Title
Terahertz Metasurface Quantum Cascade Laser

Author
Xu, Luyao

Publication Date
2017

Peer reviewed|Thesis/dissertation

UNIVERSITY OF CALIFORNIA

Los Angeles

Terahertz Metasurface Quantum Cascade Laser

A dissertation submitted in partial satisfaction

of the requirements for the degree

Doctor of Philosophy in Electrical Engineering

by

Luyao Xu

2017

ABSTRACT OF THE DISSERTATION

Terahertz Metasurface Quantum Cascade Laser

by

Luyao Xu

Doctor of Philosophy in Electrical Engineering

University of California, Los Angeles, 2017

Professor Benjamin S. Williams, Chair

Terahertz (THz) frequency range (0.3–10 THz, 30–1000 μm) is the least explored region in the electromagnetic spectrum, mostly due to a relative lack of convenient, efficient and economical THz sources. However, THz frequency range has the potential for various applications including but not limited to: astrophysics and space science, biological and medical imaging and spectroscopy, and non-destructive evaluation. This Ph.D. research builds upon the growing request for compact and efficient THz sources with both high power and high-quality beam pattern.

Since its invention in 2001, the THz quantum cascade laser (QCL) has emerged as a compact semiconductor THz source capable of delivering milliwatt-level power or higher at various frequencies from 1.2 to 5.6 THz. In the best devices, the operating temperature has reached 200 K in pulsed mode and 129 K in continuous wave (cw) mode. However, the state-of-the-art THz QCLs almost exclusively use sub-wavelength metallic and/or plasmonic waveguides, which leads to highly divergent beams. Achieving high power in combination

with an excellent beam pattern for THz QCLs remains a longstanding challenge.

Vertical external-cavity-surface-emitting-laser (VECSEL) has been demonstrated as a very successful approach to achieve high power and good beam pattern for semiconductor lasers in the visible and near-infrared. A typical VECSEL configuration consists of a quantum well (or dot) semiconductor active medium grown monolithically on a Bragg reflector and an output coupler to form a cavity. Output power is scalable with the active medium area and the cavity can be readily engineered to support only the fundamental Gaussian mode. However, the VECSEL concept has been impossible to implement for QCLs owing to "intersubband selection rule": the intersubband transitions in cascaded quantum wells — the gain medium of QCLs — are only allowed to interact with and provide gain to the electric field polarized perpendicular to the wells. This is incompatible with the natural polarization for surface incident waves in a VECSEL cavity.

This thesis reports the development of a new class of THz QCL to achieve high-power output with an excellent beam pattern — **THz metasurface quantum-cascade VECSEL (QC-VECSEL)**. The enabling component of QC-VECSEL is an active metasurface reflector composed of a sub-wavelength array of metallic microcavity antennas; each antenna efficiently couples in THz radiation, amplifies it and re-radiates into the free space. Lasing is possible when an active metasurface is paired with an output coupler form a low-loss cavity. This new architecture gives the ability to scale up output power with the metasurface area while maintaining a good beam pattern shaped by the external cavity. Moreover, this approach can leverage ongoing advances in novel metasurfaces to realize versatile functionality for QC-VECSELs, such as engineerable polarization/wavefront, spectral tunability.

The demonstration of THz QC-VECSEL marks the two "firsts": the first VECSEL in the THz frequency range and the first laser built around an active metasurface. The concept of metasurface QC-VECSEL is potentially applicable beyond the terahertz and can be applied to shorter wavelengths.

This thesis describes the theory, design, fabrication, testing and analysis of THz metasurface QC-VECSELs. Electromagnetic simulations for various active metasurfaces are presented, including the dependence of reflective gain on the antenna size, periodicity and shape, the suppression of metasurface self-lasing. A laser model is laid out for QC-VECSELs to relate the performance metrics with the metasurface and cavity design parameters, providing a tool for metasurface optimization. Numerical methods are also developed to compute the mode profile and diffraction loss of various external cavities. Experimental results and analysis are presented on a wide variety of THz metasurface QC-VECSELs varying in metasurface and cavity designs, which have yielded considerable high-performance results, including high power combined with excellent beam pattern, record-high cw power at >77 K, polarization and wavefront engineering. Finally, prospects are considered for QC-VECSELs with higher power, better temperature performance and capability to generate complex beams and versatile functionality.

The dissertation of Luyao Xu is approved.

Tatsuo Itoh

Oscar Stafsudd

Eric P. Y. Chiou

Benjamin S. Williams, Committee Chair

University of California, Los Angeles

2017

Table of Contents

List of Figures

List of Tables

Acknowledgments

This thesis would not have been possible without the inspiration and support from a number of wonderful individuals — my thanks and appreciation to all of them for being part of this journey and making this thesis possible. First of all, I owe my deepest gratitude to my adviser Prof. Benjamin Williams for his instruction, support and motivation throughout my Ph.D. career. Not only have I benefited from his extensive knowledge and in-depth understanding of physics, but I also have been inspired by his rigorous and enthusiastic attitudes on research. I am so lucky to have the opportunity to work on this exciting Ph.D. project and grateful for Prof. Williams' trust and guidance along the way. Through many trials and errors, we finally obtained lasing for the first time at a late Friday night. Prof. Williams came back to lab and shared this exciting moment with us. This is one of the best moments in my life.

I also want to express my gratitude to our long-time collaborator Prof. Tatsuo Itoh for providing many inspiring inputs to this project. It has been a great honor and pleasure working with and learning from Prof. Itoh. Thanks also goes to Dr. Mohammad Memarian for his contribution of electromagnetic modeling expertise to this project. The excellent MBE growths obtained first from Dr. Qi-Sheng Chen and then from Dr. John L. Reno is also an essential part of the success of this project.

Of course, I am thankful to my former and present labmates. This thesis work is based upon the solid foundation built by Dr. Amir Ali Tavallaee, Dr. Zhijun Liu, and Dr. Philip Hon. Much of my early training in this field also came from them. I thankfully acknowledge the valuable contributions of my present labmates Chris Curwen and Daguan Chen to this

project, especially in microfabrication and electromagnetic simulations. I also want to thank all the other labmates, Dr. Sudeep Kahnal, Jiawei Wang, Yujie Lin, and Yue Shen. Together we have created a friendly and engaging lab environment, where each one never hesitates to help the others.

Finally, I am indebted to my parents for raising me in a household that highly values education and encourages me to seek my own density. They instilled in me a passion for knowledge and a mind of determination, which took me to where I am today. I also want to thank all my caring friends inside and outside UCLA, who never let me feel alone during these years. My last thank you goes to my husband Ti-Wen for his continuous companion and support through the entire times, be it easy or hard. He always makes me believe in myself and feel life is good.

Funding: We thank the National Science Foundation (NSF) and National Aeronautics and Space Administration (NASA) for funding support throughout this work.

Facilities: The microfabrication in this work was performed at the UCLA Nanoelectronics Research Facility, and wire bonding was performed at the UCLA Center for High Frequency Electronics. We thank all the stuff members for assistance.

Vita

2007-2011	B.S. in Optical Engineering, Zhejiang University, Hangzhou, China
2009-2011	Undergraduate Research Assistant under Prof. Daoxin Dai, Department of Optical Engineering, Zhejiang University.
2010	Visiting scholar in Cross-disciplinary Scholars in Science and Technology (CSST) Program at UCLA
2013	M.S. in Electrical Engineering, UCLA.
2011-present	Graduate Student Researcher, Electrical Engineering Department, UCLA.
2013-2015	Teaching Assistant, Electrical Engineering Department, UCLA.
2016	Hardware Engineer Intern, Self-driving Car Team, Google[x], Mountain View, CA.

Publications

L. Xu, C. A. Curwen, D. Chen, J. L. Reno, T. Itoh, and B. S. Williams, "Terahertz metasurface quantum-cascade VECSELs: theory and performance," IEEE Journal of Selected Topics in Quantum Electronics, 2017. (Invited paper in press)

L. Xu, D. Chen, C. A. Curwen, M. Memarian, J. L. Reno, T. Itoh, and B. S. Williams, "Metasurface quantum-cascade laser with electrically-switchable polarization," Optica, vol. 4, 468–475, 2017.

L. Xu, D. Chen, T. Itoh, J. L. Reno, and B. S. Williams, "Focusing metasurface quantum-cascade laser with a near diffraction-limited beam," Optics Express, vol. 24, 24117–24128, 2016.

L. Xu, C. A. Curwen, P. W. C. Hon, T. Itoh, and B. S. Williams, "Terahertz Quantum Cascade VECSEL," Proceedings of SPIE, vol. 9734, 97340G, March 10, 2016. (Awarded Best Student Paper Award)

L. Xu, C. A. Curwen, P. W. C. Hon, Q. Shen, T. Itoh, and B. S. Williams, "Metasurface external cavity laser," Applied Physics Letters, 107, 221105, 2015. (Most read of the year)

L. Xu, C. A. Curwen, D. Chen, J. L. Reno, T. Itoh, B. S. Williams, Terahertz metasurface quantum-cascade VECSEL, SPIE Optics + Photonics 2017, August 6–10 2017, San Diego, CA. (Invited talk)

L. Xu, C. A. Curwen, D. Chen, T. Itoh, J. L. Reno, and B. S. Williams, "Focusing metasurface quantum-cascade VECSEL," Conference on Lasers and Electro-Optics (CLEO 2017),

May 14–19 2017, San Jose, CA.

C. A. Curwen, **L. Xu**, J. L. Reno, T. Itoh, and B. S. Williams, "Broadband continuous tuning of a THz quantum-cascade VECSEL," Conference on Lasers and Electro-Optics (CLEO 2017), May 14–19 2017, San Jose, CA.

D. Chen, **L. Xu**, C. A. Curwen, M. Memarian, J. L. Reno, T. Itoh, and B. S. Williams, "High-performance metasurface terahertz laser With electronically controlled polarization," Conference on Lasers and Electro-Optics (CLEO 2017), May 14–19 2017, San Jose, CA.

L. Xu, C. A. Curwen, J. L. Reno, T. Itoh, and B. S. Williams, "Terahertz metasurface quantum cascade lasers," 2016 International Conference on Optical MEMS and Nanophotonics (OMN), Singapore, Jun 30–Aug 4 2016. (Invited talk)

L. Xu, C. A. Curwen, Q. Chen, J. L. Reno, T. Itoh, and B. S. Williams, "Terahertz quantum-cascade VECSELs from 2.5–3.5 THz," International Conference on Infrared, Millimeter, and Terahertz Waves (IRMMW/THz 2016), Sep 25–30 2016, Copenhagen, Denmark.

L. Xu, P. W. C. Hon, T. Itoh, and B. S. Williams, "Terahertz quantum cascade VECSEL," SPIE Photonics West 2016, San Fransisco, Feb 13–18 2016. (Awarded Best Student Presentation Award)

L. Xu, P. Hon, T. Itoh, and B. S. Williams, "Terahertz quantum cascade metasurface

external cavity laser," Intersubband Transitions in Quantum Wells (ITQW) 2015, Vienna, Austria, September 6–11, 2015. (Invited talk)

B. S. Williams, **L. Xu**, and D. Chen, "Quantum cascade external cavity laser with metasurfaces," US Patent No. 15/264,509, 2016.

CHAPTER 1

Introduction

The technological exploration of the broad electromagnetic spectrum ranging from the microwave to optical frequency has led to a wealth of mature and widespread applications. However, between the traditional microwave and the infrared, there exists a frequency range named terahertz (THz) remaining one of the least tapped regions of the entire spectrum, therefore often referred to as "THz gap" (see Fig. 1.1(a)). A generalized definition of THz frequency range is 300 GHz–10 THz (λ = 30–1000 μm) [7], while the terminology varies and the lower limit is sometimes extended down to 100 GHz (λ = 3 mm). The reason for underdevelopment of THz technology is two-fold: (i) it is difficult to develop THz components, especially efficient, compact and economic THz sources, as the THz frequency is too high for electronic circuits (used for the microwave) limited by the electron speed, while too low for high-frequency photonic sources (used for the optical and near-infrared) limited by the natural materials' bandstructure properties; (ii) THz radiation experiences strong atmospheric attenuation dominated by water vapor absorption and therefore its atmospheric propagation path is limited except within certain transmission windows, making it challenging to collect THz radiation over a distance (see Fig. 1.1 (b)). Despite the obstacles, continuous and widespread efforts have been devoted to the development of THz technologies. One major

achievement is the significantly improved performance, diversity and applicability of THz sources, which facilitate a variety of promising THz applications.

1.1 THz applications

Applications in the THz range remains apparently underdeveloped, compared with its neighboring spectral ranges, the utmost reflection of which is a lack of "killer app". That's why the THz application itself makes a dynamic research topic. So far the demonstrated THz applications can be grouped into the following four categories.

1.1.1 THz astronomical and atmospheric science

THz radiation is ubiquitous in our immense universe. It is estimated that 98% of photons emitted since the Big Bang and half of the universe luminosity fall into the THz range [8], much of which is being radiated by cool interstellar medium (see Table 1.1). The spectral lines of THz emission contain rich information about mysteries of the universe, such as star and planet formation, the evolution of matter in galaxies, and even the prebiotic building blocks of life [9]. High spectral resolution ($\nu/\Delta\nu > 10^5$) observations of these emission lines and the Doppler broadened lineshapes are crucial to diagnosing the composition of interstellar medium and understanding its evolution, where high-resolution THz heterodyne spectroscopy is highly preferred. Due to the strong atmospheric attenuation of THz radiation on Earth, ground-based observation is not feasible for frequencies above 1.4 THz [10]. Therefore, THz astronomy is often conducted on high-flying platforms such as aircrafts, balloons, and space-based observatories. For example, Herschel Space Observatory, which

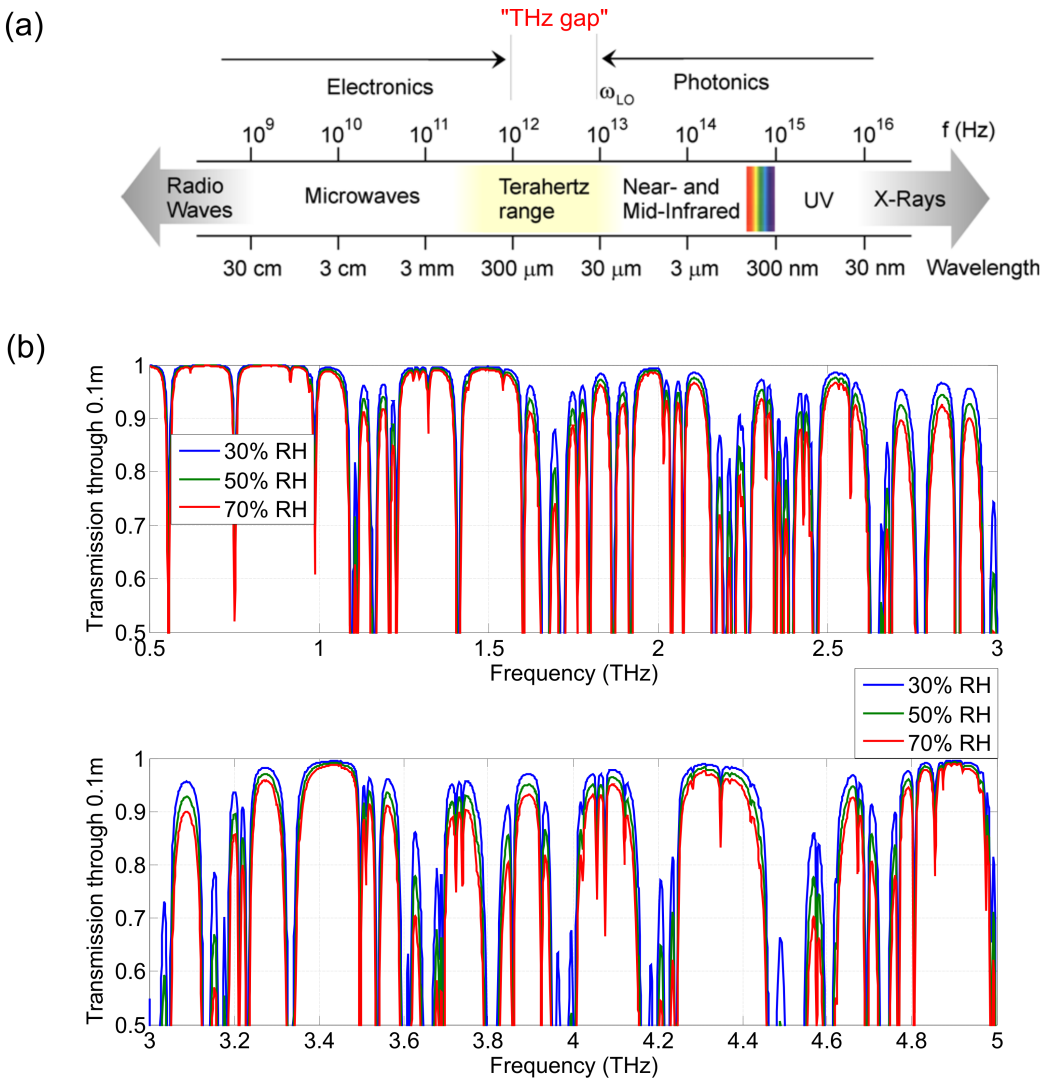

Figure 1.1: (a) THz diagram From Ref. [1]. (b) HITRAN simulation data of absolute atmospheric transmission at 300 K for three different relative humidity levels (RH) through 0.1 m of air for 0.5–3 THz band and 3–5 THz band. (Credit to Alan W. M. Lee for the HITRAN data processing code).

was the largest space-based THz observatory operated from 2009 to 2013, is equipped with a THz heterodyne spectrometer covering 0.5 to 1.9 THz [11]. More recently, the GREAT heterodyne spectrometer using a 4.7-THz quantum cascade laser as the local oscillator (LO) has been successfully operated on SOFIA during six observational flights at stratospheric altitude from 2014 to 2015 [10, 12], aimed at resolving the fine structure line of neutral atomic oxygen — OI. Further upgrade to large-scale THz heterodyne array containing tens or hundreds of pixels is under the way [6], which will bring THz astronomy to the next stage. A THz LO capable of providing sufficient power to pump the mixer or mixer array is the critical component to THz heterodyne spectroscopy, where Schottky diode mixers require milliwatts of LO power and hot electron bolometer mixers require microwatts of LO power. Given that solid-state electronic THz sources based on frequency multipliers have the power output limited below 1 mW for frequencies above 1 THz, THz quantum-cascade lasers turn out to be a key technology to meet the need of powerful LOs at and above 2 THz.

The spectral signatures abundant in the THz range are also present in Earth's atmospheres, particularly the thermal emission lines from gases that appear in the Earth's stratosphere and troposphere, such as water, oxygen, chlorine and nitrogen compounds, etc. Their spectral lines serve as the pointers to the abundance, distributions and reaction rates of species involved in ozone destruction, global warming, total radiation balance, and pollution monitoring [7]. Earth remote sensing is also best performed in a high-altitude platform using THz heterodyne detection. For instance, Earth observing system microwave limb sounder (EOS-MLS) launched on Aura in 2003 performs high-resolution heterodyne detection at multiple frequencies from 118 GHz to 2.5 THz, each of which maps a certain molecule species.

A global mapping of OH in the atmosphere is performed at 2.5 THz, using a THz gas laser as the local oscillator [13].

Table 1.1: Subset of important atomic and molecular species found in the interstellar medium at THz frequencies. From Ref. [6]

Species	Transition	THz	Importance
[C II]	$^2P_{3/2\rightarrow1/2}$	1.9013	Probe energetic PDR
[O I]	$^3P_{0\rightarrow1}$	2.06007	surfaces of molecular clouds,
[N II]	$^3P_{2\rightarrow1}$	2.4622	UC HII regions, AGB stars,
H I	n=14 $\rightarrow$ 13	2.6811	protoplanetary disks
[O III]	$^2P_{3/2\rightarrow1/2}$	3.3940	& molecular clouds.
[O I]	$^3P_{1\rightarrow2}$	4.74580	
CO	J=17 $\rightarrow$ 16	1.9560	Trace energetic molecular
	J=21 $\rightarrow$ 20	2.4139	gas in star-forming regions,
	J=25 $\rightarrow$ 24	2.8703	PDR's, SNR's, AGB ejecta.
o-$H_2^{18}O$	$2_{21} \rightarrow 1_{10}$	2.7416	Probe enhanced H_2O
p-$H_2^{18}O$	$2_{20} \rightarrow 1_{11}$	2.9389	in shocks, outflows, disks.
HD	0-0 R(0)	2.67499	Cosmological nucleosynthesis, deuterium fractionation, thermal history of starforming regions, abundance of H_2.
OH	$\Pi_{3/2\rightarrow1/2}$	1.83	Ground state OH; general
	$\Pi_{7/2\rightarrow5/2}$	2.60	H_2O and oxygen chemistry.

1.1.2 THz spectroscopy

THz has been referred as a "fingerprint region" because many molecules have strong rotational and vibrational resonances in this range. So THz spectroscopy serves as an ideal tool to identify the molecule species and elucidate its structural changes. Besides, THz radiation is non-ionizing due to very low photon energy (1–40 meV) and can propagate through barrier materials, such as clothing, plastic, wood, paper. These unique features make THz spectroscopy a desirable tool for conducting non-contact detection of concealed chemical composites, such as explosives, illicit drugs, etc [14–16]. A popular method of doing THz spectroscopy is THz time-domain spectroscopy (TDS), which a coherent method that can determine both the amplitude and phase of a THz pulse at each spectral component [17].

This gives ways to determine the complex refractive index of materials over a broad THz range. THz frequency combs, which generate a broadband spectrum with evenly spaced and well-defined lines, offer another way to perform THz spectroscopy and is expected to outperform THz-TDS by its compactness and superior resolution enabled by dual-comb technique [18, 19].

1.1.3 Non-destructive imaging

Non-destructive THz imaging has been actively investigated and applied to the medical imaging applications where the water concentration serves as an effective contrast mechanism. The high THz absorption and dielectric properties of water yield easily detectable changes in THz reflectivity for small changes in hydration [20]. Combined with the non-ionizing THz photon energy, THz imaging has been demonstrated as an ideal tool for in-vivo imaging of skins burns [21], corneal pathologies [22], and cancers [23]. THz endoscopy imaging further extend the THz-based diagnostic system to the internal organ of the body [24]. THz imaging also applies to other fields including security screening [14], pharmaceutical tablet coating thickness monitoring [25], aircraft composites defect inspection [26, 27], and artworks evaluation [28].

1.1.4 High-bandwidth THz communication

The rise of THz technologies has also attracted the great interest from wireless communication community to push the carrier frequency to THz range in order to meet the ever-increasing demand for high-bandwidth (>100 Gbit/s) wireless communication. However,

one of the big obstacles is the strong atmospheric attenuation that generally increases with frequency except some transmission windows. So the THz frequencies feasible for wireless communication are limited to the lower end for longer distance, leaving >1 THz wave only useful for near-field communication (<0.1 m) [29]. In addition, the rainfall makes another cause of attenuation for the outdoor applications. Free-space optics communication using infrared light appears as a competing technology, but it also suffers from high losses due to rainfall [30] and foggy conditions [31] and lower tolerance in beam alignment [32]. It is still too early to conclude which will becomes more adopted in the marketplace, which is ultimately determined by cost, size, performance and usability [29].

1.2 THz sources

Compared with other frequency ranges, the availability of THz sources with coherent emission has long been limited. The early source of THz radiation is from thermal blackbody radiation, which is incoherent and low-power. Generation of coherent THz radiation is intrinsically difficult, because this unique frequency range falls into the high end of solid-state electronic source devices, which experiences significant high-frequency power roll-off owing to both transit-time and resistive-capacitive (RC) parasitics effects [7, 33]. On the other hand, as the THz photon energy (0.3–10 THz, 1–40 meV) is comparable to phonon resonance that thus acts as a fast depopulation channel, it is challenging to build a THz laser that relies on a sustainable population inversion. Besides, there exists no natural materials with bandgaps of THz photon energy that can be directly used as gain medium. Nevertheless, driven by the application needs, decades of research efforts have led to a variety of THz generation tech-

niques varying in the underlying physics and performance properties. An ideal THz source would need to be high-power (above multi-milliwatts), energy-efficient, compact, economic, frequency-engineerable/tunable, with descent beam pattern, easy-to-use (turn-key, room-temperature operation), and etc, which are unfortunately not seen simultaneously in any single THz source demonstrated so far. Three representative categories of THz sources are briefly reviewed, and a summary of THz sources with competing performance is presented in Table 1.2.

1.2.1 Solid-state electronic sources

Solid-state THz electronic sources rely on the generation of fundamental frequency typically of hundreds of GHz from radio-frequency (RF) sources, followed by chains of frequency multipliers and power amplifiers to produce higher-order frequency harmonics that approach to the THz regime. Resonant tunneling diode and Gunn diode are two extensively-used RF sources capable of generating fundamental oscillations typically between 100–300 GHz [34, 35]. To go beyond 300 GHz, chains of high-frequency multipliers (frequency doublers, triplers, and mixers) and power amplifiers are typically needed to generate a specific harmonics of an input fundamental frequency and suppress undesired ones. High-electron-mobility transistor (HEMT), resonant-tunneling transistor (RTD), and Schottky diode are widely used for building frequency multiplication and power amplification chains [36, 37, 34], however, with no direct observation of gain reported above 1 THz [38]. Solid-state THz sources are after all subject to the fundamental frequency limit imposed by the electron transit-time and RC parasitics effect, therefore exhibiting a significant power roll-off with frequency proportional

to f^{-4}. As a result, power generated at frequencies >1 THz is limited to far below 1 mW [37], both at room temperature (RT) and cooled conditions.

1.2.2 Frequency down-conversion

Opposite to pushing frequency up, another strategy towards THz generation is to convert the input at high frequencies (such as visible and near-IR wave) down to the THz range. This is often realized by pumping a high-power ultra-short (<1 ps) pulse from a mode-locked laser onto a photoconductive antenna (PCA) under bias to induce fast electron oscillations to produce a broadband THz radiation [39], which is extensively applied in THz-TDS systems. The highest broadband power over 0.1–5 THz is reported at 3.8 mW from a large-area plasmonic photoconductive emitter [40], with > 1% optical-to-THz conversion efficiency. PCA also works as a photomixer under two cw/quasi-cw optical pumps with a frequency offset at THz [41, 42]. However, due to the limit of transport time between contact electrodes, the power tends to roll off with frequency and the demonstrated power at frequencies >1 THz so far is still sub-milliwatt. Another technique uses optical rectification of ultra-short pulsed pump in nonlinear crystals, which can produce broadband radiation with power peaked at >1 THz [43, 44]. However, a major drawback for this down-conversion technique is the need for a bulky and power-hungry mode-locked laser, which limits its utility largely within laboratories.

More recently, there have been efforts in leveraging high-power and RT two-color mid-infrared (mid-IR) quantum-cascade lasers to generate THz wave via the intracavity difference frequency generation (DFG) using the $\chi^{(2)}$ nonlinearity of laser material itself [45–47]. The

signature advantage of this technique is the RT generation of THz radiation. A wide tunable frequency range of 1.2–5.9 THz has been demonstrated so far [48]. But due to the limited conversion efficiency of the DFG nonlinear process ($\sim$0.1–1 mW/W^2), the peak pulsed power is limited up to 1.9 mW and cw power is limited up to 3 μW [49].

1.2.3 THz lasers

Optically-pumped molecular gas lasers can generate THz radiation with frequencies determined by the rotational levels of the excited vibrational states of gas molecules, which was started by in 1970 [50]. Depending on the type of gases, the discrete emission lines span 0.1–8 THz [51], but with very limited tunability. Typically gas lasers under high pumping are commonly capable of delivering tens to hundreds of milliwatt cw power depending on the chosen line. One of the strongest emission lines is from methanol at 2.52 THz, which is used by the gas laser on the Aura satellite that acts as a local oscillator [13]. Even though this type of THz laser is very expensive, bulky, and power-hungry, it still receives wide applications due to the considerable power level available at RT.

Coherent and high-power THz radiation is obtainable from free electron laser (FEL), where the optical amplification is achieved by feeding high energy electrons through a periodic arrangement of magnets (i.e. undulator) [52, 53]. The usage of FEL is within relatively few large facilities in the world due to the super-bulky and expensive setup involved.

Semiconductor THz laser has been demonstrated in p-type germanium (Ge) in crossed electric and magnetic fields and in uniaxially stressed Ge via optical transitions between light-hole and heavy-hole subbands [54], and in silicon doped by group-V donors based on

either long-lived impurity states or resonant electron-phonon interaction [55]. Even though tens of milliwatts up to 10 W have been reported from p-type Ge lasers, though at a duty cycle <5%, with frequency tunable in the range of 1-4 THz [56], the need for magnetic field, high voltage, and cryogenic operation (<80 K) limits its applicability. The stressed Ge laser and doped-Si laser, though with no need for magnetic field, deliver much lower power (microwatts-level) and cease to lase at a lower temperature (<40 K) [57, 56].

Quantum cascade laser (QCL) has developed to be a compact and powerful THz semiconductor laser with a spectral coverage over 1.2-5.6 THz [3, 58], since its birth in 2001 [59]. Since the topic of thesis is on a new type of THz QCL, the fundamental theory and state-of-the-art of THz QCL will be given in details below.

Table 1.2: Summary of selected THz sources.

Technique	Output Power	Operation Temperature	Comments
Solid-state electronic sources	<1 mW above 1 THz	RT or cooled	Output power rolls off rapidly with increasing frequency due to both transit-time and RC effect
Photoconductive antenna	up to 3.8 mW (pulsed); <1 mW above 1 THz (cw/quasi-cw)	RT	External optical pumping laser needed; widely used in THz-TDS.
Optically-pumped gas laser	tens to hundreds of milliwatts (cw); kilowatts (pulsed)	RT	External pumping laser needed; only at selected frequencies; power-hungry
THz QCL	up to 230 mW (cw); up to 2.4 W (pulsed)	<200 K (pulsed) <129 K (cw)	Compact semiconductor laser; frequency-engineerable/tunable

1.3 Basics of THz QCL

QCL is a category of electrically-injected semiconductor laser, where the optical amplification comes from the electronic intersubband transitions in quantum well active materials. For THz QCLs, the quantum well active material is typically grown layer by layer by molecular beam epitaxy (MBE) to a total thickness of 5–10 μm. It comprises hundreds of repeated stacks of alternating well and barrier materials of a few monolayers thickness, such as GaAs and $Al_{0.15}Ga_{0.85}As$, where electrons see a potential varying spatially on the order of a De-Broglie wavelength in the growth direction. As a result, electron motion in this direction is restricted and energy is quantized into discrete subbands. The energy seperation and radiative/nonradiative intersubband transition rates are readily engineerable by deliberate design of layer composition, thickness and doping, which gives a way to build a population inversion and therefore a laser out of it. Moreover, given the flexibility in material choice and quantum wells design, the lasing frequency design is very flexible, with the spectral coverage demonstrated from mid-IR to THz. Fig. 1.2 presents an example of THz QCL active region band diagram and SEM image.

A note has to be made here to differentiate QCLs from quantum well lasers (QWLs), which are widely used in near-IR and optical range, such as InGaAsP/InP laser used for communication wavelength. Even though QWLs also use quantum well heterostructures as the gain material, the optical amplification in QWL relies on the interband transition between electron and hole states separated by a bandgap, i.e. electron-hole recombination, as Fig. 1.3(a) shows. Since the dispersion curves of electron and hold states have opposite curvature, the joint density of states (JDOS) for an interband transition intrinsically broaden

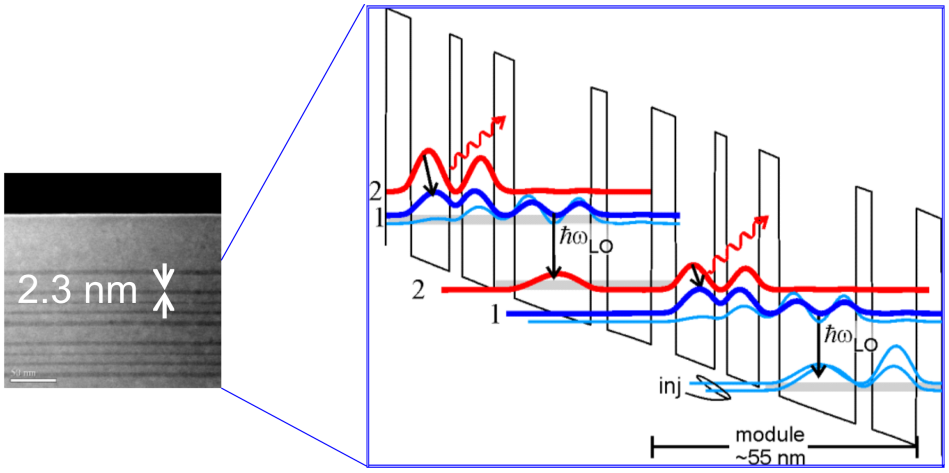

Figure 1.2: Band diagram of two repeated modules in a THz QCL active region and its SEM image.

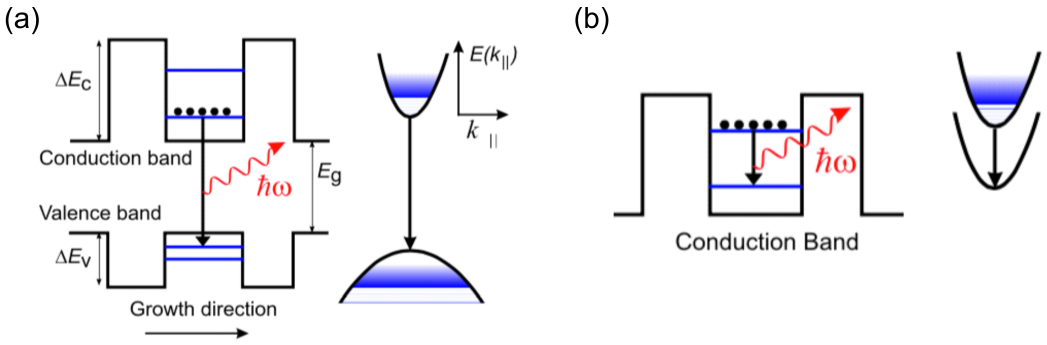

Figure 1.3: Illustrations of band diagram and energy-momentum dispersions of the relevant states for (a) interband transitions and (b) intersubband transitions. Figure from [2].

around the photon energy of interest. As a result, only a small portion of the population inversion contribute to the single-frequency lasing. Besides, the lasing frequency is restricted above that determined by the bulk material's bandgap, which makes it impossible to generate far-IR and THz wave from QWLs. However, as being said, QCL is an intersubband laser, where all the relevant transitions occur between discrete states within the conduction band and only involve electrons. The dispersion curvature of each subband has the same parabolic shape, with the energy separation unchanged with in-plane momentum, as seen from Fig. 1.3(b). Therefore the JDOS for an intersubband transition is intrinsically a delta function, the entire population inversion of which contributes to the gain. In addition, the nature of intersubband frees the lasing frequency from the low-bound limit of bulk materials' bandgap.

The concept of QCL has its roots in the proposal of using intersubband transitions for radiation amplification in a superlattice structure in 1971 by Kazarinov and Suris [60]. The first QCL was demonstrated at 4 μm (75 THz) at Bell Labs in 1994 [61]. Since then QCLs have become the dominant mid-IR semiconductor laser sources covering 3.5–25 μm [62]. Their best performance is in the 4.5–10 μm range, where RT operation, high power with hundreds of milliwatts, and high wall-plug efficiency have been demonstrated [63]. Meanwhile, efforts were also devoted to the development of THz QCL, which, nevertheless, was hindered by two major difficulties: (i) due to the low photon energy (4–20 meV, 1–5 THz) of THz wave, the energy separation between the two lasing states is very small so that it is difficult to selectively populate the lower state while maintaining the population at the upper state. (ii) it is challenging to obtain a low-loss waveguide for such long wavelengths due to increased free carrier scattering loss with wavelength in doped semiconductors.

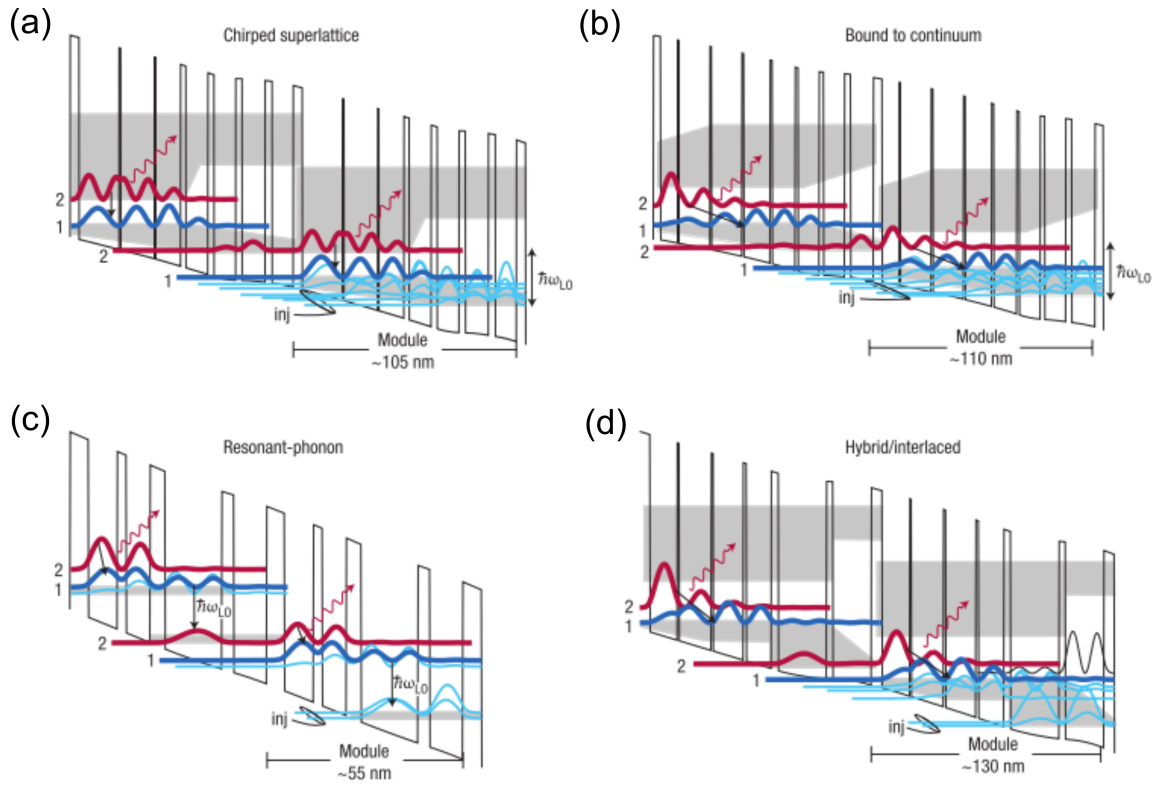

Figure 1.4: Band diagrams for four types of active region designs: (a) chirped superlattice (CSL), (b) bound-to-continuum (BTC), (c) resonant-phonon (RP), (d) hybrid/interlaced design. Figure from Ref. [3]

1.3.1 Active region design

The first THz QCL was demonstrated in late 2001 by Köhler, *et al* [59], which operated at 4.4 THz with a peak pulsed power of 2.5 mW at 8 K and maximum operating temperature T_{max} = 40 K. Soon after that, different groups demonstrated their THz QCLs varying in both active region and waveguide designs [64–67]. There are four major classes of active region designs. The chirped superlattice (CSL) is the winning design for the first THz QCL [59], where two minibands form and the radiative transition takes place between the two band-edge states. Fig. 1.4(a) exemplifies the band diagram of an CSL design. Population inversion is established because the intra-miniband scattering between tightly coupled states

quickly relax electrons to the bottom of the lower miniband. In the second class of bound-to-continuum (BTC) design shown in Fig. 1.4(b), the lower miniband is preserved as an efficient depopulation and transport mechanism, while the upper radiative state is made to be a bound state created inside the minigap, which allows for a more diagonal radiative transitions to maximize the lifetime ratio between upper and lower state, as well as the injection efficiency. This leads to improved power and temperature performance compared with CSL designs [67].

The third class of resonant phonon (RP) design directly exploits LO-phonon scattering as a fast depopulation mechanism. As is common for designing mid-IR QCLs, the collector/injector state is separated from the lower radiative state by a longitudinal-optical-phonon (LO-phonon) energy so that electrons in the lower state are quickly scattered to the collector/injector states by emitting a phonon. However, this becomes problematic for THz QCLs because the LO phonon scattering also depopulates the upper radiative state due to the small energy separation from the lower state. The key of RP designs is to make the lower radiative state anti-cross with an excited state in the adjacent wells through resonant tunneling. So after tunneling to the excited state, the electrons are quickly scattered to the injector state, which is separated from the excited state by a LO-phonon energy. An example of RP design is shown in Fig. 1.4(c). This resonant LO-phonon depopulation process leads to a lower state lifetime of several subpicoseconds. Since the injector state has little spatial overlapping with the upper radiative state, the upper state lifetime is kept to be several picoseconds. Compared with CSL and BTC designs, RP designs involve no miniband and fewer quantum wells, which typically only have 2–4 wells in a module [65, 68, 69]. The smaller module

length leads to a higher density of radiative transitions, which can compensate for the smaller oscillator strength than the other two designs.

The hybrid design combines the BTC design with the phonon-assisted depopulation [70, 71]. A miniband is designed to replace the single state that resonates with the lower lasing state in the RP design. This architecture has the advantage of reducing the direct coupling between the upper state and the extractor stage since they are physically separated by the length of the miniband region [71]. The miniband design also relaxes the alignment condition on the extractor stage.

It is notable that so far a number of high-power [72–74] and high-temperature [75–78] performances are reported from THz QCLs based on RP and hybrid designs.

1.3.2 Waveguide design

Conventional dielectric waveguides for mid-IR QCLs are not suitable for THz QCLs, because the required thickness of cladding that scales with wavelength is not feasible for MBE growth and the THz QCL active region made of GaAs/$Al_xGa_{1-x}As$ has a lower refractive index than GaAs substrate. Due to high free carriers scattering loss in doped semiconductors that increases with wavelength ($\propto \lambda^2$), unique waveguide geometries have been proposed for THz QCLs in order to minimize the spatial overlapping between the waveguide mode and the doped cladding layers. Two major types of waveguides are widely used now for THz QCLs. As shown in Fig. 1.5(a), the semi-insulating surface-plasmon (SI-SP) waveguide, which is used in the first demonstrated THz QCL [59], uses a thin heavily doped layer sandwiched between the active region and the semi-insulating GaAs substrate to support a compound

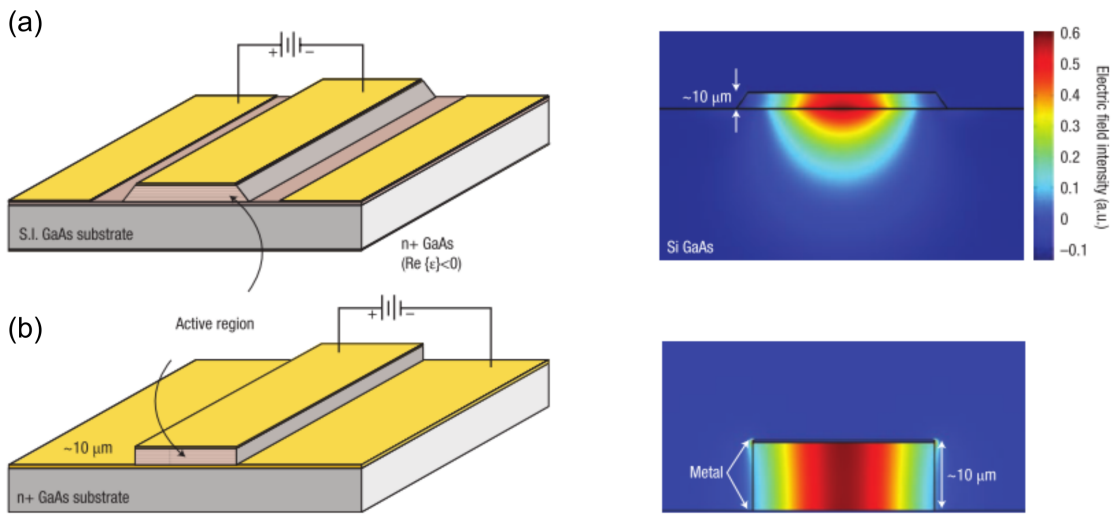

Figure 1.5: (a) Schematic of a SI-SP waveguide and its mode profile. (b) Schematic of a MM waveguide and its mode profile. Figure from Ref. [3]

surface-plasmon mode; it is confined by the metal cladding on top of the active region, and extends into the bottom substrate with a loose confinement. The confinement factor Γ, which describes the overlap of the mode with the active region, is between 0.1–0.5 for SI-SP waveguide. Metal-metal (MM) waveguide, shown in Fig. 1.5(b), is another geometry that provides very tight modal confinement by placing a metal cladding immediately on top and bottom of the active region, which achieves an almost unity Γ [79]. Because of very different modal confinements, SI-SP waveguides tend to have a larger size (ridge width >100 μm) than MM waveguides (ridge width ~10–50 μm), so are the modal sizes. As a result, SI-SP waveguides tend to produce higher output power and better beam patterns, while MM waveguides outperform in operating temperature due to the skinnier size.

1.4 Challenges of THz QCLs

So far, THz QCLs have been demonstrated at various frequencies over 1.2–5.6 THz, peak pulsed power as high as 2.4 W, cw powers as high as 149 mW, and operating temperature up to 200 K (pulsed) and 129 K (cw) [80, 58, 74, 72, 75, 78]. However, these best performances are achieved in different devices and the associated beam patterns are likely far from near-Gaussian shapes desired for most applications. Achieving high powers in combination with good beam patterns at a relatively high temperature still remains a challenge and research hot spot. A brief summary of the demonstrated approaches towards high operating temperature, high power and high-quality beams is given below. Some state-of-the-art demonstrations are summarized in Table 1.3 in terms of the important performance metrics including power, operating temperature, beam divergence, slope efficiency.

1.4.1 Operating temperature

In contrast to the rapid commercialization of mid-IR QCLs, the wide adoption of THz QCLs is hindered primarily by the low operating temperature, which necessitates cryogenic cooling facilities. The major reason is the depopulation of electrons with high in-plane momentum in the upper radiative subband via the LO-phonon scattering to any other energetically allowed states. As temperature increases, more electrons get thermally activated and therefore scattered by LO-phonon, resulting in a dramatic decrease of upper level lifetime. The thermally-activated LO-phonon scattering is alleviated to some extent by adding an external magnetic field perpendicular to the quantum wells, which splits the continuous in-plane bandstructures to discrete Landau levels where LO-phonon scattering is not allowed in en-

ergy. The improvement of T_{max} has slowed down in the recent decade. To progress beyond RT or at least thermoelectric cooler temperature, novel materials systems and design concepts have been explored and anticipated, such as using GaN/AlGaN materials with a much higher LO-phonon energy [81], quantum dots materials with 3D quantum confinement to suppress thermally-activated LO-phonon scattering [82]. Due to the difficulties in material growth and processing, no experimental results have been reported so far that surpass the performance of GaAs/AlGaAs-based THz QCLs.

Although RT operation is desired, cryogenic operating temperature for THz QCLs is feasible for applications, given the availability of compact-size and easy-to-use cryocoolers. A THz QCL capable of delivering milliwatt-level cw or averaged power at or above liquid nitrogen temperature (77 K) still stands out as a desirable THz source. In terms of thermal performance, the MM waveguide with narrow ridge width is a favorable geometry relatively efficient in thermal removal. T_{max} records in pulsed and cw mode are both reported from narrow ridge MM waveguides [75, 78]. Fig. 1.6 is a survey of the reported T_{max} for SI-SP waveguides and MM waveguides.

1.4.2 High power and high-quality beam

High power output from THz QCLs is generally achieved by making large-dimension SI-SP waveguides. The loosely-confined large modal size supported by SI-SP waveguides is preferred to harvest power from a large chunk of active gain medium. For instance, the record-high pulsed power of 2.4 W is achieved from a long and wide SI-SP waveguide (4.2 mm $\times$ 425 μm) based on a 24 μm-thick active region at 10 K [74], showing a multimode

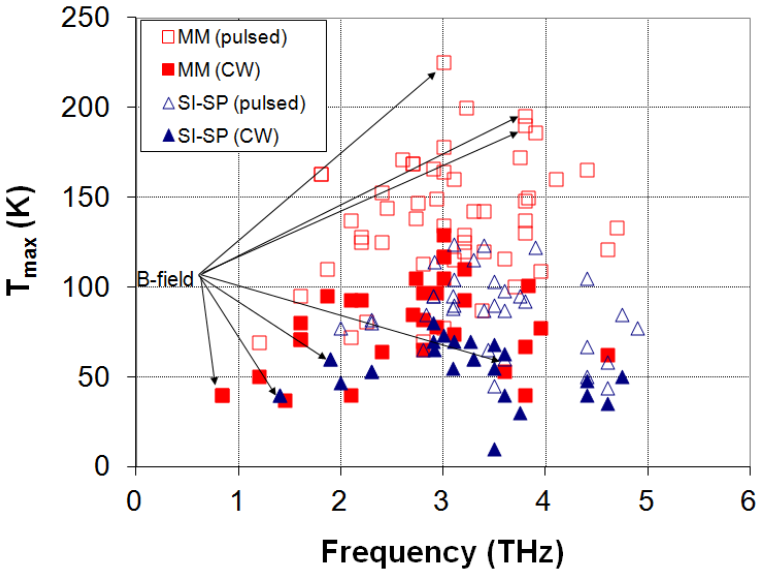

Figure 1.6: Survey of the reported peak operating temperatures shown as a function of lasing frequencies, sorted by waveguide geometries and pulsed or cw mode. The data points indicated by the arrows are for QCLs in an external magnetic field.

spectrum owing to the wide ridge. The cw power record of 149 mW is measured from a large Epi-down mounted SI-SP waveguide (2 mm $\times$ 130 μm) at 10 K, which ceases to lase in cw at 70 K. SI-SP waveguides with doubled height are also demonstrated by stacking two symmetric active regions on top of each other via wafer bonding, which showed 470 mW pulsed power from a single facet [83] at 5 K. However, large-dimension SI-SP waveguide is a poor structure for heat removal, which limits its cw performance at high temperature. So far THz QCLs demonstrated with >1 mW cw power at 77 K are all based on the MM waveguide [76, 84, 85].

Beam pattern is another fundamental feature for laser applications. Unfortunately, the beam output from a conventional cleaved-facet MM waveguide is very divergent, characterized by concentric rings in the far-field [86], as shown in Fig. 1.7. This is because the radiation from the subwavelength apertures (i.e. waveguide facets) is subject to severe diffraction, re-

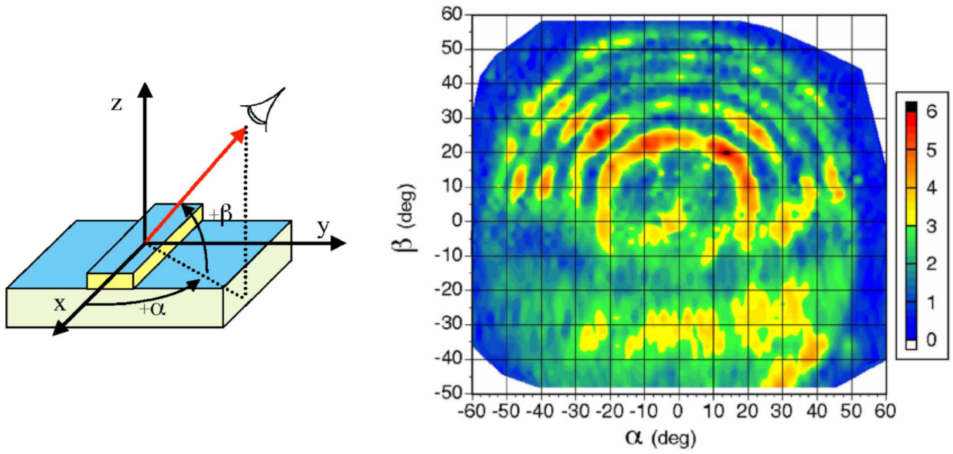

Figure 1.7: Experimental beam pattern emitted from a MM waveguide facet and the angle definition of the measurement setup.

sembling a point source radiation. This is further degraded by the field interference effect that generates fringing patterns. Although SI-SP waveguides are exempt from severe diffraction effects, the output beams are still non-ideal with large angular divergence, which calls for external beam-shaping optics [56, 87]. Considering the importance of thermal performance for applications, efforts have been devoted to improving the beam pattern from MM waveguide-based THz QCLs. A straightforward method is to attach an hyperhemispherical silicon lens to the waveguide facet to collimate the beam [88], which has shown an improved beam yet far from ideal. Besides, the third-order distributed feedback (DFB) QCL has achieved narrow beams from end-fire emission [89, 90, 84]. This is realized by designing the mode effective index to achieve the phase matching condition that the fields at grating openings radiate constructively in end-fire direction. For example, $6° \times 11°$ far-field is reported from a 5.7 mm long third-order DFB THz QCL [89]. To relieve the constraint on mode effective index, an antenna-feedback scheme is proposed to excite a compound surface plasmon mode that radiates in an ultra-narrow beam of $4° \times 4°$ in the end-fire direction [91]. But

since the beam divergence scales inversely with the square root of the cavity length, which is not diffraction-limited, further narrowing the beam requires a very long cavity, for which the phase matching condition becomes increasingly strict. Additionally, scaling up the power by increasing the ridge width or length results in thermal degradation. The other approaches exploit surface emission from a large radiating aperture to achieve good beam quality [92–94, 85, 95]. This is often realized by designing a second-order DFB [92] or its variation form such as a graded photonic heterostructures (GPH) ridge [85], which have achieved significant beam narrowing in the axis along the ridge. If one wishes to further reduce the beam divergence in the other axis by increasing the width of second-order DFB waveguides, thermal performance suffers and multiple transverse modes can appear. Another way to narrow down the beam divergence in both axes is using phase-locked second-order DFB arrays [93, 96, 95] and 2D photonic crystal cavities [94]. However, on-chip phase locking is challenging for a large number of array elements, and grating side-lobes appear if the array spacing is larger than the wavelength, which makes it difficult to further decrease the beam divergence. As an example, for phase-locking of second-order DFB arrays via antenna-mutual coupling [95] incoherent lasing and beam broadening are observed when two array quadrants are biased simultaneously. As for photonic crystal cavities, increasing the dimension to achieve further beam narrowing causes thermal degradation. Understandably, the phase-locking challenge and the thermal issue also makes it difficult to scale up the output power.

In summary, while many of these DFB approaches have realized improved beam patterns and output coupling efficiency, they show their limitations when one wish to either further narrow the beams or scale up the output power while maintaining a good beam. A secondary

issue is that DFB and other Bragg grating approaches are inherently narrowband, and largely unsuitable for widely-tunable single mode lasers or for broadband frequency combs.

Table 1.3: Survey of the state-of-the-art demonstrations of THz QCLs with high output power, good beam pattern and high operating temperature. η_{slp} is the slope efficiency. T_{max} is for pulsed mode unless specified.

Approach	Beam pattern	T_{max}	Output power	Spectral mode
Wide SI-SP waveguide with 24 μm-thick active region [97]	Divergent	125 K	2.4 W (pulsed, 10 K) η_{slp} = 1.64 W/A	Multi-mode
MM waveguide [75]	Divergent	200 K	38 mW (pusled, 8 K)	Multi-mode
Narrow ridge MM waveguide 3^{rd} order DFB [78]	33° × 22.5°	129 K (cw)	0.7 mW (cw, 30 K) η_{slp} = 28 mW/A	Single-mode
Graded photonic heterostructures (GPH) [85]	9°×20°	120 K	103 mW (pulsed, 20 K) η_{slp} = 230 mW/A 3.8 mW (CW, 12 K)	Single-mode
Phase-locked GPH arrays [96]	∼9°×6°	100 K	6 mW (pulsed) η_{slp} = ∼28 mW/A	Single-mode
2D photonic crystal cavity [94]	12°×8°	149 K	5 mW (pulsed, 78 K) η_{slp} = 3 mW/A	Single-mode
3^{rd} order DFB [89]	6°×11°	NA	5 mW (pulsed, 10 K) η_{slp} = 140 mW/A	Single-mode
2^{rd} order DFB arrays phase locked by antenna mutual coupling [95]	10°×10°	NA	6.5 mW (pulsed, 10 K) η_{slp} = 450 mW/A	Single-mode
Plasmonic laser with antenna-feedback gratings [91]	4°×4°	124 K	1.5 mW (pulsed, 78 K) η_{slp} = 15 mW/A	Single-mode

1.5 VECSEL approach to QCLs

Achieving high power in combination with good beam patterns is in fact a challenge for many types of semiconductor lasers. Simply increasing the waveguide size to scale up the power lead to multiple transverse mode oscillation, resulting in suboptimal beam quality as

well as transverse modal instabilities. One successful solution that has been demonstrated in the visible and near-infrared is the vertical-external-cavity surface-emitting-laser (VECSEL), which can be thought of as a semiconductor version of a diode-pumped solid-state disk laser. As shown in Fig. 1.8, the basic configuration is an optically pumped semiconductor gain medium backed by a distributed multi-layer Bragg mirror, which forms an open optical cavity with an output mirror. Because the cavity can be designed to preferentially support only the fundamental TEM_{00} Gaussian mode, very high beam quality can be obtained without the divergence and astigmatism found in edge emitting semiconductor lasers. The output power is scalable with the area of gain medium and optical pump. Provided that the pumping area is matched with the fundamental modal spot and the gain medium is well heat sunk, the issue of multiple transverse mode formation and instability can be largely alleviated [98]. Since the first demonstration in 1997 [99], the power of VECSELs have been steadily improved to >100 W (cw) in multi-transverse mode operation [100], and >25 W (cw) in single-frequency operation in TEM_{00} mode [101]. With the intra-cavity access, versatile functionalities have been integrated to VECSELs such as employing saturable absorber mirrors to drive VECSELs in a mode-locked regime [102, 103]. Electrically-pumped VECSELs with no need for an external pumping source mark another important step towards compact and convenient VECSELs [104, 105].

Despite the success in the near-IR and visible, it had been impossible to implement the VECSEL approach for QCLs due to the "intersubband slectron rule," which requires that the electric field must be polarized perpendicular to the plane of quantum wells in the QC gain medium to be amplified. This is incompatible with the natural polarization parallel to

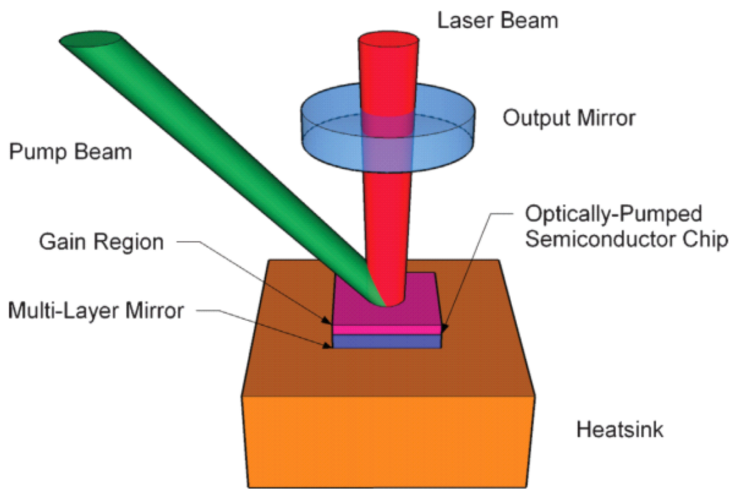

Figure 1.8: Schematic of a VECSEL. Figure from Ref. [4]

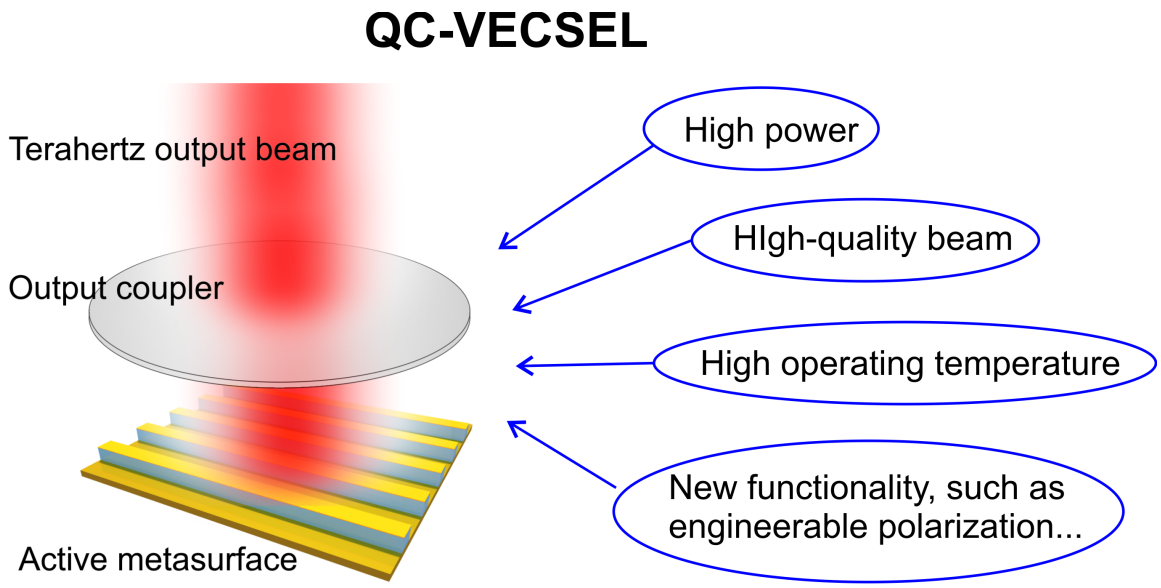

Figure 1.9: Schematic of a QC-VECSEL composed of an active metasurface and an output coupler.

the semiconductor surface in a VECSEL cavity. To address this issue, an active metasurface reflector composed of an array of metallic microcavity antennas loaded with QC gain material is developed; each antenna efficiently couples in THz radiation, amplifies it and re-radiates into the free space. The amplifying metasurface is then paired with an output coupler to create an external laser cavity. This new scheme of QCL is named as **QC-VECSEL**, a schematic of which is shown in Fig. 1.9. It is essentially an electrically-pumped VECSEL. The approach of QC-VECSEL is fundamentally different from the previous beam shaping techniques — it is the super mode of the VECSEL cavity, rather than the mode of the individual metallic microcavities on the metasurface, that exhibits lasing and shapes the beam to a near-Gaussian profile. Multiple aspects of design and engineering that enable QC-VECSEL are the focuses of following chapters. Compared to conventional THz QCLs, the advantages of QC-VECSEL can be summarized as:

- The output power is scalable with the active area on the metasurface as more active microcavities contribute stimulated emission to the VECSEL cavity mode.
- A near-Gaussian beam pattern is obtainable with the external cavity that tightly shapes the beam.
- Compared to monolithic cavities, it is easier to achieve the optimum coupling condition and maximize the output power by choosing the reflectance of the output coupler.
- The sparse arrangement of the microcavities reduces the power dissipation density, which helps to improve temperature and cw performances; each microcavity is very small, which maintains a favorable geometry for heat removal.

- Versatile metasurface designs can be leveraged to integrate new functionality to QC-VECSELs, such as wavefront/polarization engineering, broadband operation for tuning, frequency combs generation, higher-order mode engineering for multi-beams, arbitrary beam generation using holographic metasurfaces, etc.

Experimental demonstrations of the advantages will be presented and discussed in the following chapters. Of course, these advantages must be deliberately balanced against the additional size and complexity of an external cavity.

1.6 Thesis overview

This thesis is focused on the theory, design, fabrication, testing and analysis of THz metasurface QC-VECSELs. Chapter 2 presents a summary of electromagnetic simulations and design considerations for active metasurfaces, including the dependence of reflective gain on the antenna size, periodicity and shape, the suppression of metasurface self-lasing. In Chapter 3, a laser model is laid out for QC- VECSELs to explicitly relate the performance metrics with the metasurface and cavity design parameters, providing a tool for design optimization. Numerical methods are also developed to calculate the mode profile and diffraction loss of external cavities of different types, which is detailed in Chapter 4. Chapters 5–8 present a wide variety of experimentally demonstrated THz metasurface QC-VECSELs varying in both metasurface and cavity designs, which have yielded considerable high-performance results and valuable information about QC-VECSELs power scaling, beam shaping, polarization and wavefront engineering, and high-temperature/cw operation. Finally, a comprehensive summary is given in Chapter 9, where prospects are considered for QC-VECSELs with higher

power, better temperature performance and capability to generate complex wavefront beams.

CHAPTER 2

Active metasurface design

Active metasurface reflector plays a key role in the QC-VECSEL to both provide the gain and constitute the cavity. The proposal of an active metasurface composed of many microcavity metallic antennas loaded with QC active materials makes it possible to implement the VECSEL concept for THz QCLs, as the unique modal properties of the metallic antenna design makes the "intersubband selection rule" satisfied inside the QC material. This chapter provides a comprehensive look at various design aspects of active metasurface reflectors. Since metasurfaces comprise a dynamically advancing field of research, an overview of this research field is presented in the beginning. Then I will introduce a baseline active metasurface design comprising an array of identical metal-metal microcavity ridge antennas in details and discuss the Bragg scattering and self-lasing suppression. Alternative designs of active metasurfaces are presented next to show the versatility of metallic antenna design and arrangement. Finally the fabrication procedures for active metasurfaces are briefly introduced.

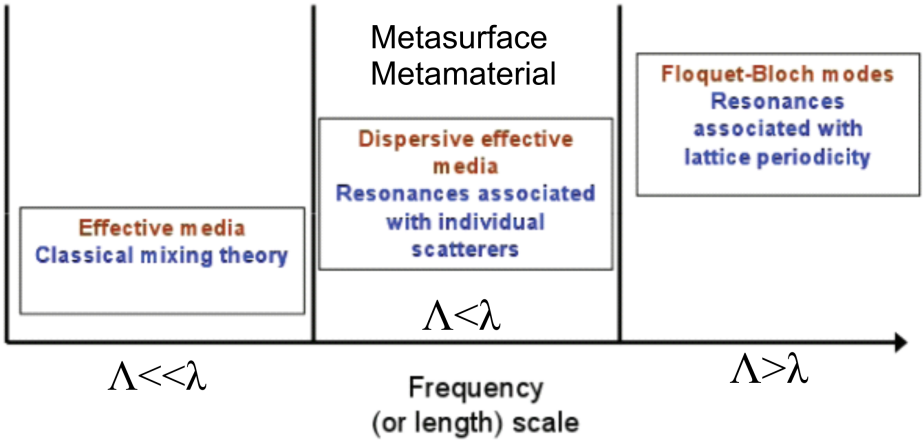

Figure 2.1: Three characteristic regions of artificial composite materials. Figure from Ref. [5].

2.1 Survey of metasurfaces

Metamaterial and metasurface are modern concepts of devising artificial electromagnetic structures to engineer the wavefront of by altering its phase, amplitude, and polarization in a desired manner. Metamaterial is known for the engineerable bulk electric response (represented by permittivity ϵ) and magnetic response (represented by permeability μ), devised by arranging small resonators/scatterers structured on a subwavelength scale throughout a region of 3D space; the bulk response accumulated through propagation leads to the desirable wavefront. Metasurface, in contrast, is a surface or interface metastructure composed of resonators/scatterers arranged in 2D pattern of subwavelength thickness. Therefore interaction with metasurfaces introduces minimal propagation phase and the bulk material parameters are of less interest [106]. Of significant importance are the surface or interface reflection and transmission, through which the phase, amplitude, polarization of the incident wavefront are modified abruptly, resulting in a new wavefront of the reflected, transmitted or even guided

waves that can be designed at will [5, 107, 108, 106].

To be general, a 2D/3D structure composed of scatterers arranged with a subwavelength spacing can be called a metasurface/metamaterial. Scatterers are usually laid out in a periodic format; its periodicity (Λ) with respect to the wavelength of interest (λ) is a key parameter to differentiate a metasurface/metamaterial ($\Lambda < \lambda$) from an effective medium that can be described by classical mixing formulas ($\Lambda \ll \lambda$) or an photonic bandgap structure where higher-order Floquet-Bloch modes are excited ($\Lambda > \lambda$) (see Fig. 2.1) [5]. The characteristic resonance of metasurface are predominantly determined by the resonance associated with the scatterers, while slightly affected by the resonance associated with the periodicity. To operate in this region, the periodicity has to be subwavelength to only allow for the zeroth-order Floquet-Bloch mode, and the scatterers' resonance needs to be designed at frequencies below the first higher-order Floquet-Bloch mode. Otherwise, the resonance with the scatterers will couple strongly with the Floquet-Bloch mode, resulting in a undesired leak of energy to the propagating modes along the metasurface.

As a rapidly growing research field, metasurface has been studied over a wide spectral range from microwave to optical frequencies, resulting in a wealth of functionality including beam collimation [109–111], anomalous reflection and refraction [112–115], vortex plates [112, 116, 115, 117], waveplates [118], flat lenses and axicons [119–121], polarization converters [122, 123], free-space propagating wave to surface wave convertor [124], surface wave guiding [125–128], amplitude and phase modulators [129], etc. The fundamental building block of metasurfaces — scatterers (a.k.a. "optical antennas") structured and arranged on a subwavelength scale — can take a variety of forms such as metallic grooves engineered to

support "spoof surface plasmon", single-layer metallic antennas of various shapes, metallic refectarrays, and dielectric resonators.

A metallic-dielectric interface support surface plasmons, which are a form of electromagnetic wave that couples coherently with electronic oscillations and propagates along the interface. It is known for the subwavelength field confinement and enhancement adjacent to the metal surface, which offers the exciting possibility of light manipulation. Difficulties of using surface plasmons rise in long wavelengths such as infrared and terahertz, because the plasmon frequency for most metals is in the ultraviolet and hence metals behave more like a perfect conductor at long wavelengths, leaving the surface plasmon loosely bound to the metal surface [111]. This issue is addressed by metasurfaces consisting of metallic groove textures on a deep-subwavelength scale, which is designed to support tightly confined surface waves at long wavelengths [130]. Since the dispersion of these surface waves resembles a surface plasmon, they are referred to as spoof surface plasmon. The plasmonic frequency is engineerable with the grooves geometry and can be significantly lowered to achieve a much enhanced field confinement to the metal surface. Second-order grating is further embedded to the metallic grooves to scatter the spoof surface plasmon to free space, which has been demonstrated as an effective beam collimator for mid-infrared and THz QCLs [109–111].

The plasmonic resonance can be engineered merely by a thin-layer metallic antenna (with negligible thickness compared to one wavelength) on a dielectric substrate [112, 131]. If a single antenna resonance is involved, such a single-layer metallic antenna gives π phase shift across the resonance [107, 132]. To achieve 2π phase tuning to be truly useful for arbitrary phase front engineering, multiple independent resonances, coupled antenna resonances, or

geometric effects (i.e. Pancharatnam-Berry phase) are commonly employed in designs [106]. For example, the famous V-shaped metallic antennas proposed by Yu, et.al support the two plasmonic eigenmodes with different resonant properties [112, 132]; the excitation of each mode is designable with the antenna geometry. This is further combined with the geometric effect induced by varying antennas' spatial orientation, which leads to a coverage of the entire 2π range with a constant scattering amplitude. This concept has been applied to produce flat optics that can reflect and refract light to arbitrary directions, focus beam as a lens or axicon, converts a uniform wavefront to a vortex beam or a circularly-polarized beam [112, 118]. One limitation of single-layer metallic antenna is its low scattering efficiency (10-20% in this case) due to the low quality-factor associated with the antenna resonance (i.e. high radiative loss) [106]. As a result, a considerable amount of energy is wasted without being converted into the designed beams.

Another type of metallic metasurface is reflectarrays, which is a concept originally developed in the microwave and millimeter regime mostly for beam focusing and steering in the reflection setup [133, 134]. An array of microstrip patches or dipoles are printed on a subwavelength thin dielectric substrate with metal coated on the backside; the dimension of microstrip element is varied spatially to scatter the incident field from a feed antenna with the proper phase to achieve the designed phase front; this is essentially enabled by the $\sim 2\pi$ phase change as the microstrip resonance is tuned across the design frequency [135]. This concept has been extended to higher frequencies by scaling down the dimension [136, 137]. A significant advantage of using reflectarray is the much improved scattering efficiency, which reaches 80% in the anomalous reflection demonstration [138]. This is attributed to the

high-Q resonance associated with the microstrip antenna structure, because the radiation is primarily through the fringing field, rather than the electric current flowing on the top metal, which does not radiate due to the mirror image of opposite sign induced by the back metal plane [139]. In fact, the metal-metal waveguide structure widely used for THz QCLs is essentially a terahertz version of microstrip [140–142]. Therefore THz QCLs provide a natural and convenient platform to realize reflectarray metasurface concepts. More importantly the QC material sandwiched between the two metal layers in replacement of passive dielectric substrate provides another degree of freedom for metasurface engineering — gain, which is simply supplied by adding biases across the microstrip.

Other than altering phase or amplitude response by varying the antenna structure to tune resonance frequency, one can also tailor the phase response using the so-called Pancharatnum-Berry phase [143–145]. An anisotropic scatterer can scatter a circularly-polarized light with one handedness to another with the opposite handedness plus an additional phase change. The mount of phase change is proportional to the orientation angle of the anisotropic scattered and a 2π change is induced with the scatterer rotated from 0 to π [146]. This phase change is defined as Pancharatnum-Berry phase. This property has been utilized to demonstrate many functionality such as focusing or diverging lenses [147, 117], vortex beam plates [115], metasurface holograms [138, 148]. Metasurfaces of this type show ultra-broadband performance and high efficiency [149], as it is free from the wavefront distortion induced by the antenna dispersion as the frequency deviates from the designed one.

Suppression of reflection is preferable for metasurfaces designed for controlling transmitted light to achieve a high efficiency. Huygens' metasurfaces have been proposed to control

both electric and magnetic response of the scatterers to achieve this goal [150]. This is done by engineering the electric sheet admittance and magnetic sheet impedance Y_{es} and Z_{ms}, of the metasurface to achieve $\sqrt{Z_{ms}/Y_{es}} = \eta_0$, where η_0 is the impedance of the surrounding media. One can vary Y_{es} and Z_{ms} simultaneously to ensure a phase variation from -π to +π while maintaining the impedance matching condition. This concept has been first demonstrated in the microwave region using copper traces and loops patterned on top and bottom of a dielectric substrate, showing a transmission efficiency as high as 86% [150]. To adapt Huygens' metaurfaces to optical frequencies, cascade metasurfaces have been designed using optical nanocircuits as the building block [151], though which beam deflectors [152] and flat lenses have been realized [153].

Metasurfaces made of low-loss and high-refractive-index dielectric scatterers are attracting increasing attentions, particularly in the optical frequency range, since the ohmic loss of metallic metasurfaces increases with frequency owing to the increased penetration depth in metals. Another unique property of dielectric scatterer is that both electric and magnetic resonances can be tuned, which enables phase tuning over the entire 2π range [120, 122] and the realization of dielectric Huygens' metasurfaces [154]. Dielectric metasurfaces based on Pancharatnam-Berry phase have also be realized [117].

Metasufaces demonstrated so far mostly function as passive devices. However, increasing efforts have been devoted to integrating electrically- or optically-controllable functions into metasurfaces to realize active metasurfaces with tunable resonances. Examples include metasurfaces with the transmission tunable by photoexcitation [155], metasuface amplitude and phase modulator enabled by integrated diodes and Schottky junctions [129, 156, 157],

graphene-integrated metasurfaces with electrically-tunable resonance [127]. Metasurfaces also offer a platform ideal for enhancing nonlinear effects [158–160], thanks to the ability of strong subwavelength field enhancement and relaxed phase matching requirement. Nevertheless, there has been relatively little experimental work on integrating gain into the metasurface itself, whether simply for mitigating losses, or for implementing new laser concepts [161–165]. This is understandable, since in the infrared and visible the metallic/plasmonic elements that make up many metasurfaces are prohibitively lossy [166]. However, the situation is quite favorable in the THz frequency range, where metals have sufficiently modest losses so that THz QCLs can effectively use sub-wavelength metallic waveguides [140].

2.2 Baseline design of active metasurface

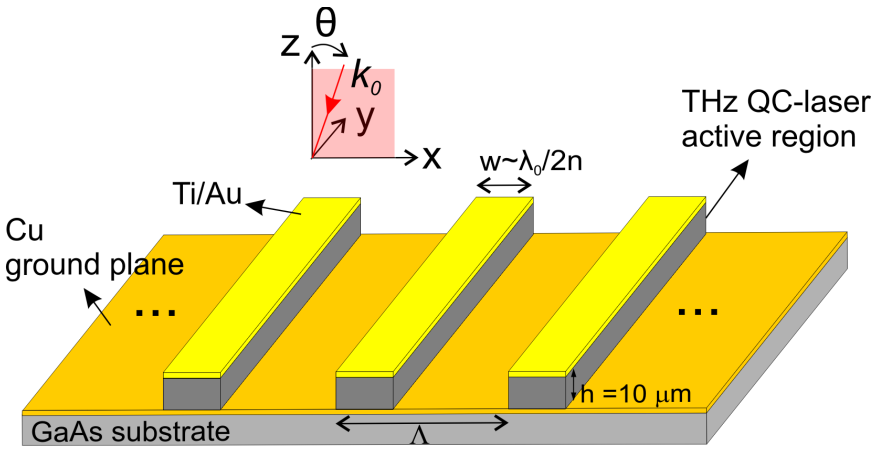

Figure 2.2: Schematic of an active metasurface design consisting of period arrays of MM waveguide microcavity of width w, height h and period Λ.

THz QCLs based on metal-metal waveguide structures offer a model system ideal for implementing reflectarray metasurfaces with the QC gain incorporated. Based on it, the active

reflectarray metasurface reflector is proposed to exploit the QC gain to realize amplified reflection. A baseline form of the active metasurface reflector is composed of a sparse array of identical metal-metal (MM) waveguide ridges, a schematic of which is shown in Fig. 2.2. Each ridge is made up of GaAs/AlGaAs multiple-quantum-well QC active material (usually 10-μm thick), with metal cladding/contacts directly above and below. When electrically biased, the material provides a gain described by the bulk material gain coefficient $g(\nu)$. While MM waveguides are usually intended to support a confined and guided mode, in this case we wish them to act as surface emitting antennas; each element couples in incident THz radiation polarized transverse to the ridge axis (i.e. x-axis shown in Fig. 2.2), amplifies it via stimulated emission, and re-radiates it back into free space, resembling an elongated microstrip patch antenna [141, 142, 167, 168]. The ridge width w is designed to produce a resonance at the wavelength of interest λ_0, which approximately corresponds to $w \approx \lambda_0/n$, where n is the refractive index of the QC active material. This is essentially the lowest order standing wave in a very short cavity of length w. From the waveguide perspective, each MM ridge can be thought of as operating at or near the cutoff frequency ω_c of the MM waveguide's first higher-order lateral mode (TM_{01}), which locates within the light line, indicating a leaky mode that radiates to the free space in contrast to the bound propagating modes outside the light line (see Fig. 2.3(a)). The ridges are spaced with period Λ designed to be less than the λ_0 (e.g. the intended laser emission wavelength), in order to suppress higher-order Bragg diffraction — only zeroth-order (specular) reflection occurs. As will be discussed later, for $\Lambda \ll \lambda_0$ this resonance frequency is predominantly determined by the ridge width w and only slightly affected by the period Λ. However, as the period approaches the free-space wavelength λ_0, a coupling occurs between the localized resonance and a propagating Bloch

Table 2.1: Relevant Drude parameters used for Au and active medium.

Material	Carrier density N (cm^{-3})	Carrier lifetime τ	Effective electron mass m^*	Core permittivity ϵ_{core}
Au [169]	5.9×10^{22}	39 fs (at 77 K)	m_0	ϵ_0
Active medium [170]	5×10^{15}	0.5 ps (at 77 K)	$0.067m_0$	$12.9\epsilon_0$

surface wave.

Numerical simulation of the metasurface's reflection spectra under normal incidence of radiation ($\theta = 0^\circ$ in Fig. 2.2) is conducted using a full-wave finite-element electromagnetic solver (COMSOL 5.2), in which a 2D unit cell of metasurface is modeled with Floquet periodic boundary conditions applied to depict an infinite structure. The Drude model was used to describe the free carrier scattering loss in GaAs/AlGaAs and gold metallization that accounts for the loss in the metasurface, the parameters of which are listed in Table 2.1. The details of the Drude expressions used are presented in Appendix A. Fig. 2.3(c) shows a set of simulated reflectance spectra for a group of metasurfaces with different ridge widths ranging from 11–12.5 μm and a fixed periodicity $\Lambda = 70$ μm for two scenarios: passive with $g = 0$ cm^{-1} and active with $g = 30$ cm^{-1} in the QC material. As expected, reducing the width w leads to a higher resonance frequency. Fig. 2.3(d) shows the reflectance increases with gain for the metasurface with $w = 11.5$ μm and $\Lambda = 70$ μm at its resonance frequency 3.4 THz and two other frequencies above and below the resonance. As shown in Fig. 2.3(d) the reflectance R_{MS} increases with the gain g; it is useful to fit these numerical results to the relation

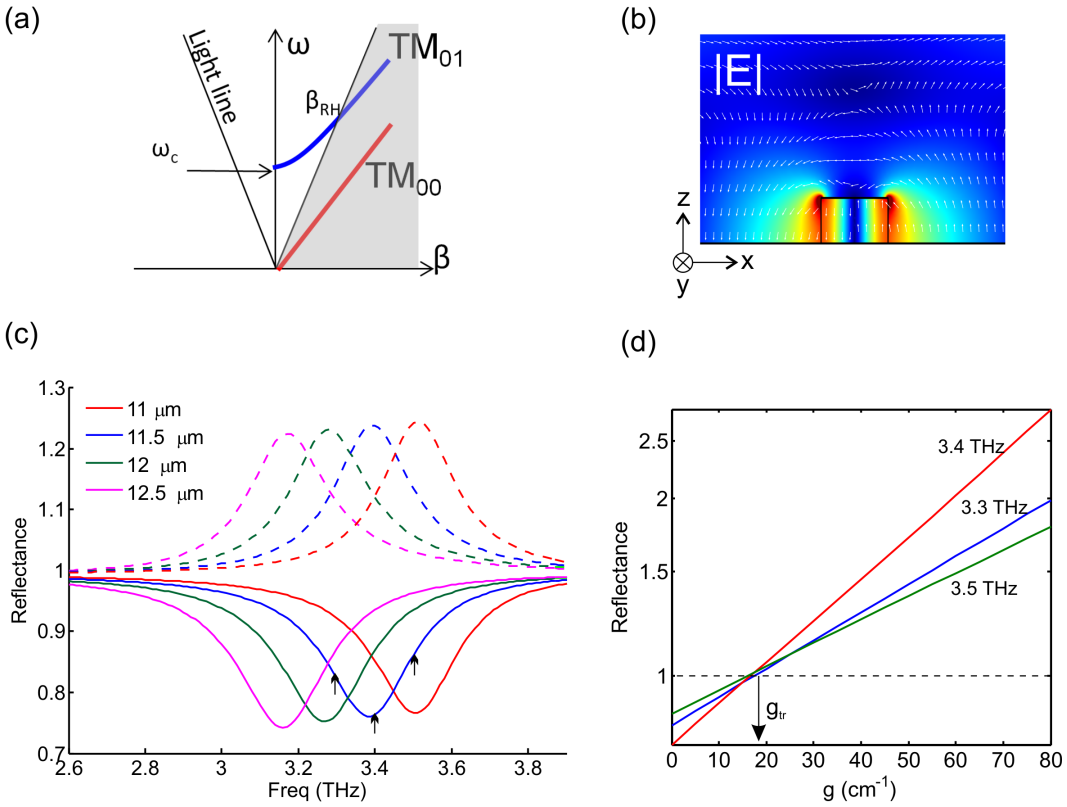

Figure 2.3: (a) Schematic dispersion diagram of TM_{00} and TM_{01} modes for a MM waveguide. (b) E-field profile for the TM_{01} mode excited under normal incidence at the resonant frequency of 3.4 THz for a metasurface with $w = 11.5$ μm and $\Lambda = 70$ μm. (c) Simulated reflectance spectra for four metasurfaces with ridge widths varying from 11–12.5 μm and fixed period $\Lambda = 70$ μm. The solid lines are results for passive metasurface with $g = 0$ cm^{-1}, and the dashed lines are for active metasurface with $g = 30$ cm^{-1}. (d) Simulated reflectance change (plotted in log scale) with medium gain g for a metasurface with $w = 11.5$ μm and $\Lambda = 70$ μm at three different frequencies respectively below, at and above the resonant frequency of 3.4 THz, as indicated by the black arrows in (c). The transparency gain g_{tr} is almost fixed.

$$R_{MS} = R_1 G = e^{\xi(\nu)(g - g_{tr})} \tag{2.1}$$

where R_1 is the passive metasurface reflectance at frequency ν, G is the reflective intensity gain, g_{tr} is the transparency gain coefficient needed to balance absorption losses (from the metal and semiconductor) so that $R_{MS} = 1$, and $\xi(\nu)$ is a fitting coefficient that contains information about the metasurface frequency response and Q-factor. Gain is more efficiently coupled to incident radiation when the operation frequency is closer to the resonance, which is represented by a higher value of $\xi(\nu)$ and thus a larger slope of the curves plotted in Fig. 2.3(d). The transparency gain g_{tr} stays almost unchanged with operation frequency, which is $\sim$17 cm^{-1} here. This amount of gain is readily achievable by QC gain materials, which are typically capable of supplying 50–100 cm^{-1} of bulk gain. Back to the fundamental obstacle that inhibits implementing VECSEL concepts for QCLs — intersubband selection rule, it is apparent that this rule is satisfied in this baseline metasurface design, as the excited TM_{01} mode has its E-field inside the gain medium predominantly polarized perpendicular to the quantum wells (see Fig. 2.3(b)). In these simulations, a frequency-independent gain is assumed for the active medium, so that the metasurface response can be analyzed independently of the choice of active material. In reality, the gain will have its own lineshape; the general design goal is to match the metasurface resonance with the peak gain frequency of the gain medium. In practice, this is typically accomplished by first measuring the lasing spectrum of a conventional MM waveguide QCL fabricated from the same active material, and then designing the metasurface dimensions around the measured values.

2.3 Bragg scattering suppression

Despite the resemblance of metasurface shown in Fig. 2.2 to a grating, the primary mechanism of operation for the metasurface is not Bragg-scattering. Rather, each microcavity antenna is locally self-resonant on the unit cell level, consistent with the characteristics of metasurface resonance within Region $\Lambda < \lambda$ of Fig. 2.1. This is readily seen in simulated absorption ($A = 1 - R_{MS}$) spectra from a passive metasurface with ridge width w varied in a large range from 6–13 μm and period Λ fixed at 70 μm, shown in Fig. 2.4. Two bands are observed in this dispersion map. For a large ridge width (>9 μm), the lowest frequency mode is the localized microcavity resonance; it scales inversely with w, and has a relatively broad bandwidth due to the low radiative Q-factor of the antenna (Q $\sim$ 10-15 in simulation). The higher frequency band at and above $\sim$4.3 THz represents a propagating surface Bloch waves that couples to normally incident radiation via Bragg scattering when $\lambda_0 \approx \Lambda$ or $\lambda_0 < \Lambda$. The passive reflectance spectra for ridge widths varying from 11–12.5 μm in Fig. 2.3(c) are the line cuts from the part within the white dashed box on this spectral map, which exclude the high frequency region containing Bragg scattering features. However, as the ridge width is reduced, the microcavity mode resonance increases in frequency and hybridizes with the surface Bloch wave mode, which is characterized by an anti-crossing feature. This is accompanied by an increase in the radiative Q of the microcavity mode and an increased dependence on Λ of the resonance frequency, a phenomenon which has been observed in a variety of coupled systems [171, 172]. Despite the higher Q of the surface Bloch wave, this mode is undesirable for VECSEL operation, since it is less confined to the active region, and for a finite sized metasurface it is associated with considerable scattering and

diffraction losses. Thus, we typically confine the metasurface within the design space where the microcavity mode resonance is clearly distinct from the surface Bloch wave.

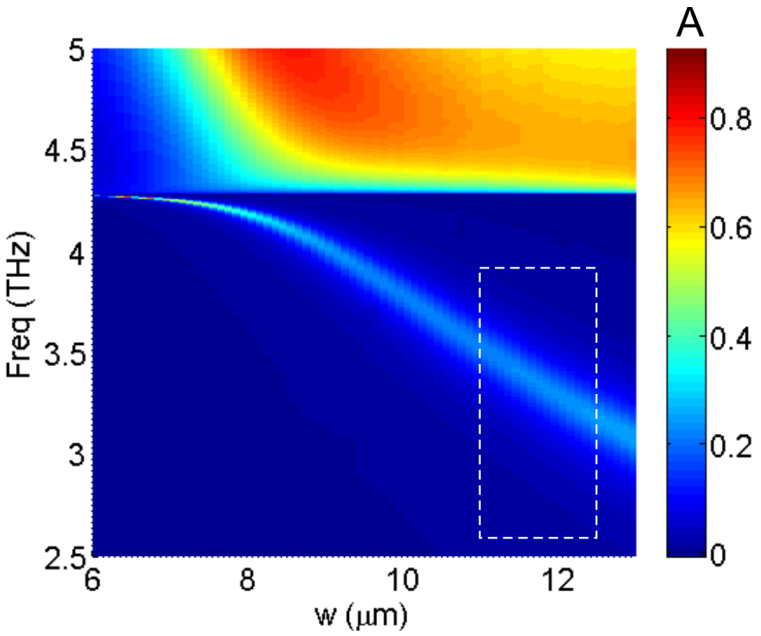

Figure 2.4: Colormap of the simulated absorption ($A = 1 - R_{MS}$) spectra for a passive metasurface with ridge width w varied from 6–13 μm and period Λ fixed at 70 μm. Spectra shown in Fig. 2.3(c) are vertical cuts within the white dashed box.

A further complication arises due to the fact that a finite sized beam incident upon the metasurface will contain components with non-zero transverse momentum, i.e. obliquely incident components could more easily excite the surface Bloch wave than normally incident waves [173]. For a non-zero incident angles θ as defined in Fig. 2.2, this excitation occurs at a frequency lower than the first-order Bragg diffraction cutoff frequency of c/Λ. For example, in one of the early metasurface designs for 2.7–3.0 THz, we chose period $\Lambda = 90$ μm (corresponding to $c/\Lambda \sim 3.33$ THz), with the ridge width varied from 11.5–13.5 μm to overlap with the gain peak [174]. The reflectance spectra have been measured using Fourier transform infrared spectroscopy (FTIR) for these five metasurfaces, nominally at normal incidence (see Fig. 2.5(a)). First, as expected, resonances are only observed when

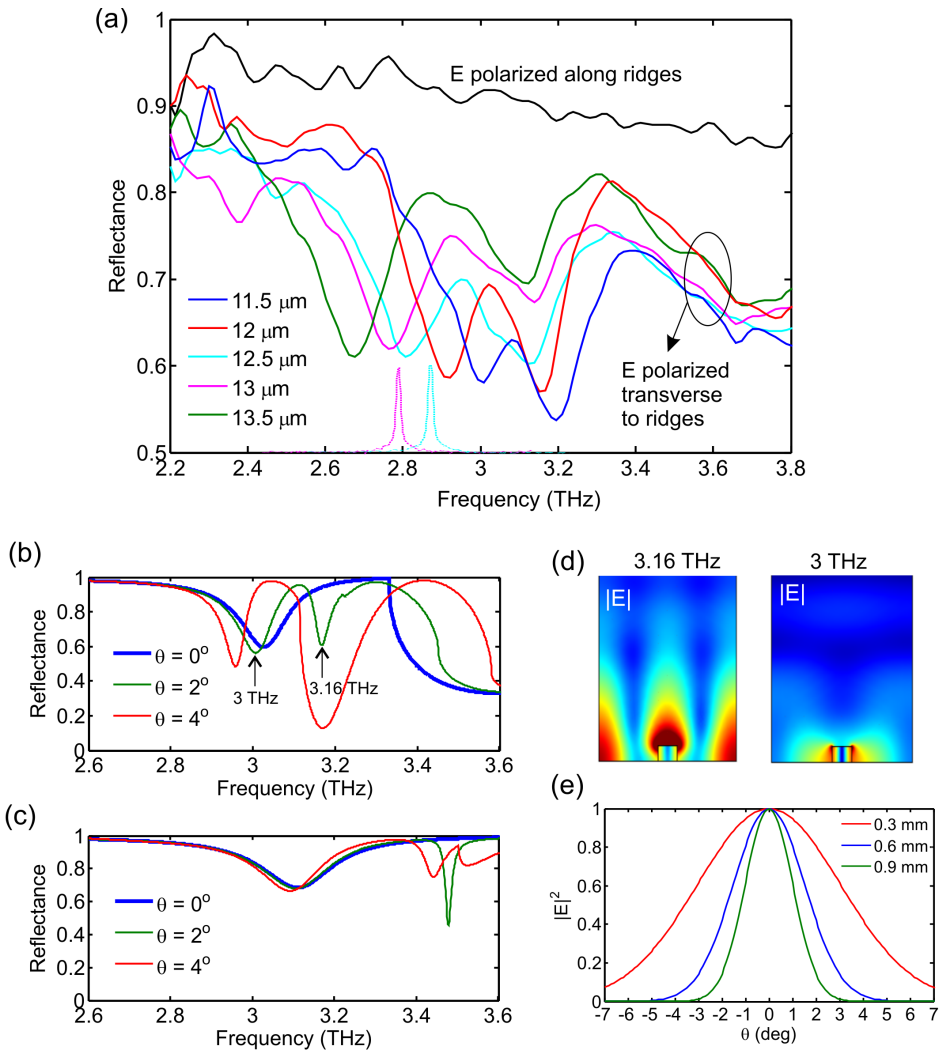

Figure 2.5: (a) Measured reflectance spectra for five metasurfaces with ridge widths ranging from 11.5–13.5 μm and $\Lambda = 90$ μm, with the incident E-field polarized transverse to the ridges. The reference used is a flat gold surface. The lasing spectra measured at 77 K for two QC-VECSELs based on $w = 12.5$, 13 μm metasurfaces are plotted in the corresponding color below the reflectance spectra. (b) (c) Simulated spectra for a metasurface with 12.5 μm ridge width and $\Lambda = 90$, 80 μm under plane wave incidence at different angles θ. (d) Excited surface Bloch mode at 3.16 THz and TM_{01} microcavity mode resonant at 3 THz on the spectrum at θ =2° in (b). (e) Decomposition of Gaussian beams with different beam widths at 3 THz into plane wave components with amplitude $|E|^2$ plotted as a function of the propagation angle θ.

the incident radiation is polarized transverse to the ridge axis. Second, the spectra clearly show two absorption features, corresponding to the microcavity mode resonance and guided mode excitation. As w decreases, the resonance frequency increases. For $w = 11.5$ μm and 12 μm designs, the resonances become strongly coupled and an anticrossing is observed. This is consistent with our experimental observations: VECSEL designs based upon $w = 12.5$, 13 μm metasurfaces were observed to lase (see spectra in Fig. 2.5(a)), while designs with w = 12, 11.5 μm did not lase, despite the fact that the active material was known to have strong gain at those frequencies. A metasurface with $w = 13.5$ μm did not exhibit lasing likely due to the spectral mismatch between metasurface resonance and the gain medium. The effect of the surface wave is also manifested in reflectance spectrum simulations for a metasurface ($w = 12.5$ μm, $\Lambda = 90$ μm) under plane wave incident from different angles, as seen in Fig. 2.5(b). Since it is an infinite structure simulation, for normal incidence $\theta = 0^\circ$ the localized microcavity resonance is at 3.0 THz, and the first-order Bragg diffraction is observed starting at ∼3.33 THz (almost exactly c/λ_0). For $\theta = 2^\circ$, a surface guided mode is excited at 3.16 THz, which is bound to the metasurface and propagates in the transverse direction, as Fig. 2.5(d) shows. This is very different from the localized microcavity mode excited at 3 THz (see Fig. 2.5(d)). The coupling of two modes also narrows and shifts the microcavity mode resonance dip. This impact increases with a larger incident angle as the guided mode excitation occurs at a lower frequency. The key strategy to suppress the impact of the surface wave is to further reduce the period Λ compared to λ_0 — perhaps more than would be initially expected. As seen in Fig. 4(c), by reducing Λ from 90 μm to 80 μm, the guided mode excitation is pushed to frequencies much higher than the microcavity resonance and therefore slightly affected by oblique incidence. The primary drawback to this strategy

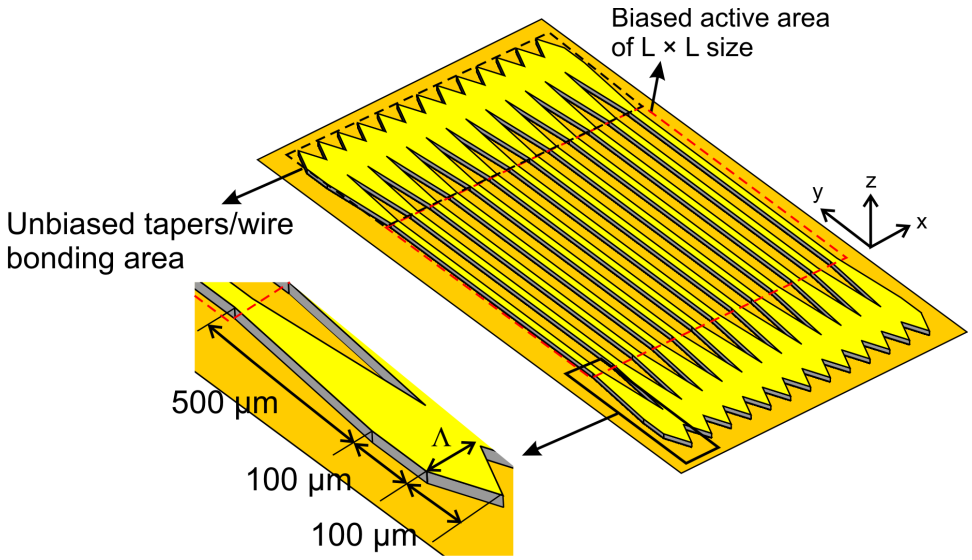

Figure 2.6: Schematic of an example design of unbiased tapers/wire bonding area.

is the desire to minimize the fill factor w/Λ to minimize the thermal dissipation per unit metasurface area, which is especially important for THz QCL cw performance. Suppression of Bragg scattering induced by the wave components with non-zero transverse momentum become increasingly critical for beams of smaller sizes. This is reflected in the decomposition of Gaussian beams of varying beam waists, which suggests a smaller size Gaussian beam has more energy contained in plane wave components with non-zero incident angles, as shown in Fig. 2.5(e). So far, a design rule of thumb is developed to keep $\Lambda \leq 0.8\lambda_0$ to prevent the Bragg scattering effect.

2.4 Self-lasing suppression

The designed active metasurface is supposed to form a VECSEL cavity with an external output coupler. As long as the reflective gain from the amplifying metasurface is sufficient to compensate for the cavity loss and output coupling loss, lasing is likely to occur in the

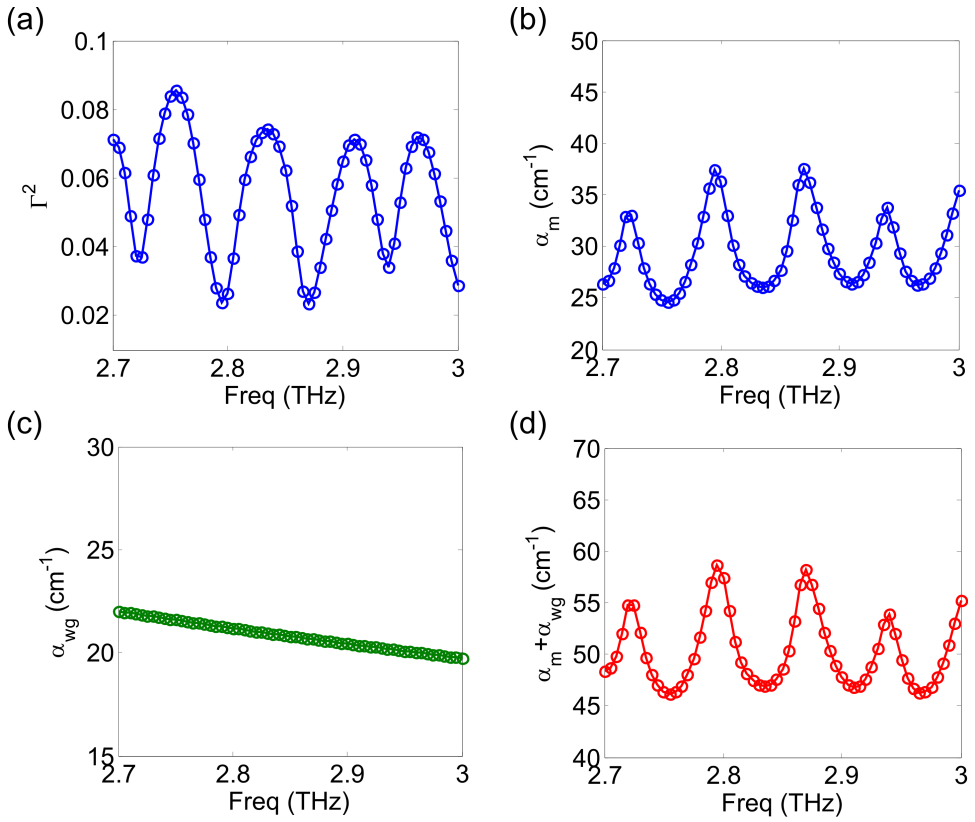

Figure 2.7: (a) Simulated reflectance Γ^2 at the intersection between the MM waveguide and taper for TM_{01} mode. (b) Mirror loss α_m for a biased MM ridge of 1-mm length. (c) Waveguide loss α_{wg} of the MM ridge of 12.5-μm width. (d) Self-lasing threshold calculated by $\alpha_m + \alpha_{wg}$.

VECSEL cavity that is engineered to support near-Gaussian profiles. However, owing to the fundamental nature of lasing behavior — lasing always prefers to occur in the lowest-loss mode that requires the lowest amount of gain, an active metasurface might self-oscillate in low-loss individual or collective sub-cavity modes. The metasurface self-lasing behavior that occurs in the absence of an external cavity will steal the gain from the desired VECSEL mode and even prevent VECSEL lasing. To tackle this potential risk, strategies of loss engineering are used to suppress metasurface self-lasing. First, for the baseline metasurface designs comprising an array of MM microcavities, each microcavity is designed to operate at TM_{01} mode cutoff as a leaky-wave antenna. The radiative Q-factor associated with this mode is very low ($\sim$10-15 extracted from Fig. 2.3(c)) so that each sub-cavity will not self-oscillate at this operating point. Second, each microcavity also supports a highly confined propagating TM_{00} waveguide mode as well as propagating TM_{01} mode, which in dispersion diagram locate outside the light line as Fig. 2.3(a) shows. To suppress self-lasing in these propagating waveguide modes, absorbing boundary conditions are placed at the terminations in the form of lossy tapers and wire bonding area to significantly reduce the facet reflection and thus increase the lasing threshold. The lossy condition is realized by depositing an insulation layer between the top metal contact and the QC active material to prevent the active medium in these designated areas from being biased. The shape of lossy tapers and wire bonding areas are designed based on a graduated labmate Dr. Philip Hon's linear taper design [175]. An example design is shown in Fig. 2.6. The reflectance Γ^2 for TM_{00} mode at the intersection between the MM ridge ($w = 12.5$ μm, $\Lambda = 90$ μm) and taper is simulated using a 3D full-wave numerical model (see Fig. 2.7(a) for Γ^2), which can be converted to the waveguide mirror loss $\alpha_m = \ln \Gamma^2 / L$. For a typical biased ridge length of 1 mm, α_m

is plotted in Fig. 2.7(b). Combining the simulated waveguide loss α_{wg} for MM waveguide TM_{01} mode, the self-lasing gain threshold that equals to $\alpha_m + \alpha_{wg}$ is plotted in Fig. 2.7(c). The threshold is higher with a smaller bias area. The self-lasing threshold is on the edge of the QC bulk gain capability, which is typically ∼50–100 cm^{-1} for QC materials, while in contrast the QC-VECSEL lasing threshold can be engineered to ∼30 cm^{-1} or even lower (see Sec. 4.2). Therefore lasing in the desired VECSEL mode is ensured.

2.5 Other metasurface designs

Other than the baseline metasurface, there are a multitude of metasurface designs that can be exploited to build up QC-VECSELs, offering considerable freedom to the engineering of QC-VECSELs' various properties. In this section, another two alternative metasurface designs are presented and discussed: TM_{03} MM waveguide microcavity array and MM patch array. In Chapters 5–8, advanced designs including inhomogeneous focusing metasurfaces and polarization-switchable metasurfaces will be detailed with experimental results.

The TM_{03} MM waveguide microcavity array design utilize the higher odd-order transverse resonant mode (i.e. TM_{0N}) in a MM waveguide that couples to the normally incident radiation around the corresponding cutoff frequency $f_{0N} = N\frac{\pi c}{nw}$, where N is an odd integer number. $N = 3$ is chosen for TM_{03} design and $N = 1$ for the baseline metasurface design. An example design of TM_{03} MM waveguide microcavity array and the simulation results are shown in Fig. 2.8 (a)–(c), which exhibits a TM_{03} transverse resonance at 3.4 THz with the ridge width $w = 35.6\,\mu$m and periodicity $\Lambda = 70\,\mu$m. The amplification of reflected wave at resonance is clearly seen from the reflection simulation with bulk gain increased. TM_{03}

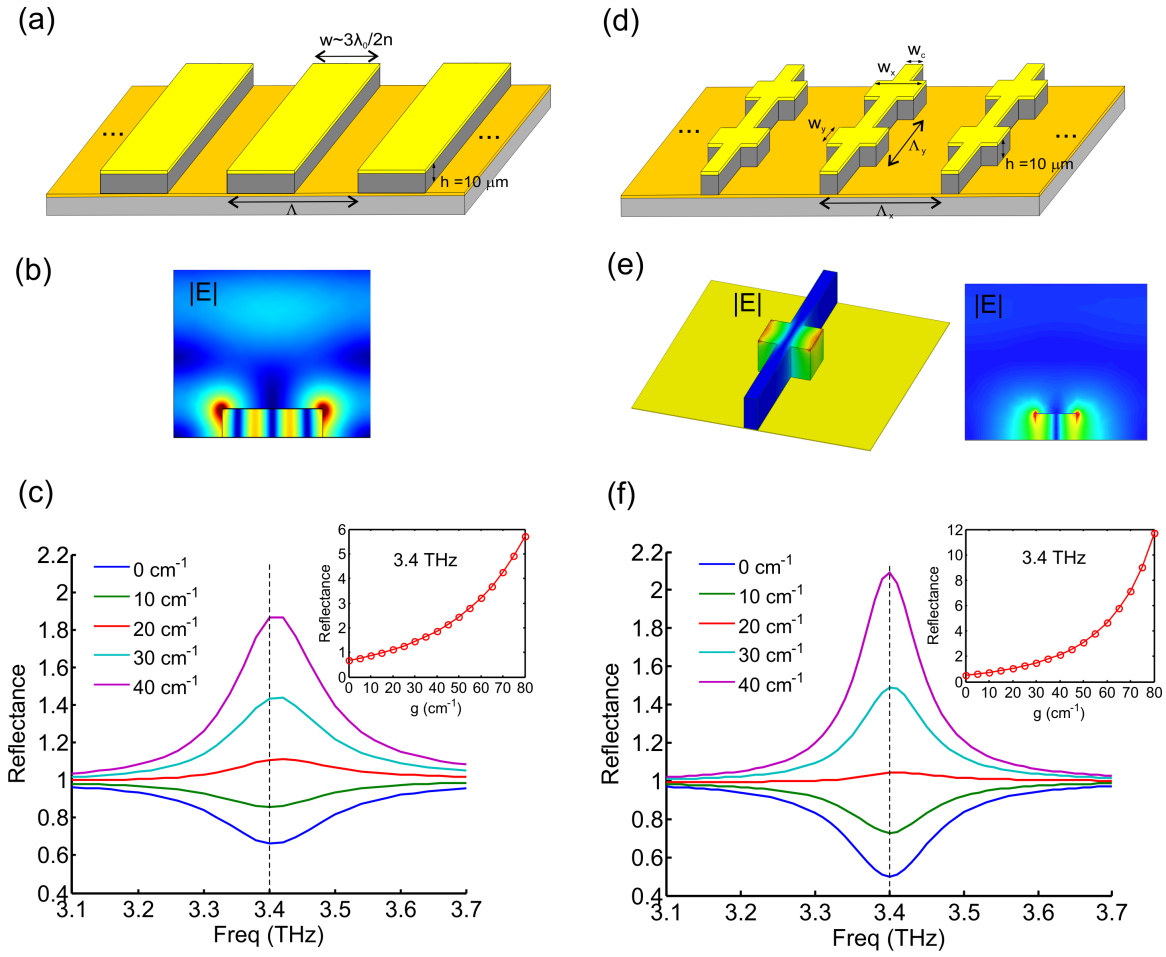

Figure 2.8: (a) TM_{03} MM waveguide microcavity array design. (b) Excited TM_{03} mode profile. (c) Simulated reflectance spectra at different bulk gains for the TM_{03} metasurface with $\Lambda = 70\,\mu$m, $w = 35.6\,\mu$m. Inset is the reflectance change with bulk gain g at the resonant frequency 3.4 THz. (d) MM patch array metasurface design. (e) Excited TM_{01} patch resonant mode profile. (f) Simulated reflectance spectra at different bulk gains for the patch array metasurface with $\Lambda_x = \Lambda_y = 70\,\mu$m, $w_x = 15.3\,\mu$m, $w_y = 11.5\,\mu$m, $w_c = 4\,\mu$m. Inset is the reflectance change with bulk gain g at the resonant frequency 3.4 THz.

metasurface design offers an approach to scale up the output power by increasing the active material fill factor $F = w/\Lambda$ without increasing the device footprint and the QC material cost. This, however, might lead to some degradation in thermal and cw performance due to higher density of heat generated. So this design is preferable for achieving QC-VECSELs aimed at high peak pulsed power.

In contrast, the second metasurface design composed of connected MM patch array features a very low active fill factor and therefore efficient heat removal, which makes it a promising design to achieve improved high-temperature and cw performance. An example design is shown in Fig. 2.8(d), where an array of patches are connected by narrow connectors of width w_c to provide continuous electrical bias over all patches. As Fig. 2.8(e) shows, the excited resonant patch mode takes TM_{01} mode-like profile as seen in the baseline metasurface design in the transverse direction parallel to the incident wave polarization, while stays nearly uniform in the longitudinal direction. The simulated refection spectra with bulk gain varied are plotted in Fig. 2.8(f), which also exhibits the amplifying effect with sufficient bulk gain provided.

Besides the thermal consideration, one can also compare different metasurfaces by two characteristic parameters: g_{tr} and ξ, as defined in Eq. 2.1, which respectively reflects the intrinsic loss and the radiative Q-factor associated with the resonators on the metasurface. Generally speaking, metasurfaces with lower g_{tr} and higher ξ are preferred in most QC-VECSEL setups in terms of the power output level. Detailed discussion will be presented in Sec. 3.4 following the proposal of the laser model, which is needed to relate these two parameters with the QC-VECSEL performance.

2.6 Fabrication process

The fabrication of metasurfaces generally follows the standard process for making MM waveguide QCLs [76]. Cu-Cu thermocompression bonding is used to bond the 10 μm-thick active layer to a receiving GaAs wafer, followed by lapping and selective wet-etching of the substrate. Then $\sim$200 nm of SiO_2 is deposited and patterned to isolate the taper and wire bonding area from being biased, followed by evaporation and lift-off of Cr/Au/Ni to provide the top metallization and self-aligned etch mask. The metal-metal waveguide ridges are then defined by the Chlorine-based dry etching with the subsequent removal of the Ni layer. The fabrication flow is briefly illustrated in Fig. 2.9. All the demonstrated metasurfaces were fabricated using UCLA Nanolab facilities. The detailed recipes of each step are given in Appendix B.

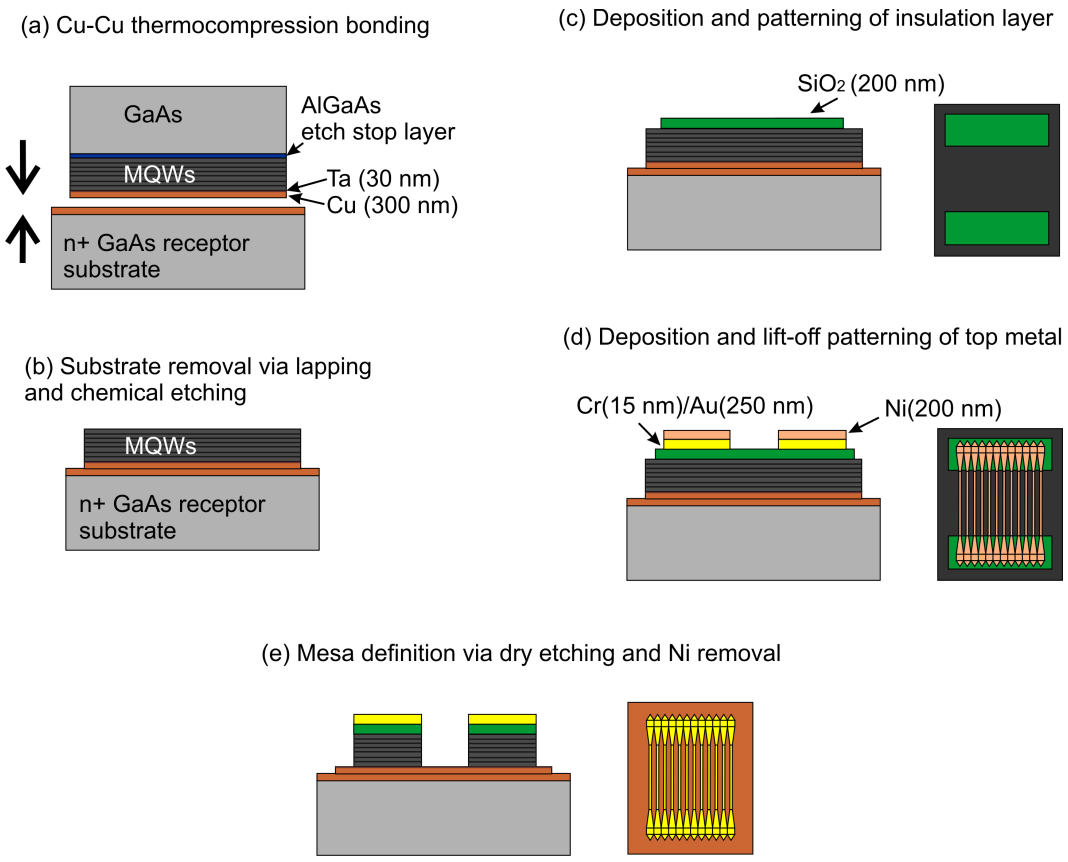

Figure 2.9: (a)-(e) Metasurface fabrication flow.

CHAPTER 3

Laser model for metasurface QC-VECSELs

In this chapter, a basic formalism is derived to describe the threshold condition and slope efficiency for an idealized metasurface QC-VECSEL. This sets the basis for the subsequent discussion on the effect of multiple design parameters for metasurfaces on the QC-VECSEL performance, including the bias diameter on the metasurface and the radiative Q-factor of the metasurface.

3.1 Derivation of the threshold condition and slope efficiency

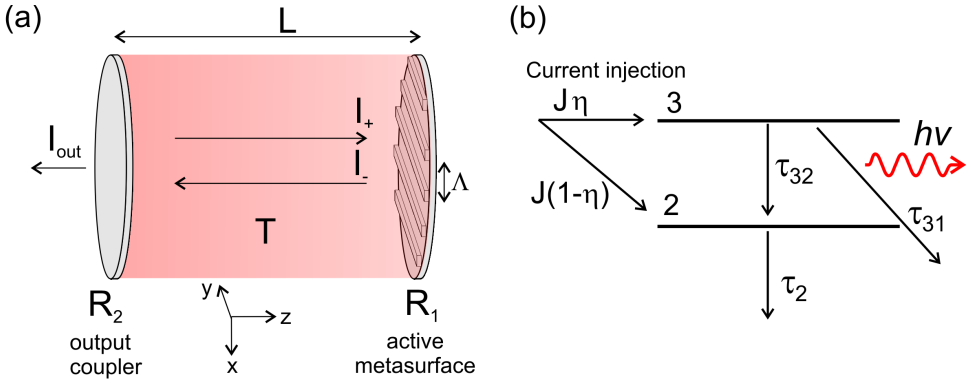

Figure 3.1: (a) Schematic of idealized metasurface VECSEL cavity with mode area of A and length L, where the metasurface sub-cavity period is Λ. (b) Three-level model for QC-laser gain medium, where non-radiative relaxation times τ_{32}, τ_{31}, and τ_2 are explicitly shown. Level 1 (injector state) is not explicitly shown.

We consider a cavity as illustrated in Fig. 3.1, constituted between a metasurface reflector of area A with passive reflectance R_1, and an output coupler with reflectance R_2 and transmittance $T = 1 - R_2$. The incident and reflected circulating intensities are I_+ and I_- respectively, as defined just above the metasurface. We also include a single-pass transmittance T for the propagation over the cavity length L which includes the effect of diffraction loss, atmospheric absorption, and cryostat window transmission. The metasurface produces a uniform power gain $G = e^{\xi g}$, so that its active reflectance is equal to $R_1 G$. The bulk gain coefficient of the active QCL material at the cavity mode frequency ν is $g{=}g(\nu)$. We assume for the moment that the intensity is uniform in the transverse direction, and that the mode area and metasurface area are identical; later we will modify our expression to account for a transverse confinement factor. Using Eq. 2.1 and requiring the intensity to be unchanged after one round trip, i.e. $|R_1 G R_2 T^2| = 1$, the threshold gain coefficient g_{th} is obtained as:

$$g_{th} = -\frac{\ln\left(T^2 R_1 R_2\right)}{\xi}. \tag{3.1}$$

To go further, we model the QC-laser active material as a 3-level system, as shown in Fig. 3.1(b). The upper radiative state 3 is pumped using tunneling current injection at a rate of $J\eta/eL_p$, where J is the current density, η is the injection efficiency, e is the fundamental charge, and L_p is the length of one cascade period. The remaining fraction (1-η) of current density is injected into the lower radiative state 2, which is then emptied by some combination of tunneling and electron-phonon scattering. The various non-radiative lifetimes are given by τ_3, τ_{32}, and τ_2. This is a standard treatment for QCL systems similar to that given in Refs. [1, 176]

Within the active material, we use a standard expression for the saturated gain coefficient for a homogeneously broadened gain transition:

$$g = \frac{g_0(J)}{1 + I_0/I_s} = \frac{(J - J_{leak})\,\sigma\tau_{eff}}{eL_p}\frac{1}{1 + I_0/I_s}, \tag{3.2}$$

where $g_0(J)$ is the unsaturated gain coefficient, which is assumed proportional to the pump current density J. J_{leak} is an empirical shunt leakage current. The effective upper state lifetime is given by $\tau_{up} = \tau_3\,(1 - \tau_2/\tau_{32})$, and the effective lifetime for population inversion is $\tau_{eff} = \eta\tau_{up} - (1-\eta)\tau_2$, which accounts for a non-unity injection efficiency η. For the case of $\eta = 1$ we see $\tau_{eff} = \tau_{up}$. The circulating intensity within each sub-cavity ridge is I_0, and the saturation intensity is $I_s = h\nu/\sigma\,(\tau_{up} + \tau_2)$. The stimulated emission cross section at the cavity frequency is $\sigma(\nu)$, such that $g(\nu) = \sigma(\nu)(n_3 - n_2)$, where n_3 and n_2 are the 3D population densities of levels 3 and 2 respectively. Setting the value $g = g_{th}$, we can obtain an expression for the intensity vs. current density:

$$I_0 = \frac{h\nu}{eL_p}\frac{\tau_{eff}}{\tau_2 + \tau_{eff}}\frac{(J - J_{th})}{g_{th}}, \tag{3.3}$$

where the threshold current density is:

$$J_{th} = \frac{g_{th}eL_p}{\sigma\tau_{eff}} + J_{leak}. \tag{3.4}$$

We now must relate the intensity I inside the microcavity to the open cavity circulating intensities. The field within each of the N microcavities centered at x_i can be well approxi-

mated by a standing wave field profile. The field within the cavity of length L can be then be approximated as

$$E = \underbrace{\hat{x}E_{+}\psi(x,y)\left(e^{ik_0 z} + r_1\sqrt{G_{th}}e^{-ik_0 z}\right)}_{open\ cavity} + \underbrace{\sum_{i=1}^{N}\hat{z}E_0\psi(x,y)\sin\left(\frac{\pi}{w}(x-x_i)\right)}_{inside\ sub-cavities\ only}, \tag{3.5}$$

where $\hat{x}$ is the unit vector transverse to the microcavity ridges, r_1 is the field reflection coefficient of the metasurface, and $\psi(x,y)$ is a slowly varying transverse modal profile (assumed for now to be unity – i.e. a top-hat beam). Conservation of energy requires

$$A(I_{-} - I_{+}) = \frac{dU}{dt} = \frac{\omega_0 U_0}{Q_{abs}}, \tag{3.6}$$

where U_0 is the electromagnetic energy stored inside the antenna microcavity, ω_0 is resonance frequency, and Q_{abs} represents the nonradiative quality factor of the microcavity that accounts for the absorption loss. We write U_0 based on 3.7:

$$U_0 = AF\frac{1}{4}\varepsilon_r\varepsilon_0 E_0^2 h, \tag{3.7}$$

where h is the microcavity height determined by the active material thickness, ϵ_r is the relative permittivity of the active material, and F is the fill factor of biased antenna area over the entire metasurface area ($F = w/\Lambda$ for the metasurface shown in Fig. 2.2. We further write $Q_{abs} = \frac{\omega_0 n}{(g_{tr}-g)c}$, where transparency gain $g_{tr} = -\xi^{-1}\ln R_1$, and is obtained from numerical

simulations such as described in Sec. 2.2. Using the relation $I_- = R_1 G I_+ = c\varepsilon_0 E_-^2 \big/ 2$ and combining Eq. 3.6 and 3.7, we can define a field enhancement factor M as

$$M = \frac{|E_0|^2}{|E_-|^2} = \frac{2(1 - R_1 G)}{R_1 G(g_{tr} - g) n h F}. \tag{3.8}$$

The output intensity is written as $I_{out} = (1 - R_2) T I_-$. With $I_0 = nc\varepsilon_0 E_0^2/4$ and $I_+ = nc\varepsilon_0 E_+^2/4$ we can write the output intensity as:

$$I_{out} = \frac{2(1 - R_2) T}{nM} I_0. \tag{3.9}$$

Substituting Eq. 3.3 and 3.8 to Eq. 3.9, using the laser threshold condition $R_1 G_{th} = (R_2 T^2)^{-1}$, and multiplying by the metasurface area A, we obtain the total output power as

$$P_{out} = N_p \frac{h\nu}{e} \underbrace{\frac{\tau_{eff}}{\tau_2 + \tau_{eff}}}_{\eta_i} \underbrace{\frac{T(1 - R_2)\ln(R_2 T^2)}{(1 - R_2 T^2)\ln(R_1 R_2 T^2)}}_{\eta_{opt}} (I - I_{th}), \tag{3.10}$$

and

$$I_{th} = AF \left[\frac{eL_p}{\sigma \tau_{eff}} \frac{-\ln(R_1 R_2 T^2)}{\xi} + J_{leak} \right]. \tag{3.11}$$

3.2 Effect of modal uniformity

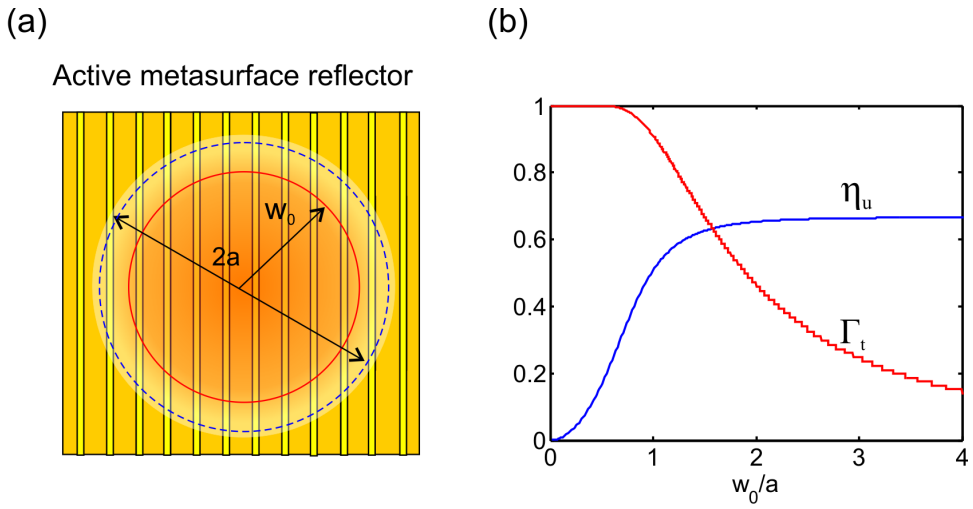

Figure 3.2: (a) Illustration of modal overlap for a Gaussian beam of beam waist w_0 on the metasurface with a circular biased area of $2a$ diameter. (b) Uniformity factor η_u according to Eq. 3.13 and transverse confinement factor Γ_t according to Eq. 3.17 for the modal overlap described in (a).

The derivation so far doesn't account for the effects of modal non-uniformity and spatial hole burning. For example, the effect of modal nonuniformity is to reduce the slope efficiency near threshold, as the injected current is effectively wasted in regions with low modal intensity. The effect of spatial hole burning is particularly acute in THz QCLs, due to the long length scale of the standing wave ($\sim$10 μm) compared to the lateral diffusion lengths of the inverted carrier population (estimated at a few hundred nm). As derived in Ref. [177], this effect results in a nonlinear P-I curve, however near threshold a linearized expression can be derived, and included through an additional "uniformity efficiency" factor $\eta_u \leq 1$ into Eq. 3.10. The slope efficiency near threshold can then be written:

$$\frac{dP}{dI} = N_p \frac{h\nu}{e} \eta_{opt} \eta_i \eta_u. \tag{3.12}$$

Since the electric field is polarized almost entirely in the z-direction within MM waveguides (see Fig. 2.3(b)), the uniformity factor associated with the microcavity mode can be written as

$$\eta_u = \underbrace{\frac{\left(\int_{act} |E_z|^2 \, dA\right)^2}{A_{act} \int_{act} |E_z|^4 \, dA}}_{microcavity} \underbrace{\frac{\left(\int_A |\psi(x,y)|^2 \, dA\right)^2}{A \int_A |\psi(x,y)|^4 \, dA}}_{cavity\ mode\ shape}. \tag{3.13}$$

The first factor describes the modal uniformity within each microcavity, and the second factor describes the uniformity of the slowly varying cavity mode profile incident upon the metasurface. While η_u can be solved exactly from numerical results, for a uniform cavity mode and the sinusoidal dependence of the mode within the microcavity described by Eq. 3.5, $\eta_u = 2/3$ (very close to the value of 0.65 extracted from a finite element simulation for Fig. 2.3(b)). If the transverse beam $\psi(x,y)$ within the cavity is not uniform, then η_u will be further reduced. This function is plotted for a Gaussian beam with spot size w_0 on a square metasurface, where only the center circular area of diameter $2a$ is biased. The uniformity is shown in Fig. 3.2(a) and suggests that under-filling a metasurface with the beam will cause a significant reduction in output power.

The effects of modal uniformity and spatial hole burning illustrate one of the largest differences between the metasurface VECSEL and conventional Fabry-Pérot waveguide QCLs. While longitudinal spatial hole burning in a semiconductor laser also results in a reduced η_u for any given mode, in a Fabry-Pérot laser multi-mode oscillation "washes-out" the overall field nonuniformity and allows for the most efficient use of the available gain. Hence η_u typically does not appear in most conventional expressions for the slope efficiency. However, in

a VECSEL cavity, all of the various longitudinal modes in the external cavity interact with the active material through the same metasurface resonance, and have the same uniformity factor η_u. This may lead to a suppression of multi-mode operation — more work is needed to fully understand this phenomenon. However, we should also point out that this effect may be "engineerable" by designing spectrally and spatially inhomogeneous metasurfaces.

3.3 Relationship to conventional formalism

The formalism developed above for an idealized metasurface QC-VECSEL can be linked to a more common form for semiconductor lasers, if one defines the threshold gain g_{th} in terms of a loss coefficient α_{cav} (prorated over the cavity round trip length $2L$) according to:

$$g_{th} = \frac{n}{\Gamma}\alpha_{cav} = -\frac{n}{\Gamma}\frac{\ln\left(T^2 R_1 R_2\right)}{2L}, \tag{3.14}$$

where $\Gamma = \Gamma_l \Gamma_t$ is a modal confinement factor which describes the overlap of the mode with the QC-active material (satisfying the polarization selection rule). It can be defined using a standard expression,

$$\Gamma = \Gamma_l \Gamma_t = \frac{\int_{act} \varepsilon(\mathbf{R}) \left|E_z(\mathbf{R})\right|^2 dV}{\int_V \varepsilon(\mathbf{R}) \left|E(\mathbf{R})\right|^2 dV}, \tag{3.15}$$

which can be conceptually separated into a longitudinal confinement factor Γ_l and a transverse confinement factor Γ_t as defined in Eq. 3.17. The longitudinal confinement factor Γ_l contains the field enhancement effects of the microcavity resonance M (see Eq. 3.8). For

large cavity lengths, and using the field in Eq. 3.5, we can approximate

$$\Gamma_l \approx \frac{hn^2MF}{2L(1+R_1G_{th})}, \tag{3.16}$$

This expression has undesirable feature that it depends upon the threshold gain G_{th}. However, in the limit of a high finesse cavity, R_1G_{th}, R_2, and T are all close to unity. In this limiting case, Γ_l is directly proportional to the fitted ξ parameter extracted from the numerical metasurface simulation: $\xi = 2L\Gamma_l/n$ (see Eq. 2.1).

The transverse mode confinement factor Γ_t is calculated using

$$\Gamma_t = \frac{\int_{bias\ area} |\psi(x,y)|^2\, dA}{\int_A |\psi(x,y)|^2\, dA}, \tag{3.17}$$

which is plotted in Fig. 3.2 v.s. different mode sizes. Γ_t exhibits a trend opposite to $\eta_{u.}$, suggesting a tradeoff between these two factors in the metasurface bias area design. When the transverse extent of the mode is smaller than the biased area of the metasurface, the transverse confinement factor Γ_t is unity.

Note, if we assume a lossless transmittance for the external cavity, i.e. $T = 1$, the optical coupling efficiency η_{opt} defined in Eq. 3.12 reduces to $\eta_{opt} = \alpha_m/\alpha_{cav}$ where $\alpha_m = -\ln R_2/2L$ is the prorated output mirror loss coefficient and $\alpha_{cav} = -\ln(R_1R_2)/2L$ is the prorated total cavity loss coefficient. The slope efficiency and threshold current density become

$$\frac{dP}{dI} = N_p \frac{h\nu}{e} \frac{\alpha_m}{\alpha_{cav}} \eta_i \eta_u, \tag{3.18}$$

$$J_{th} = \frac{eL_p}{\sigma\tau_{eff}}\frac{n}{\Gamma}\alpha_{cav} + J_{leak}. \tag{3.19}$$

Thus we recover the classic formulas for dP/dI and J_{th} for waveguide based QCLs. The factor of n in these definition results from the fact that the prorated loss coefficients are over a length $2L$ in vacuum, while the gain coefficient is defined in the semiconductor medium with refractive index n.

3.4 Effect of metasurface characteristics: R_1 and ξ

Two parameters describing the metasurface characteristics are involved in the modeling of QC-VECSEL performances: R_1 and ξ, as seen in Eq. 3.10 and Eq. 3.11. Since R_1 can be represented as $R_1 = e^{-\xi g_{tr}}$ based on Eq. 2.1, it is more straightforward to investigate the dependence of laser performances on the transparency gain g_{tr} and ξ. Physically, g_{tr} depends on the excited resonant mode profile in metasurface microcavities; a higher g_{tr} is seen for mode profiles with stronger fringing fields concentrated around the microcavity corners and edges, which increases metallic loss. ξ is a parameter extracted from the linear curve fit of Eq. 2.1 at a specific frequency, which physically reflects the modal confinement within the QC gain medium. In practice a larger ξ suggests a higher radiative Q-factor of the metasurface, and hence ξ is peaked at the resonant frequency (see Fig. 2.3(d)).

To understand how g_{tr} and ξ influence QC-VECSEL performances, the laser output power P_{out} that changes with the output coupler reflectance R_2 is studied for three metasurface designs: (i) the baseline TM_{01} metasurface, (ii) TM_{03} metasurface, and (iii) patch array

metasurface, which are elaborated on in Chapter 2. The resonant frequency for these three designs are 3.4 THz, at which the reflectance changes with bulk gain are plotted in Fig. 3.3. g_{tr} and ξ extracted for these designs are summarized in Table 3.1. Plugging the three groups of g_{tr} and ξ into Eq. 3.10 and Eq. 3.11, we obtain the output power P_{out} change with the output coupler reflectance R_2 as plotted in Fig. 3.4 for two cases of external cavity loss: $T^2 = 0.82$ which follows the estimation in Sec. 4.2 and an ideal external cavity with $T^2 = 1$. A fixed bias area of $AF = 0.3$ mm^2, which is closed to the metasurface demonstrated in Sec. 5.4, and a fixed injection current density of $J = 600$ cm^2 are assumed. The values of other involved parameters including $N_p = 163$, $\sigma\tau_{eff}/eL_p = 0.64$ cm/A, $\nu = 3.4$ THz, $\eta_i = 0.43$, $\eta_u = 0.65$, $J_{leak} = 343$ A/cm^2 are inherited from the experimentally extracted values presented in Sec. 5.4.

As expected, the output power increases as the output coupler reflectance decreases, peaks at a certain reflectance, and then rolls off until the lasing ceases. The optimized R_2 at which the optimum output power P_{opt} is reached varies for different metasurface designs and occurs at lower values for metasurfaces with higher ξ. In other words, a more transmittive output coupler is needed to achieve the optimum output coupling for a metasurface with low radiative Q-factor. Another observation is that in a lossless external cavity with $T^2 = 1$ the optimum output power is higher for metasurfaces with a lower g_{tr}, which is not surprising as lower absorption loss is always preferred. However, in a lossy external cavity with $T^2 < 1$ a higher ξ leads to a higher optimum output power even if it is accompanied with a higher transparency gain. Larger ξ is beneficial in a lossy external cavity because it leads to a larger field enhancement within the QC gain medium, i.e. less field resides in the lossy cavity. This

finding implies that one should maximize the power output from an actual QC-VECSEL in the presence of external cavity loss by optimizing both g_{tr} and ξ.

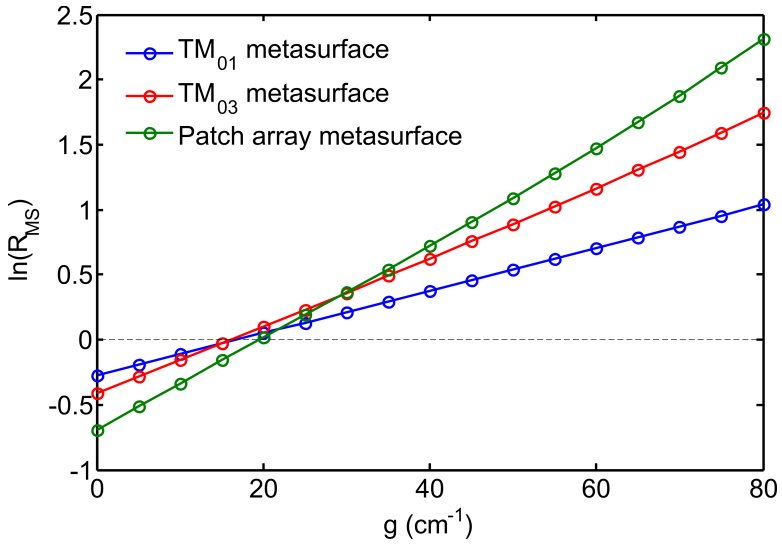

Figure 3.3: Simulated metasurface reflectance R_{MS} change with bulk gain g for three metasurface designs at 3.4 THz. $R_{MS} = 1$ is indicated by the black dashed line.

Table 3.1: Values of g_{tr} and ξ extracted for three metasurface designs at 3.4 THz.

Design	g_{tr} (cm^{-1})	ξ (cm)
TM_{01} metasurface	16.8	0.0163
TM_{03} metasurface	16.6	0.0277
Patch array metasurface	19.6	0.0370

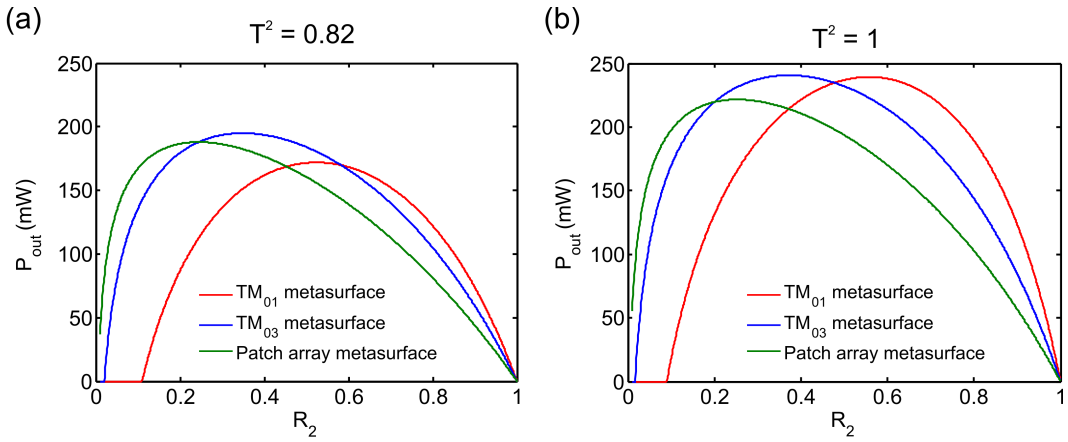

Figure 3.4: Calculated output power change with the output coupler reflectance R_2 for $T^2 = 0.82$ (a) and $T^2 = 1$ (b) for different metasurfaces with a fixed bias area of $A = 0.3$ mm^2.

Since the optimization of g_{tr} and ξ depends on how lossy the external cavity is, to obtain a complete picture it is useful to study four parameters that characterize laser performance as a function of both g_{tr} and ξ, including optimum output power P_{opt}, slope efficiency η_{slp}, threshold current density J_{th}, and optimum output coupler reflectance R_2. As shown in Fig. 3.5, for a lossless cavity P_{opt} improves with a lower g_{tr}, as a result of a lower J_{th} and higher η_{slp}, which, however, shows no dependence on ξ at all. As pointed out, the optimized R_2 is smaller with a higher ξ. In contrast, a very different colormap is obtained for a lossy external cavity with $T^2 = 0.82$ (see Fig. 3.6), which suggests that P_{opt} improves with a lower g_{tr} and a higher ξ, contributed by lower J_{th} and higher η_{slp}. This dependence is still valid even for a slightly lossy external cavity with $T^2 = 0.98$, as seen from Fig. 3.7. 2% round-trip external cavity loss is an lower bound estimate for a low-loss cavity, such as an intra-cryostat compact cavity with cryostat window loss and air loss removed (see Chapter 7).

However, it is worth noticing that the increase of P_{opt} with ξ is less dramatic and tends to saturate at a lower ξ for a less lossy cavity, as seen from Fig. 3.8(a), with an extreme case being that for $T^2 = 1$ where P_{opt} does not vary with ξ. Since P_{opt} converges to its maximum $P_{opt}|_{\xi\to\infty}$ as ξ keeps increasing, we can reasonably define the optimized value of ξ as ξ_{opt} at which 90% of $P_{opt}|_{\xi\to\infty}$ is reached, which are indicated by dots in Fig. 3.8(a) for three cases of T^2. ξ_{opt} is further calculated and plotted against T^2 for different g_{tr} (see Fig. 3.8(b)), which suggests that a higher ξ is preferred for a lossier external cavity with lower T^2. In the actual design process, even if the values of T^2 and g_{tr} are estimated with an accuracy limit, an optimum range of ξ can still be inferred from the results shown in Fig. 3.8(b), which provides a guideline for metasurface design and optimization.

Finally, there is a caveat when designing a metasurface with a high ξ. Since a higher ξ indicates lower radiative loss, a metasurface with a very high ξ might self-lase before lasing in the QC-VECSEL. This is rarely seen in the QC-VECSELs demonstrated so far since the metasurface resonance is characteristic of broad linewidth and thus high radiative loss. However, there exists an exception case of polarimetric metasurface self-lasing discussed in Sec. 8.4, which occurs at a high-Q resonance mode. Besides, the narrower linewidth associated with a higher ξ makes it more challenging to match the metasurface resonance with the QC material bulk gain peak.

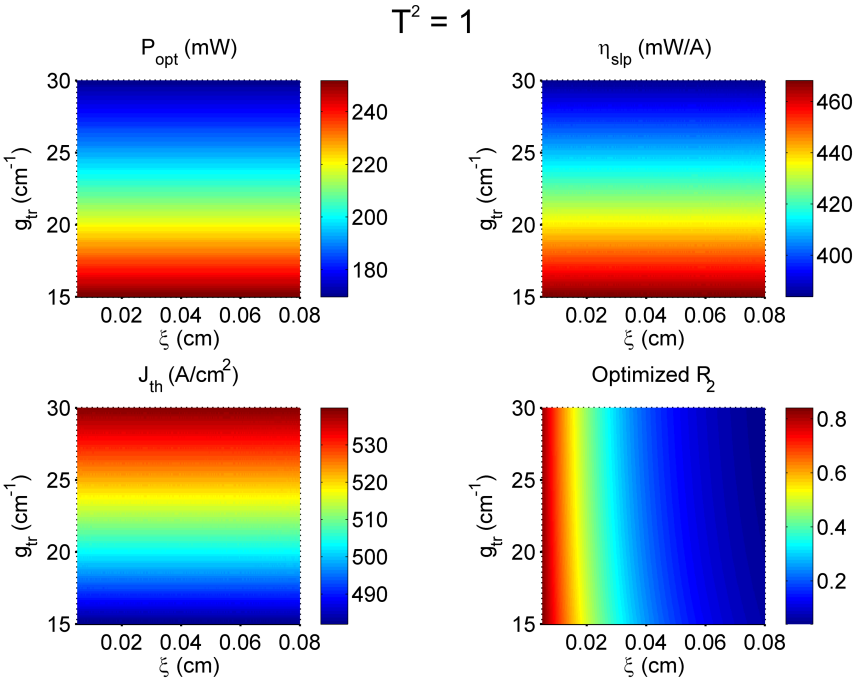

Figure 3.5: Calculated variations of P_{opt}, η_{slp}, J_{th}, and optimized R_2 with g_{tr} and ξ for a lossless external cavity with $T^2 = 1$.

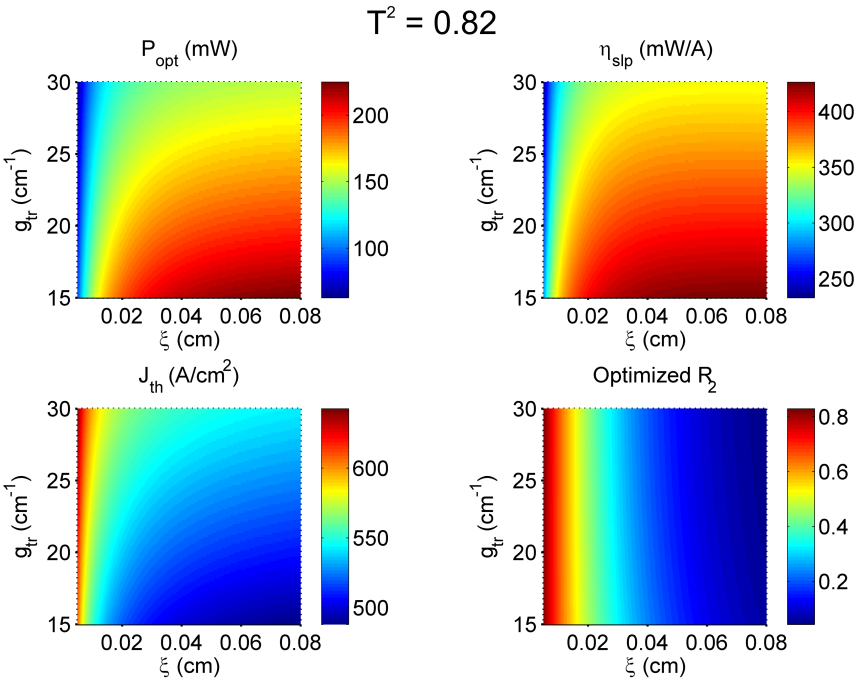

Figure 3.6: Calculated variations of P_{opt}, η_{slp}, J_{th}, and optimized R_2 with g_{tr} and ξ for a lossy external cavity with $T^2 = 0.82$.

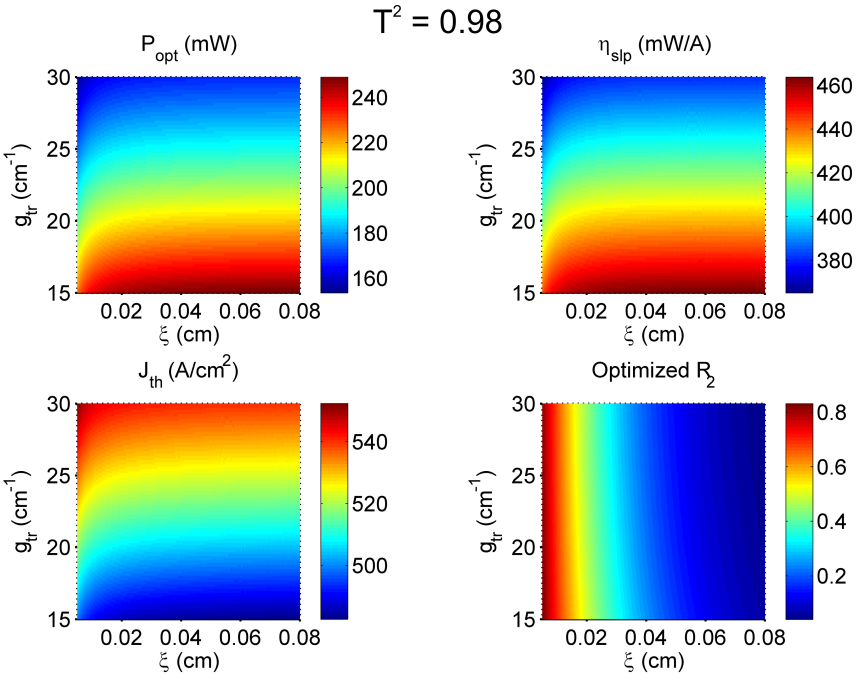

Figure 3.7: Calculated variations of P_{opt}, η_{slp}, J_{th}, and optimized R_2 with g_{tr} and ξ for a slightly lossy external cavity with $T^2 = 0.98$.

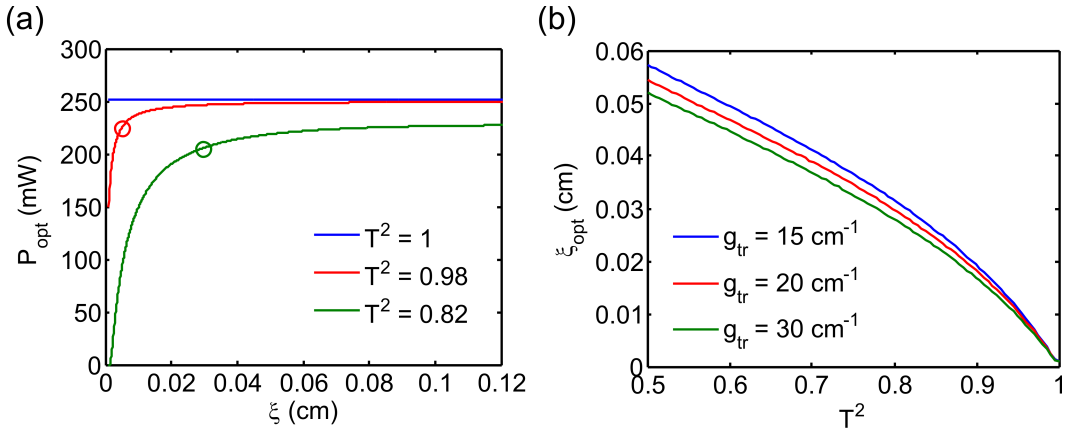

Figure 3.8: (a) P_{opt} change with ξ for different external cavity losses represented by T^2 and a fixed $g_{tr} = 15$ cm^{-1}. The red and green dots indicate where P_{opt} is 90% of $P_{opt}|_{\xi\to\infty}$. (b) ξ_{opt} change with T^2 for three values of g_{tr}. ξ_{opt} is where 90% of $P_{opt}|_{\xi\to\infty}$ is achieved.

CHAPTER 4

VECSEL cavity design and modeling

This chapter focuses on the design and modeling of QC-VECSEL cavities of various types, including plano-concave mirror Gaussian cavity, plano-plano Fabry-Pérot (FP) cavity, and intra-cryostat compact cavity. Different sources of cavity loss are discussed and calculated to estimate the threshold metasurface reflective gain required for lasing. The Fox-and-Li method is used and further modified to model the cavity mode profiles, diffraction loss and threshold gain for QC-VECSELs, which provides insights to compare pros and cons of different cavity designs.

4.1 QC-VECSEL cavity design

QC-VECSELs have been demonstrated in a variety of external cavity types, as summarized in Fig. 4.1. The first proof-of-concept demonstration of QC-VECSELs was made with a gold concave mirror external to the cryostat in conjunction with the active metasurface mounted within to form a hemispherical cavity [178], as shown in Fig. 4.1(a). This cavity has zero output coupling loss due to nearly unity reflection to the cavity, and ideally very low cavity diffaction loss that is insensitive to minor cavity misalignment, since it is a geometrically stable Gaussian cavity as long as the cavity length L_c is chosen to be smaller than the

concave mirror curvature radius. The low external cavity loss is preferred for the initial proof-of-concept trials.

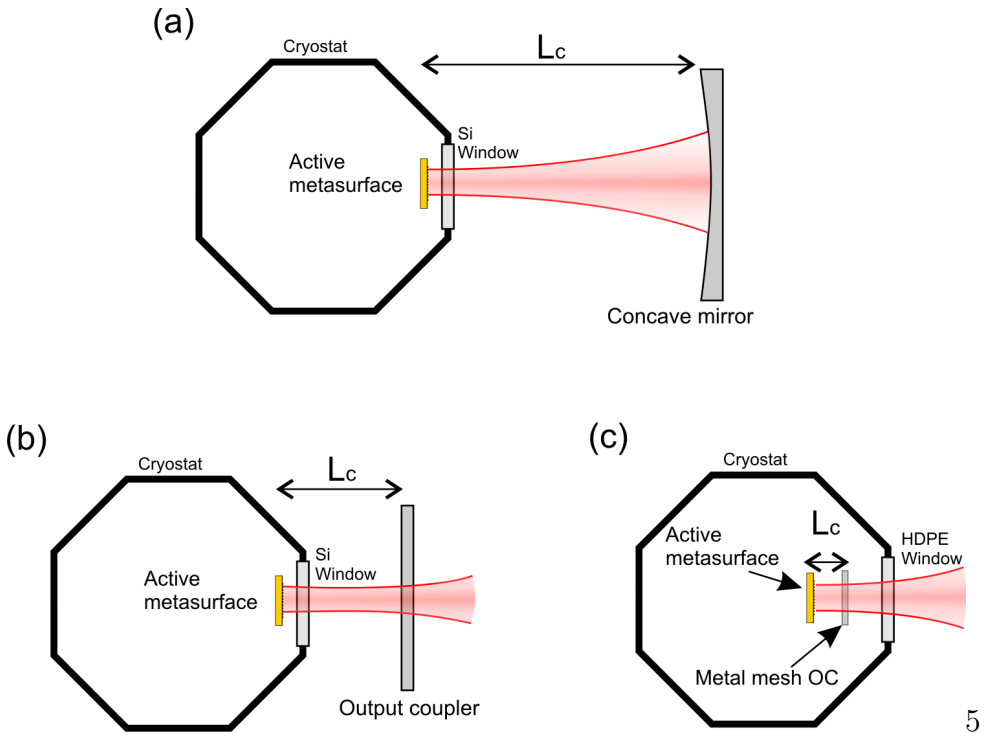

Figure 4.1: Schematics of three QC-VECSEL cavity designs: (a) plano-conave mirror Gaussian cavity; (b) plano-plano Fabry-Pérot cavity; (c) plano-plano compact cavity inside a cryostat.

Given that partially transmitting spherical mirrors are not readily available in THz range and drilling a hole through the concave mirror will mess up the beam, we soon turned to using flat output couplers (OC) to build plano-plano Fabry-Pérot (FP) cavities by as shown in Fig. 4.1(b). It is possible to use an off-the-shelf wire grid polarizer as an output coupler [174]. A particular advantage of this approach is that the output coupling efficiency is tunable with the polarizer's orientation, enabled by the polarized response from both the metasurface and the polarizer. This allows optimization of the power "on-the-fly" simply by turning the output coupler to reach the optimum coupling point. However, the polarization

eigenstate for the circulating cavity mode is non-trivial, and a function of orientation, which complicates analysis. Meanwhile, we designed and fabricated a number of THz OCs based upon either inductive or capacitive metal meshes of different mesh sizes on a crystal quartz substrate to provide different amounts of reflectance [179, 180]. Due to the FP effect of the substrate, the transmittance/reflectance of these OCs changes with frequency in a oscillating manner, which we measured exactly using a FTIR spectrometer (see Sec. 5.4). Unlike using a polarizer as OC, these metal mesh OCs are insensitive to polarization. In the recently demonstrated focusing metasurface QC-VECSEL [181], we used these metal mesh OCs to form a cavity, instead of a wire-grid polarizer, to prevent the polarized response from the OC from interfering with the focusing effect. Compared with the previous plano-plano FP cavity, the QC-VECSEL based on a focusing metasurface exhibits a higher stability, resembling a concave-plano hemispherical cavity. This is confirmed by the numerical modeling of cavity loss change with the misaligned angle between OC/concave mirror and metasurface, based on a modified Fox-and-Li method explained in Sec. 4.3.

The third type of QC-VECSEL cavity that we have demonstrated is a compact intra-cryostat cavity, as shown in Fig. 4.1(c). The parallelism between the OC and metasurface is achieved by fine tuning a specially designed mechanical stage at RT, which is then mounted inside the cryostat and cooled down. While this approach prevents fine alignment of the cavity during operation, our experience so far suggests that misalignment due to thermal contraction at low temperature is not a severe problem for high performance metasurfaces. This is partly attributed to the short cavity length allowed by this intra-cryostat setup, which reduces the diffraction loss due to misalignment. Using a focusing metasurface is also

helpful, though not essential, to mitigate the effects of misalignment. This compact cavity is not only convenient for application, but also eliminates any possible loss from the cryostat window and atmosphere. The lasing threshold for this cavity has been found to be much lower than the external FP cavity counterpart with the same OC and metasurface (see Sec. 7.2).

4.2 Sources of cavity loss

In a cold QC-VECSEL cavity (i.e. QC material gain $g = 0$ cm^{-1}), the total cavity loss consists of (i) metasurface absorption characterized by passive metasurface reflectance R_1 or the transparency gain g_{tr}, (ii) output-coupling loss determined by OC's reflectance R_2, and (iii) external cavity loss represented by the round-trip transmittance $T^2 = (1-\alpha_a)(1-\alpha_w)(1-\alpha_d) \approx 1-\alpha_a-\alpha_w-\alpha_d$, where α_a, α_w, and α_d respectively represent the round-trip power loss owing to atmospheric absorption, the absorption and reflection loss due to the cryostat window, and the QC-VECSEL cavity diffraction loss due to cavity misalignment and metasurface finite size.

THz radiation is subject to strong atmospheric absorption except within a few transmission windows where 0.5–2 dB/m attenuation is typical, as shown in Fig. 4.2(a). Fig. 4.2(b) shows the round-trip air absorption loss α_a as a function of one-trip propagation length in air within a QC-VECSEL cavity. For a typical external setup of $\sim$2 mm air length, α_a is about 0.5–2% depending on the relative humidity level and frequency.

In the actual QC-VECSEL setup, the metasurface is mounted inside a cryostat facing the

cryostat window, which is a 3.3 mm-thick high-resistivity silicon. The cryostat window acts as an etalon filter inside the cavity, the transmission spectrum of which changes rapidly with frequency ω and is calculated by $T_{Si} = |\frac{4ne^{i\delta/2}}{(n+1)^2-(n^2-1)e^{i\delta}}|^2$, where $\delta = \frac{2n\omega}{c}d$, d is the thickness of Si window, $n = 3.417 + i\frac{\alpha c}{2\omega}$, $\alpha = 0.05$ cm^{-1}, and c is the speed of light. As shown in Fig. 4.2(c), the Si window's etalon effect determines that lasing is likely only allowed at discrete frequencies separated by a free spectral range (FSR) of ~13 GHz, where the round-trip loss of $1 - T_{Si}^4$ is minimal and reads $\alpha_w \sim 7\%$.

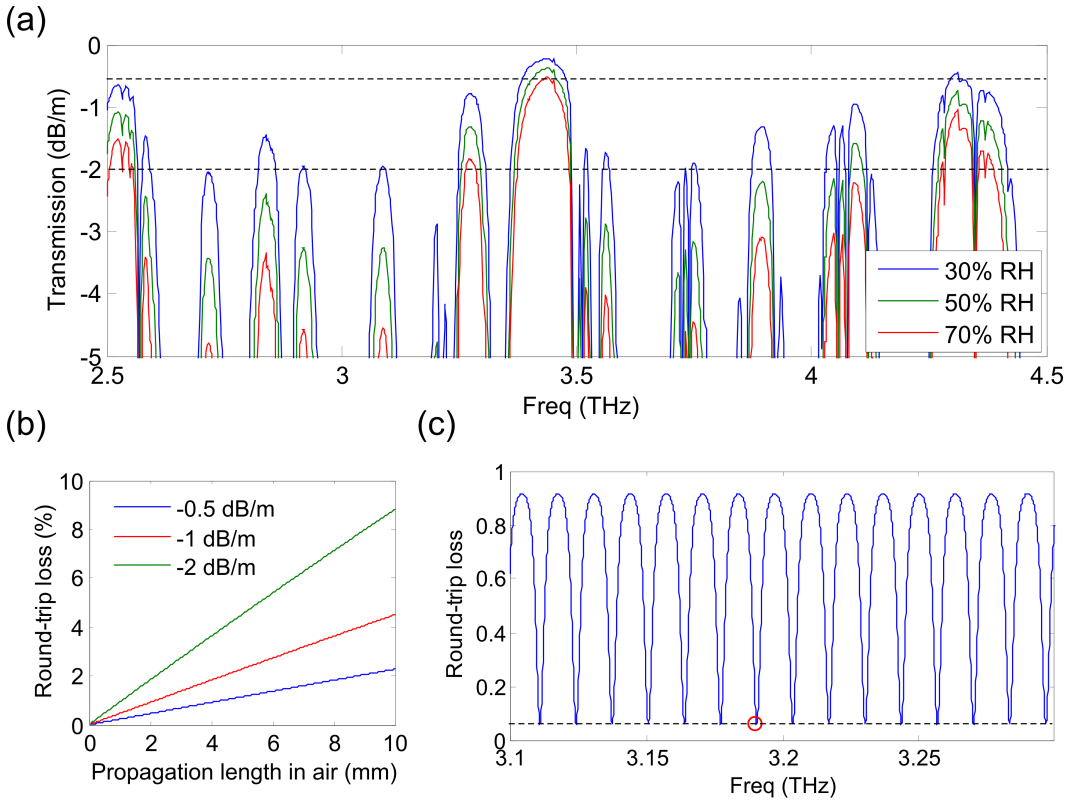

Figure 4.2: Schematics of three QC-VECSEL cavity designs: (a) Atmospheric transmission spectrum of THz radiation represented by the attenuation in dB/m for three relative humidity (RH) levels. Dashed lines indicates the 0.5–2 dB/m attenuation range. (b) Round-trip atmospheric absorption loss α_a change with propagation length in air. (c) Round-trip loss spectrum of a 3.3 mm-thick high-resistivity silicon window as an etalon filter. The red dot highlights the minimal loss of ~7%.

The diffraction loss α_d is calculated using the Fox-and-Li method explained below. $\alpha_d =$

10–15% is a reasonable estimate for an external cavity setup. To sum up, we can estimate the threshold bulk gain for lasing g_{th} by $g_{th} = g_{tr} - \frac{\ln(R_2 T^2)}{\xi}$ rewritten from Eq. 2.1, using a reasonable estimate of total external cavity loss of $T^2 = 1 - 1\%(\alpha_a) - 7\%(\alpha_w) - 10\%(\alpha_d) = 0.82$. Assuming $R_2 = 0.95$ and incorporating the simulated results for the baseline metasurface design of $g_{tr} = 16.8$ cm^{-1} and $\xi = 1.63 \times 10^{-4}$ m, we obtain $g_{th} = 31.4$ cm^{-1}. This level of bulk gain is readily achievable by QC materials. Improved cavity and metasurface designs can further reduce the threshold gain, such as using an intra-cryostat cavity design free from air and window loss (see Fig. 4.1(c)).

4.3 Modeling of cavity mode by Fox-and-Li method

The cavity mode and corresponding diffraction loss out of the QC-VECSEL cavity are calculated by a scalar 1D numerical model based on the Fox-and-Li method (polarization is neglected) [182, 183]. In this method an initial distribution of electric field is launched from the metasurface and propagated to the OC using Huygen's integral [184]; upon each reflection, the field profile is multiplied by a spatially dependent complex reflection coefficient on the finite-size metasurface and OC. The algorithm is iterated until the mode profile and round-trip cavity loss converge to a stable solution after multiple round trips. We represent the 1D reflection coefficient distributions on the metasurface reflector and the OC by $r_{MS}(x_a)$ and $r_o(x_b)$. The back and forth wave propagation in the cavity is formulated by

$$B_n(x_b) = \sqrt{\frac{k_0}{i8\pi}} \int_{-a}^{a} A_n(x_a) r_{MS}(x_a) \frac{e^{ikR}}{\sqrt{R}} (1 + cos\theta) dx_a \tag{4.1}$$

$$A_{n+1}(x_a) = \sqrt{\frac{k_0}{i8\pi}} \int_{-b}^{b} B_n(x_b) r_o(x_b) \frac{e^{ikR}}{\sqrt{R}} (1 + cos\theta) dx_b, \tag{4.2}$$

where the 1D integral in Eq. 4.1 is evaluated over the metasurface of dimension $2a$ on which $A_n(x_a)$ represents the electric field distribution after n round trips, and integral in Eq. 4.2 is evaluated over the OC of dimension $2b$ of on which the field is represented by $B_n(x_b)$. R is the distance from the point x_a to x_b. θ is the angle between the direction x_a to x_b and the direction normal to the metasurface plane. k_0 is the free space wave vector. After many round trips, the field distributions stabilize to the lowest-loss mode profile and the attenuation factor defined as $\gamma_n(x'_a) = \frac{A_n(x'_a)}{A_{n-1}(x'_a)}$ also converges to a constant. The round-trip cavity diffraction loss can be extracted by $\alpha_d = 1 - |\gamma_n(x'_a)|^2$ (x'_a is a fixed position on the metasurface that can be arbitrarily chosen).

The 1D Fox-and-Li approach is first applied to the plano-plano FP cavity to calculate its diffraction loss and mode profile, which is essentially an unstable cavity. However, as long as the cavity length is small enough with respect to the size of flat elements, a near-Gaussian mode survives in it as the lowest-loss mode. The cavity length L_c is chosen based on the condition for the Fresnel number $N = \frac{(L/2)^2}{L_c \lambda_0} > 0.5$ [182], where the metasurface is assumed of $L \times L$ size and λ_0 is the free-space wavelength. Due to fabrication and material constraints, the size of metasurface is generally limited to less than 3×3 mm^2 while the size of OC can be made much larger. Therefore the diffraction loss is mainly induced by the mode spillover of non-vanishing tails on the metasurface edges. As expected, the calculated round-trip diffraction loss α_d increases as the cavity length L_c increases and the metasurface size of $L \times L$ decreases (see Fig. 4.3(a)). The converged mode profiles on the metasurface

for $L_c = 9$ mm are shown in Fig. 4.3(c), where the intensity of mode edges is higher for a smaller metasurface, resulting in a worse mode spillover. From the converged mode profile on the OC, it is straightforward to calculate the far-field beam pattern, which is well fitted with a Gaussian curve. The full width at half maximum (FWHM) divergence angle θ_{FWHM} can be extracted from the Gaussian curve fit, which is shown in Fig. 4.3(b) for different metasurface sizes with varying cavity length L_c. It is seen that the cavity with a larger metasurface generates a narrower far-field beam, which slightly narrows down with long cavity length. The far-field beam intensities with Gaussian curve fits are plotted in Fig. 4.3(d) for $L_c = 9$ mm. It is noticeable that the larger diffraction occurring on a small metasurface with $L = 1.5$ mm for $L_c = 9$ mm cavity length also induces slightly larger side lopes in the far-field beam.

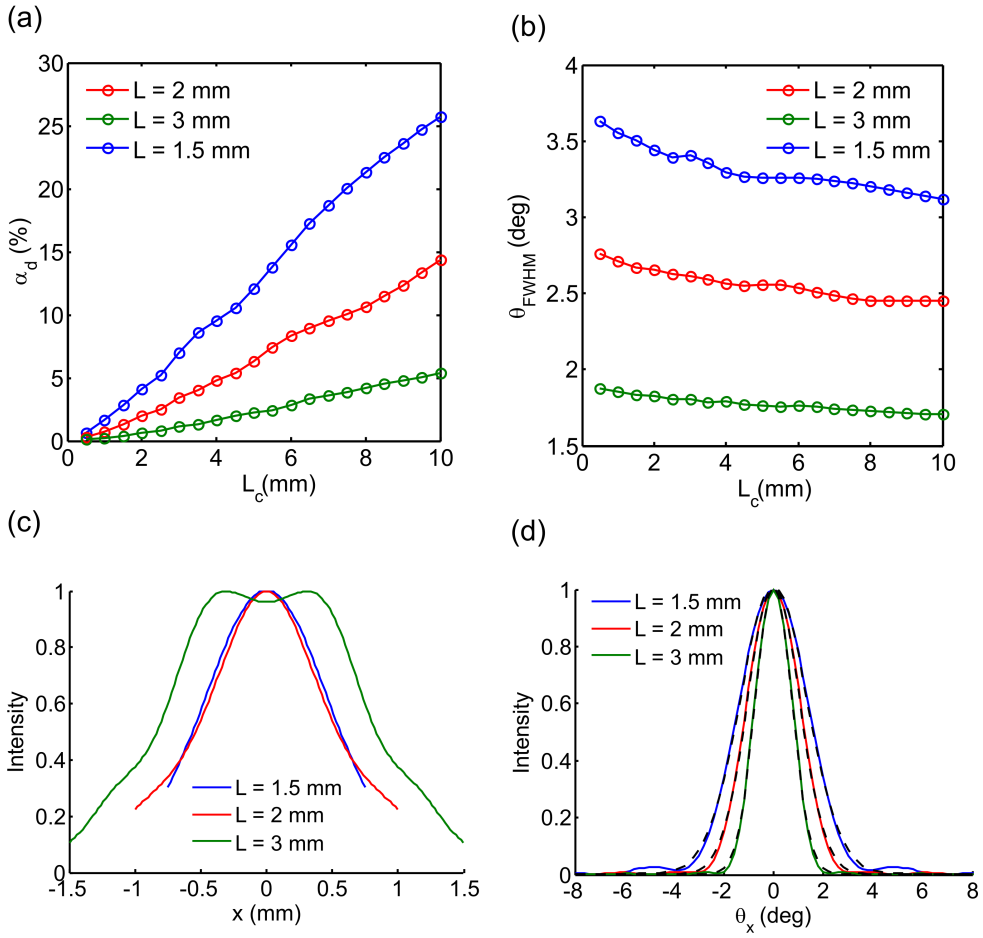

Figure 4.3: Round-trip diffraction loss α_d (a) and FWHM divergence angle of far-field beams θ_{FWHM} (b) as a function of cavity length L_c for a plano-plano FP cavity formed by a metasurface of size $L \times L$ and a much larger OC. Converged mode profiles and far-field beams are plotted in (c) and (d) for metasurfaces of size $L \times L$ for cavity length $L_c = 9$ mm.

A geometrically stable cavity that supports the fundamental TEM_{00} Gaussian mode is ideal for VECSEL cavity. However, this type of cavity is only utilized for the initial proof-of-concept demonstration of QC-VECSEL formed by a metasurface and a concave mirror (see Sec. 5.2), until a later demonstration of using the active focusing metasurface (FCMS) design that mimics a concave mirror to form a stable cavity with a flat OC element (see Chapter 6). A stable cavity, such as concave-plano hemispherical cavity in this case, leads to reduced diffraction loss, especially when there is an angular misaligned δ between

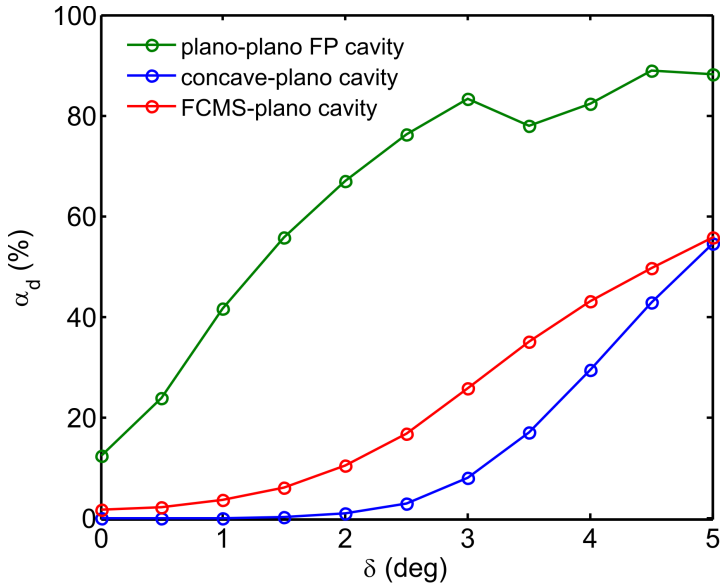

Figure 4.4: Calculated round-trip cavity loss α_d induced by angular misalignment vs. misaligned angle δ for three types of cavity: plano-plano FP cavity, concave-plano cavity, and FCMS-plano cavity. All the other sources of loss are neglected.

OC/concave mirror and metasurface that induces additional beam walk-off loss. This is confirmed by 1D Fox-and-Li calculation for three types of cavities with varying misaligned angle δ introduced: plano-plano FP cavity, concave mirror-plano cavity, and FCMS-plano cavity. The metasurface size of $L = 2$ mm is kept identical. The reflectivity of concave mirror with a curvature radius of R_m is represented by $e^{-i(\frac{x_a^2}{R_m})}$, which is valid as long as $\frac{L^2/4}{2R_m} \ll \sqrt{L_c\lambda_0}$ [183]. The reflectivity distribution on the FCMS is represented by a nonuniform phase profile modulated by the ridge with distribution and a "fictitious" uniform reflectance, which is detailed in Chapter 7. The small angular misalignment is represented by a linear phase shift of $e^{-i\frac{4\pi\delta x_a}{\lambda_0}}$, which varies spatially with x_a. Fig. 4.4 plots the calculated round-trip diffraction loss α_d as a function of the misaligned angle δ for the three cavities, which confirms that stable cavities lead to the much reduced diffraction loss and improved robustness to angular misalignment.

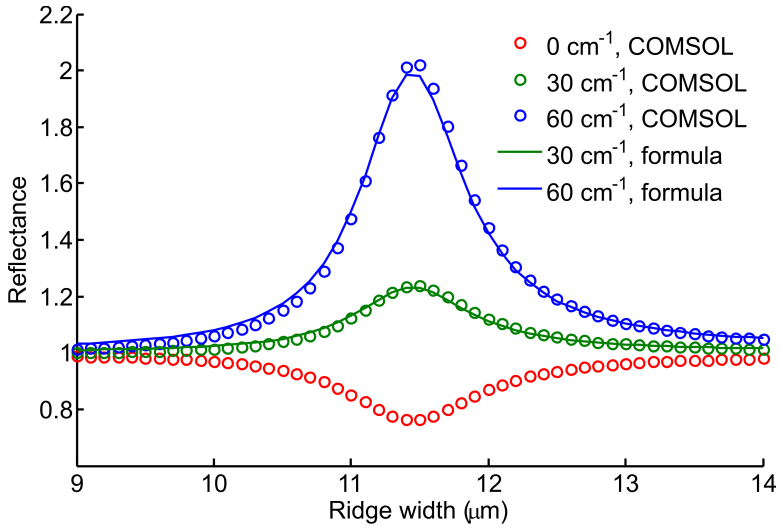

Figure 4.5: Simulated results of reflectance v.s. ridge width for a metasurface with periodicity $\Lambda = 70$ μm by COMSOL in comparison to the results obtained by Eq. 4.3 for nonzero bulk gain of 30 cm^{-1} and 60 cm^{-1}.

4.4 Calculation of threshold gain by modified Fox-and-Li method

The above Fox-and-Li calculation is aimed at estimating the diffraction loss α_d only, which does not involve all the other losses. In an attempt to explicitly calculate the threshold gain g_{tr} for lasing, a modified Fox-and-Li calculation is implemented using a root finder algorithm to find the value of bulk gain that leads to a metasurface reflectivity distribution for which the total round-trip cavity loss is zero. This calculation is useful to evaluate the various metasurface designs, particularly for the inhomogeneous design that has a nonuniform reflectivity distribution (such as FCMS) and the metasurfaces that are selectively biased.

In this root finder, the metasurface reflectance R_a is now a function of position x_a and bulk gain g. The reflectivity phase is nearly unchanged with bulk gain, as is confirmed by the finite-element simulation. Using Eq. 2.1, we can write R_a as

$$R_a(x_a, g) = e^{-\frac{R_1(x_a)}{g_{tr}}(g-g_{tr})} \tag{4.3}$$

where $R_1(x_a)$ is the reflectance distribution on the metasurface when it is passive. g_{tr} is assumed unchanged with x_a (i.e. over the metasurface) at a certain frequency, which is obviously valid for a uniform metasurface design. What about an inhomogeneous metasurface where the ridge width is varying along x_a? To account for this case, the reflectance v.s. ridge width is plotted using Eq. 4.3 with $g_{tr} = 17$ cm^{-1}, which is extracted for the ridge width of 11.5 μm corresponding to the resonance peak at 3.4 THz. As shown in Fig. 4.5, the close resemblance of the results by Eq. 4.3 to the COMSOL simulation results confirms the validity of using Eq. 4.3 to approximate the nonuniform metasurface reflectance change with bulk gain. A root finder algorithm is developed by incorporating Eq. 4.3 into Eq. 4.1 and 4.2 and gradually increasing g while performing the back and forth propagation until the attenuation factor $\gamma_n(x'_a) = \frac{A_n(x'_a)}{A_{n-1}(x'_a)}$ is converged to unity, which signals g_{th} is found. Using this method, g_{th} are calculated for three cavity setups as a function of angular misalignment, which are detailed in Chapter 7.

CHAPTER 5

External cavity QC-VECSELs with uniform metasurface

This chapter presents a wealth of experimental results regarding external cavity QC-VECSELs based on uniform metasurface designs. The uniform metasurface composed of a periodic array of sparsely spaced and identical metal-metal (MM) waveguide microcavities has a uniform distribution of reflection amplitude and phase over the metasurface area. It can form a Gaussian cavity with a concave gold mirror and a plano-plano FP cavity with a flat output coupler (OC), which have been both demonstrated experimentally. Considerable power has been achieved in combination with a near-Gaussian beam pattern from uniform metasurface QC-VECSELs based on plano-plano FP cavity, proving the success of QC-VECSEL concept. Furthermore, the output coupling efficiency is easily controllable by the choice of OCs or simply turning the polarizer as OC, which largely eases the power maximization by achieving the optimum output coupling efficiency. A family of uniform metasurface designs targeted at different resonant frequencies have been demonstrated lasing, which covers a broad spectral range from 2.5–4.4 THz.

5.1 Uniform metasurface design

The first uniform metasurface consists of 17 MM ridges spaced with a periodicity of $\Lambda = 90$ μm, with a center square area of 1.5×1.5 mm^2 biased. The ridge width w is designed varying from 11.5 μm to 13.5 μm to let the metasurface resonant frequency overlap with the QC material bulk gain peak at ~2.9 THz (FL178-M7 design). The fabricated metasurface is shown in Fig. 5.1(a), where the unbiased reflectors on each side of the active area ensures the tails of cavity mode see a highly reflecting area. The full-wave finite-element simulation of this metasurface reflectance is shown in Fig. 5.1(b), which confirms its amplification effect near the TM_{01} resonant frequency when the bulk gain g is above ~20 cm^{-1}.

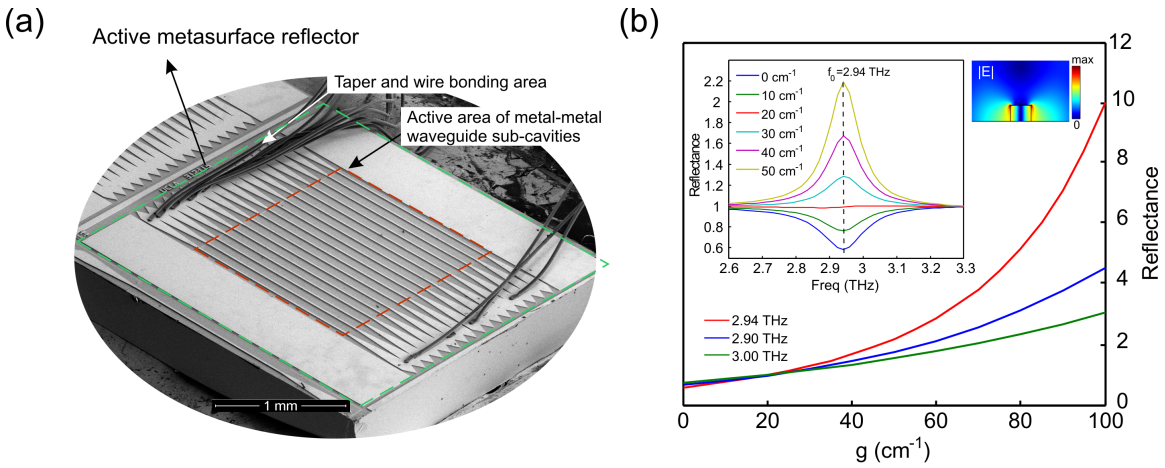

Figure 5.1: (a) SEM image of a fabricated active metasurface with a 1.5×1.5 mm^2 active area within the red dashed box. (b) Simulated reflectance change with the bulk gain g at three different frequencies for an active metasurface with $w = 13$ μm and $\Lambda = 90$ μm. The left inset shows the simulated reflectance spectra for normally incident planes waves for different values of g. The right inset shows the E-field magnitud.1e at resonance of 2.94 THz, where the E-field is predominantly polarized normal to the metal plane within the gain medium.

5.2 Proof-of-concept demonstration of QC-VECSEL

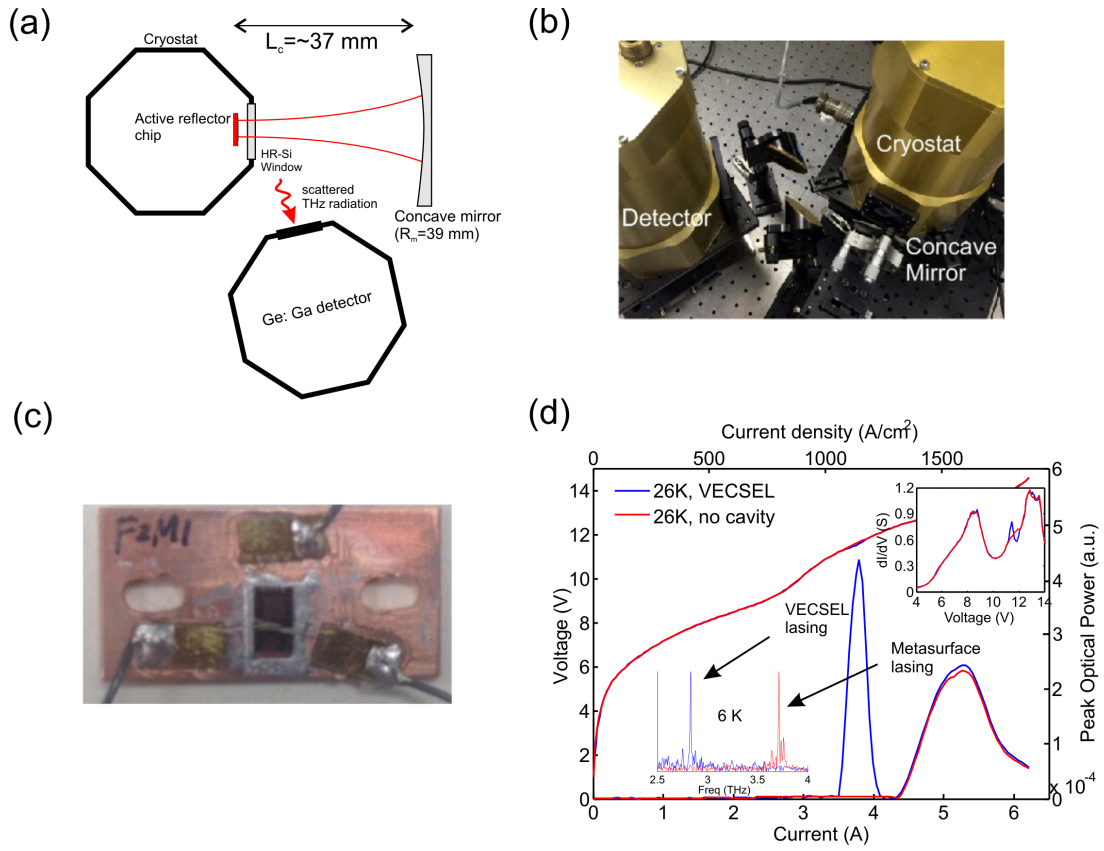

Figure 5.2: (a) Schematic of the proof-of-concept demonstration of THz QC-VECSEL in a plano-concave FP cavity. (b) Actual experimental setup. (c) Active metasurface device mounted on a copper chip carrier. (d) *P-I-V*s of the QC-VECSEL and the metasurface alone (with no cavity). The inserted are spectra for VECSEL lasing and metasurface lasing, and the differential conductance curves for two configurations.

We obtained lasing in a THz QC-VECSEL device for the first time in April 17, 2015. It is a proof-of-concept demonstration realized in a concave-plano Gaussian cavity, which can minimize the diffraction loss and remove the output coupling loss [178]. As shown in Fig. 5.2(a), the cavity consists of an active metasurface (w = 13 μm and Λ = 90 μm) and a concave gold mirror facing the metasurface, the actual experimental setup of which is shown in Fig. 5.2(b). The metasurface device is cleaved from a fabricated piece containing multiple

devices, indium soldered onto a copper chip carrier, and wired bonded to the gold pads, the final form of which is shown in Fig. 5.2(c). The copper chip is mounted on the cold stage inside the cryostat (Infra-Red Laboratories emission dewar) facing the cryostat window.

The cavity is pre-aligned using a He-Ne laser with the opaque cryostat window removed; then the window is re-installed and the cryostat is pumped and cooled down. The power-current-voltage (P-I-V) curve is measured in pulsed mode (0.3% overall duty cycle, 300 ns-long pulses repeated at 10 KHz) at 26 K. Due to no appropriate output coupling channel for direct power measurement, the THz power is measured from a very small scattered component collected by parabolic mirrors and focused to a liquid Helium-cooled Ge:Ga photodetector in lock-in detection mode. The measured P-I curve for the QC-VECSEL exhibits two peaks, as shown in Fig. 5.2(d). In contrast, another P-I-V curve is measured with a blocking object inserted inside the cavity to destroy the VECSEL cavity mode, which only shows one peak that matches with the second peak in the QC-VECSEL P-I curve. Accompanied with P-I curves change is the change in differential conductance curves. These facts suggest that the first peak depends on the presence of the concave mirror and comes from the VECSEL lasing, while the second is indifferent to the cavity setup, which is believed to represent the lasing in the fundamental propagating mode of waveguide sub-cavities. The self-lasing only occurs at low temperature and high biases when the bulk gain is sufficiently high, since it is intentionally suppressed by lossy boundary conditions. The measured spectra for the two bias regions are also very different, with the first closed to the designed meta-surface resonant frequency and the second shifted to a much higher frequency as a result of the Stark effect at the high bias. This proof-of-concept QC-VECSEL demonstration proves

it is viable to implement the VECSEL concept for THz QCLs using the active metasurface reflector.

5.3 Uniform metasurface paired with a polarizer

Beyond the proof-of-concept demonstration, a QC-VECSEL with appropriate output coupling element is the next step. Due to a lack of concave mirrors with partial transmittance in THz range, the focus is quickly shifted to plano-plano FP cavity formed by a uniform metasurface and a flat output coupler (OC) in parallel. The first demonstration uses a free-standing wire-grid THz polarizer (made of 20-μm diameter Tungsten wires spaced with a period of 50 μm) as the OC, as Fig. 5.4(a) shows [174]. Among metasurfaces fabricated with periodicity $\Lambda = 90$ μm and ridge width w varying from 11.5 μm to 13.5 μm, only $w = 12.5$ μm and 13 μm were observed lasing with the best performance obtained from $w = 12.5$ μm. This is primarily attributed to the coupling between microcavity TM_{01} resonant mode and surface wave excited via first-order Bragg scattering, which is detailed in Sec. 2.3. Presumably $w = 12.5$ μm design has the best overlap of the gain spectrum with the metasurface resonance.

5.3.1 Experimental results

The reflectance from a wire-grid polarizer highly depends on the electric field polarization direction relative to the wires, which is maximum ($\sim$0.97) when parallel and minimum ($\sim$0.18) when perpendicular. Due to the polarized response of both the metasurface and polarizer, one can increase the output coupling transmittance by varying the angle θ_p of

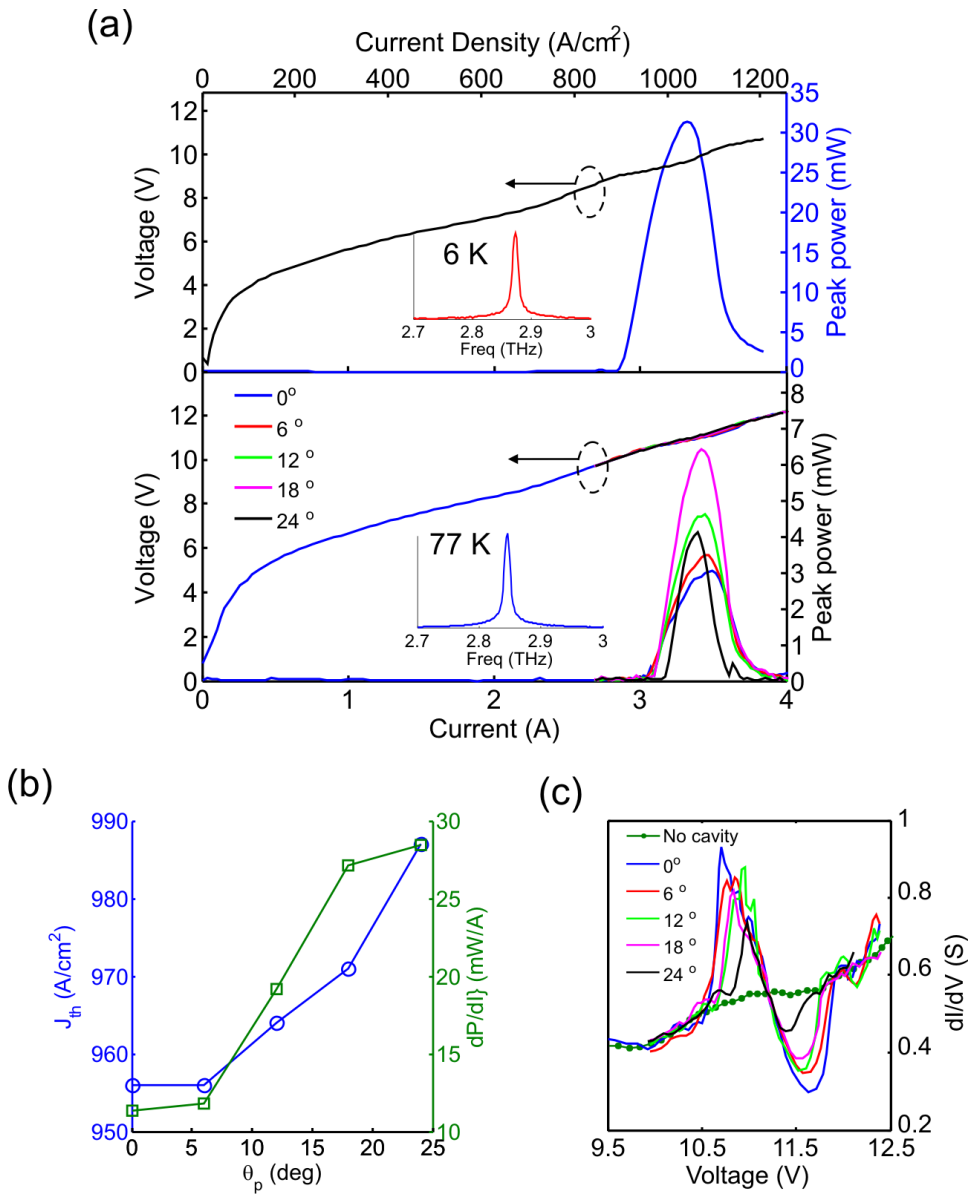

Figure 5.3: (a) Upper: pulsed mode P-I-V characteristic and spectrum at 6K, with polarizer angle $\theta_p = 30°$. Lower: pulsed mode P-I-V characteristics for angle θ_p varied from 0° to 24° at 77 K. The inset is the lasing spectrum. (b) Measured threshold current density J_th and slope efficiency dP/dI versus with θ_p at 77 K. (c) Differential conductance curves in the lasing range for different θ_p and no cavity case at 77 K.

the polarizer from 0° to 90°. θ_p is the angle between the polarizers wire orientation and the direction transverse to the ridges on the metasurface, as indicated in Fig. 5.4(a). The precise dependence is non-trivial, as the output transmittance depends on the polarization state of the circulating laser field, which in turn depends on the co- and cross-polarized reflection coefficients of both the polarizer and metasurface. As for any laser, there is an optimum coupling condition which maximizes the output power, which depends upon the interplay between the coupling loss and total loss, and its effect on threshold, the circulating power, and transmitted power. Fig. 5.3(a) shows *P-I-V* curves for a set of orientation angles from 0° to 24° at 77 K. The *P-I-V* characteristics were measured in pulsed mode (0.25% overall duty cycle, 500 ns-long pulses repeated at 10 kHz, modulated by a slow 5 Hz pulse train with lock-in detection). A calibrated pyroelectric photodetector was mounted close to the output coupler polarizer without any intermediate optics for power measurement. The absolute power calibration procedures are detailed in Appendix D. At 77 K, the output power is maximized at a value of 6.45 mW, which is achieved with $\theta_p = 18°$. The threshold current density and slope efficiency both increase with θ_p as shown in Fig. 5.3(b), which is consistent with an increasing out-coupling loss. For $\theta_p > 24°$, out-coupling loss becomes too high for the VECSEL to reach the lasing threshold. Fig. 5.3(c) shows the differential conductance (dI/dV) for each angle. The discontinuity at threshold is observed to be lower as θ_p is increased, which is consistent with a longer upper state lifetime due to reduced stimulated emission and reduced circulating intensity under higher out-coupling loss conditions. When the polarizer is removed to destroy the external cavity, no lasing power is measured and the discontinuity disappears. Only in one outlier device at liquid Helium temperature was lasing observed to occur without the polarizer; this occurred at very high threshold and at

a frequency (∼3.6 THz) far away from the metasurface resonance of 2.8-2.9 THz (see Fig. 5.2(d)). Due to the larger gain present at 6 K, the optimum coupling condition is reached at a larger polarizer angle of $\theta_p = 30°$. The maximum output power is measured to be 31.3 mW, with a slope efficiency of 80.4 mW/A (equivalent to 0.039 photons/electron/stage), as shown in Fig. 5.3(a). The present metasurface dissipates more than 30 W, which is not suitable for cw operation at cryogenic temperatures. However, because the narrow active region ridges (∼13 μm) is favorable for heat removal, it is believed that the VECSEL configuration is advantageous for cw operation provided the total power consumption is reduced to a moderate level, perhaps by using a different active region design with lower threshold current density or by reducing the total active area of the metasurface.

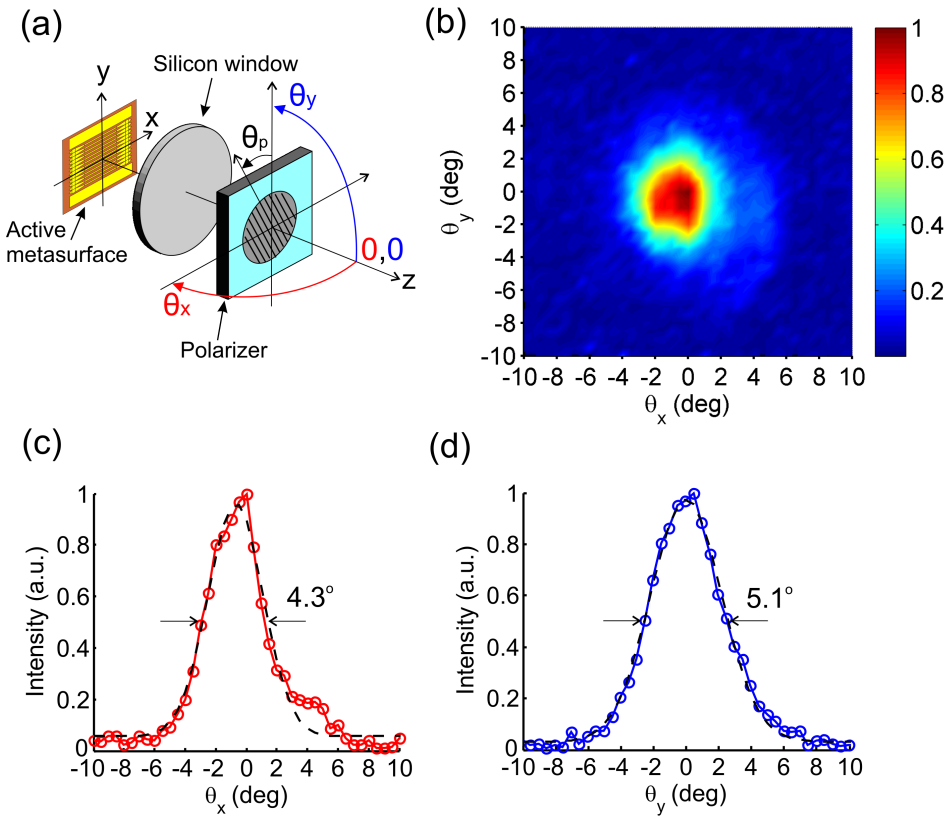

Figure 5.4: (a) The schematic for the VECSEL cavity setup and beam pattern measurement scheme. (b) Measured beam pattern measured for the THz QC-VECSEL at 77 K. (c) and (d) 1D cut of the beam pattern through the intensity maximum along θ_x and θ_y angular directions, with Gaussian curve fit (dashed black line).

At 77 K the emission spectrum is single-mode at 2.846 THz (within the ∼7 GHz resolution limit of our spectrometer), and is unchanged with adjustments in electrical bias, cavity length, or polarizer angle. Tuning the cavity length by moving the polarizer in the axial direction only results in turn-on and -off of lasing, caused by the longitudinal mode phase matching. It is believed that this single mode behavior results from the etalon effect of the HR-Si window in combination with the limited resonant frequency range of the metasurface. The spectrum is also measured at 6 K in pulsed mode and shows single-mode lasing at 2.873 THz. The shift of 27 GHz of the lasing frequency from 6 K to 77 K represents two longitudinal

mode hops in the FP cavity, i.e., approximately twice the ∼14 GHz FSR of the HR-Si window etalon. This mode hopping is presumably a result of the metasurfaces reflection peak and phase change and the active mediums gain profile change with temperature.

The measured far-field beam pattern is quite symmetric and directive as shown in Fig. 5.4(b), which is directly measured after the polarizer as shown in Fig. 5.4(a). The 1D cuts of the beam pattern through the center along θ_x and θ_y directions are given in Fig. 5.4(c) and (d), which show good fits with Gaussian curves. The FWHM divergence angle is about 4.3° in the θ_x direction and 5.1° in the θ_y direction. The low-divergence near-Gaussian beam pattern aligns with the fact that the plano-plano FP cavity can support a quasi-stable cavity mode with a near-Gaussian mode profile, and is close to the calculated beam divergence based on Fox-and-Li method.

5.3.2 Results analysis and discussion

In this implementation of a metasurface QC-VECSEL, the sub-cavity ridge antennas that comprise the metasurface only provide gain to one polarization of incident radiation (considered to be the y-polarization here). This polarized response allows the use of a wire-grid polarizer as an OC mirror with variable transmittance. However, this introduces additional complications, as the cavity mode becomes a function of polarizer angle as well as the reflectance matrices for both the metasurface and the polarizer.

The Jones matrix describing the active reflection from metasurface is given by

$$\mathbf{\Gamma}_1 = \begin{pmatrix} \Gamma_{xx} & 0 \\ 0 & \Gamma_{yy}\sqrt{G}e^{i\phi_G} \end{pmatrix}, \tag{5.1}$$

where Γ_{yy} is the passive reflection coefficient for the metasurface, and $\sqrt{G}$ and ϕ_G are the field gain magnitude and phase shift respectively for the y-polarized radiation incident transverse to the metasurface stripe antennas. Radiation polarized along the stripes (x-direction) is not amplified; ideally $|\Gamma_{xx}|= 1$, although finite metal conductivity, roughness, and diffraction losses may reduce this value.

The reflection Jones matrix for the output coupler polarizer is given by

$$\mathbf{\Gamma}_2 = \mathbf{R}(\theta_p)\mathbf{M}_{pol}\mathbf{R}(-\theta_p) = \begin{pmatrix} r_\perp \cos^2\theta_p + r_{||}\sin^2\theta_p & \left(r_\perp - r_{||}\right)\sin\theta_p\cos\theta_p \\ \left(r_\perp - r_{||}\right)\sin\theta_p\cos\theta_p & r_\perp \sin^2\theta_p + r_{||}\cos^2\theta_p \end{pmatrix} \tag{5.2}$$

where $r_{||}$ and $r_\perp$ are the reflection coefficients for a polarizer for radiations with polarization parallel and perpendicular to the wire grid direction respectively. Ideally $r_{||} = \sim$-1 and $r_\perp$=0, so that the maximum reflectance is achieved when $\theta_p = 0$.

Non-polarizing transmission loss through the etalon, atmosphere, or through diffraction losses is captured in the single pass transmission T, which results in a transmission matrix of

$$\mathbf{M}_T = \begin{pmatrix} \sqrt{T} & 0 \\ 0 & \sqrt{T} \end{pmatrix}, \tag{5.3}$$

The threshold condition is that the electric field vector repeats itself after one round trip:

$$\mathbf{E}_+ = \mathbf{M}_T\mathbf{\Gamma}_2\mathbf{M}_T\mathbf{\Gamma}_1\mathbf{E}_+ = \mathbf{M}_{RT}\mathbf{E}_+ \tag{5.4}$$

where $\mathbf{E}_+$ is the electric field vector incident upon the metasurface. The solution yields the threshold gain G_{th}, along with the polarization state of the field which can then be used to find the effective metasurface reflectance R_1 and output coupler reflectance R_2, and its transmittance $T_2 = 1 - R_2$. An accurate solution requires knowledge of the various complex reflection coefficients of the metasurface and output coupler, which are not experimentally known. However, we are able to make an estimate based upon data from numerical simulations. Fig. 5.5 shows the results of such a calculation for the effective output coupler reflectivity R_2, cavity field polarization angle θ_c, and optical coupling efficiency η_{opt}. The optical coupling efficiency is defined as η_{opt}=Q_{tot}/Q_{out} — the ratio of the total cavity quality factor to the quality factor associated with out-coupling. In particular, the optical coupling efficiency exhibits a very similar trend to the experimentally measured slope efficiency.

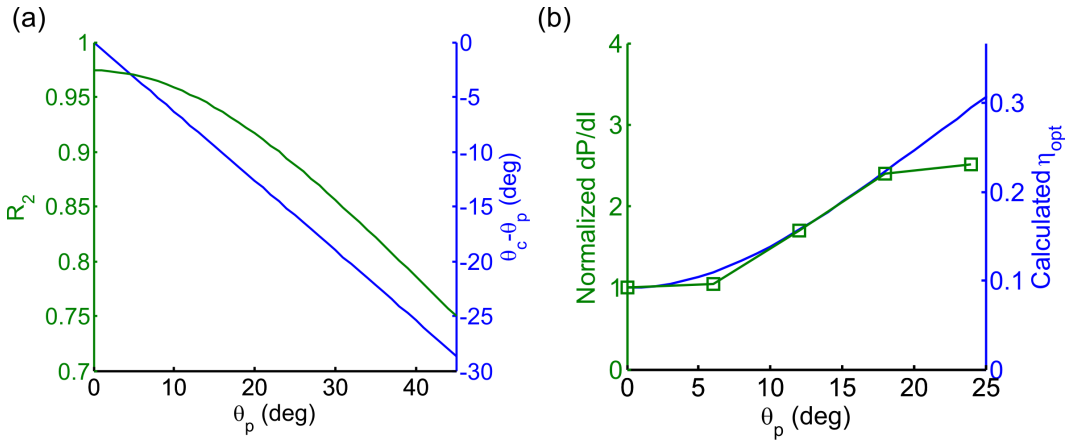

Figure 5.5: (a) Calculated effective output coupling reflectance R_2 change and the electric polarization angle of the cavity mode incident upon the output coupler with respect to the polarizer orientation angle ($\theta_c - \theta_p$) change with polarizer orientation angle θ_p. (b) Calculated optical efficiency η_{opt} change with polarizer orientation angle θ_p and the measured slope efficiency dP/dI normalized with respect to $dP/dI(\theta_p = 0°)$ at 77 K. The calculation results are based on the parameters simulated for the metasurface at 77 K.

The mode profile and far-field beam pattern are calculated y and θ_y direction, which both have near-Gaussian intensity profiles. The metasurface is modeled as a uniform distribution of unity reflectance across the metasurface, modified by a reflection phase shift difference of -112° between the passive reflector area at the edges and the central active area. These values are obtained from finite-element simulations and are shown in Fig. 5.6(a). The reflectivity on the polarizer is treated as unity uniformly. The calculated spot on the metasurface and the calculated far-field beams are plotted in Fig. 5.6(b) and (c). The calculated diffraction cavity loss is ∼7% per round trip. If the calculated ∼7% round-trip absorption and reflection loss due to the HR-Si window etalon is included, the total round-trip cavity loss is estimated to be ∼14%. The calculated far-field beam divergence is 3.4° which is ∼1-2° narrower than the measured divergence; the discrepancy may result from some factors not considered in the calculation. For example, the calculated beam is sensitive to the precise phase and gain

distribution on the metasurface, which in turn sensitively depends on the lasing frequency relative to the sub-cavity resonance frequencies, which may differ from our simulation.

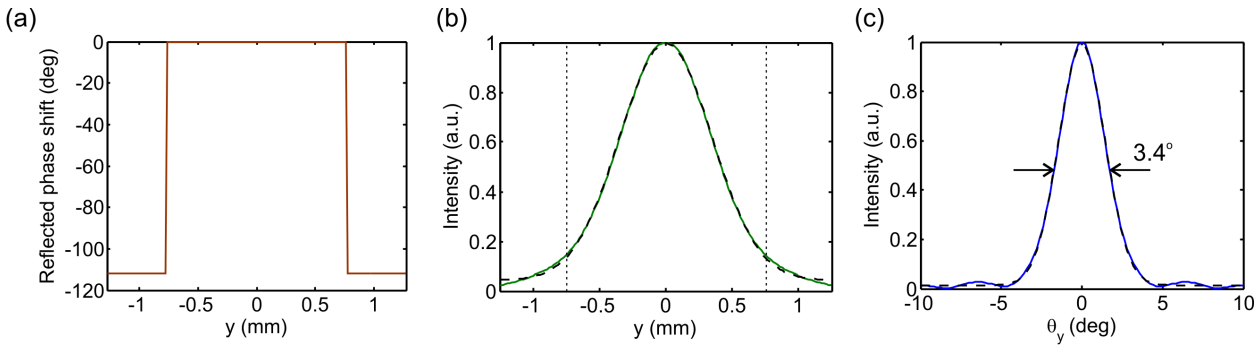

Figure 5.6: (a) The reflected phase shift on the metasurface reflector used in the calculation of cavity mode. (b) The calculated lowest-loss intensity profile on the metasurface with Gaussian curve fit (dashed line). The dotted line indicates the boundary between the active area and the passive reflector. (c) The calculated far-field beam pattern with Gaussian curve fit (dashed line).

Finally the measured slope efficiency is compared with the estimated one based on $\frac{dP}{dI} = N_p \frac{h\nu}{e} \eta_{opt} \eta_i \eta_u$ (see Sec. 3.2). From Fig. 5.6(b), the beam waist w_0 of the near-Gaussian on the metasurface is $\sim$0.75 mm, which leads to $\eta_u \approx 0.44$ using Eq. 3.13 for a square bias area of 1.5×1.5 mm^2. The optical output coupling efficnecy is calculated to be $\eta_{opt} = 0.4$ for $\theta_p = 30°$. Combined with $N_p = 178$, one obtains 352 mW/A (at 6 K) — about 4.4× larger than the measured value of measured $dP/dI = 80.4$ mW/A (at 6 K). The internal quantum efficiency η_i is likely to account for this discrepancy, which is expected to have a value of 0.25 - 0.75 (depending on the active region design, temperature and frequency). The discrepancy might also result from excess absorption on the metasurface, scattering loss, or diffraction loss due to cavity misalignment. Furthermore, the model presented here for slope efficiency assumes single-mode lasing interacting with a homogeneously broadened transition; an inhomogenously broadened gain transition will result in spectral hole burning

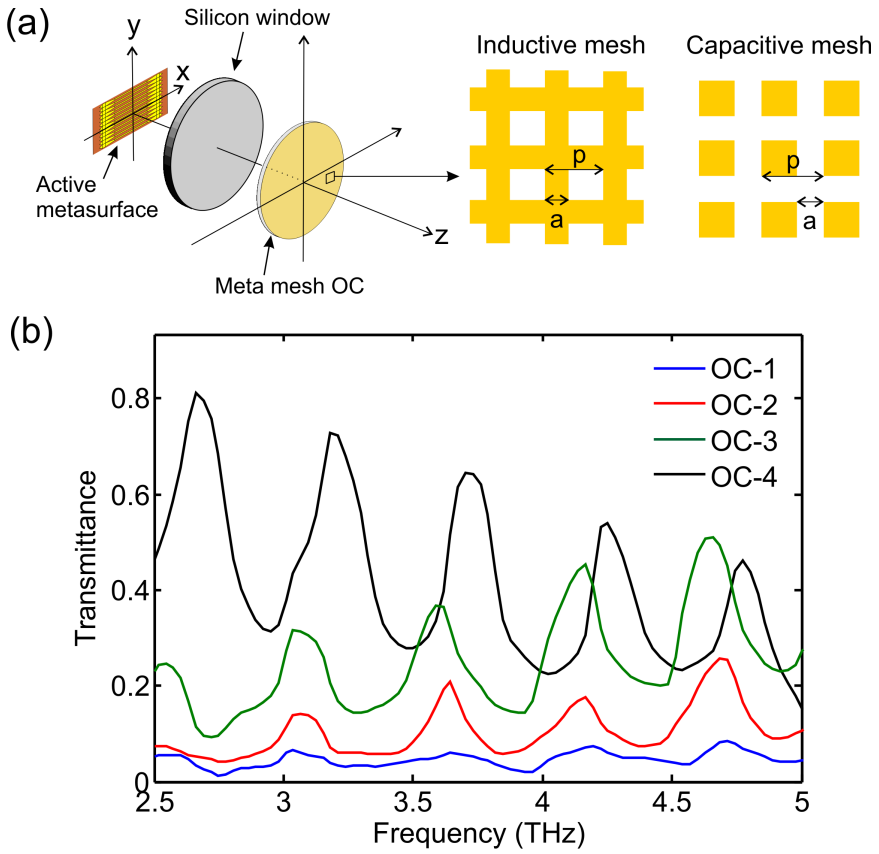

Figure 5.7: (a) Schematic of the QC-VECSEL setup using a metal mesh OC, composed of either an inductive mesh or capacitive mesh. p is the periodicity of the mesh and a is the size of mesh width/gap. (b) Measured transmission spectra for four metal mesh OCs.

and a reduction in efficiency.

5.4 Uniform metasurface paired with a metal mesh output coupler

One advantage of THz QC-VECSEL is the freedom of controlling output coupling efficiency. This can be done by turning the polarizer as explained above or simply using different metal mesh OCs varying in reflectance. A primary advantage of metal mesh OCs is that their reflectance is independent on the incident field polarization. Therefore using different metal mesh OCs provides a straightforward approach to study the loss from a passive metasurface,

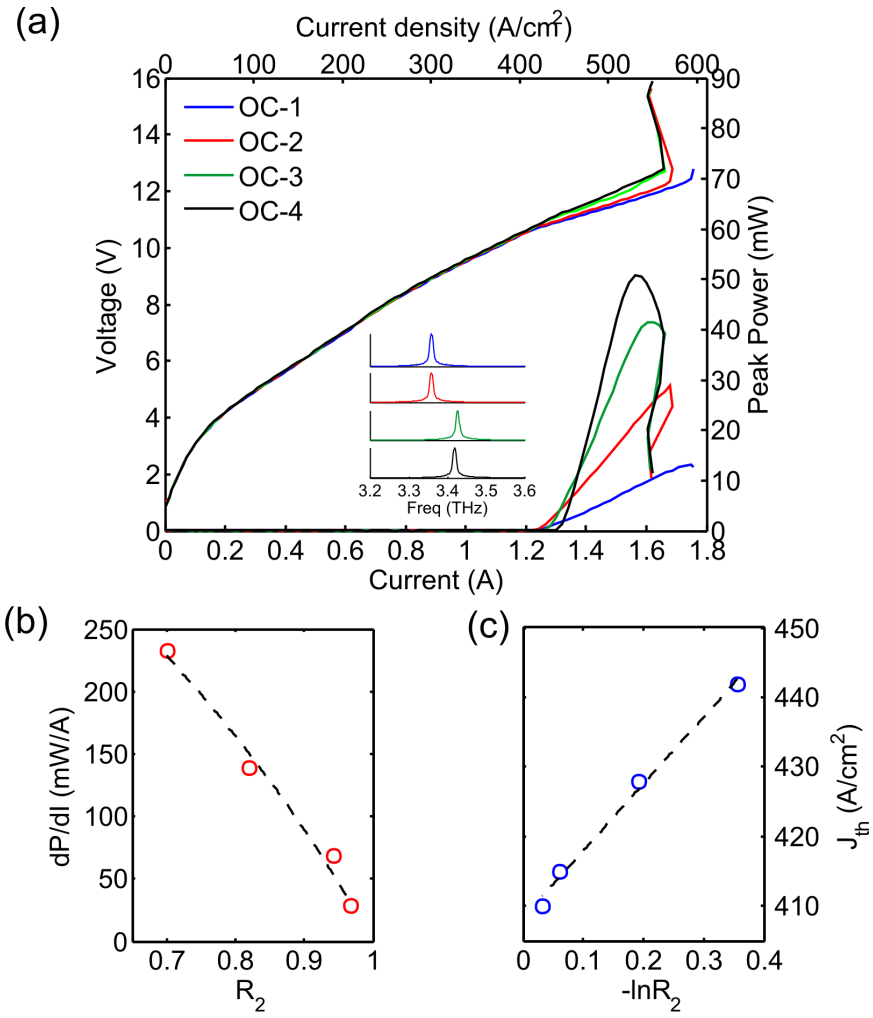

Figure 5.8: (a) Measured 77 K pulsed *P-I-V* for QC-VECSELs built with one metasurface and four OCs. The inset shows the lasing spectra for each VECSEL. (b) Slope efficiency change with the OC reflectance R_2. The black dashed line is the fitted curve. (c) Threshold current density J_{th} change with the OC reflection R_2 represented in $-\ln R_2$. The black dashed line is the fitted curve.

similar to extracting the waveguide guide loss by measuring lasers of various ridge length [185]. For this study, we used four output couplers (labeled as OC-1 to OC-4) to build the plano-plano FP cavity as shown in Fig. 5.7(a), which are fabricated all on one ∼100 μm-thick quartz substrate and comprised of either capacitive or inductive metal meshes of different sizes to systematically vary the reflectance R_2. The design parameters for OC1-4 are shown in Table 5.1. The metasurface used is a 2×2 mm^2 uniform design with 29 MM ridge micro-cavities of $w = 11.5$ μm ridge width and spaced with a $\Lambda = 70$ μm periodicity, designed for ∼3.4 THz. The QC active material used (RPC163-M1 design) has the design similar to Ref. [97]. A center circular area of 1.5-mm diameter is biased. No passive Au reflectors are placed on the two side to avoid the possible diffraction loss induced by the phase discontinuity as seen in Fig. 5.6(a). FTIR spectroscopy was used to measure the transmittance $T_2 = 1 - R_2$ at the relevant frequency, which gives 3.2%, 5.8%, 17.5%, 30% for OC1–4 respectively (spectra shown in Fig. 5.7(b)). Fig. 5.8(a) shows four *P-I-V* curves for the same metasurface paired with each OC. Due to the dependence of the OC's reflectance on frequency, the VECSEL lasing frequencies are slightly different. The slope efficiency *dP/dI* and the threshold current density J_{th} are extracted for each *P-I-V* and fitted with the expressions for slope efficiency and threshold current density based on Eq. 3.10, 3.11, and 3.12. We estimate 18% round-trip loss comprising 7% Si window loss and 11% diffraction loss obtained from Fox-and-Li cavity modeling (for this uniform metasurface-plano FP cavity of 9-mm cavity length) such that $T^2 = 0.82$. Fig. 10(b) and (c) show the extracted *dP/dI* and the threshold current density J_{th} with the curve fitting result. Fitting the data yields values of $R_1 = 0.62$, $\eta_i \eta_u = 0.29$, and $J_{leak} = 343$ A/cm^2. The measured passive reflection is close to the simulated value of 0.76 at resonance frequency of 3.4 THz. If we assume $\eta_u = 0.65$, this implies that the he

Table 5.1: Design parameters for the four different metal mesh OCs labeled as OC1-4.

Design label	Type of mesh	p (μm)	a (μm)
OC-1	Inductive	10	3
OC-2	Inductive	13	3
OC-3	Inductive	15	2.5
OC-4	Capacitive	15	2.5

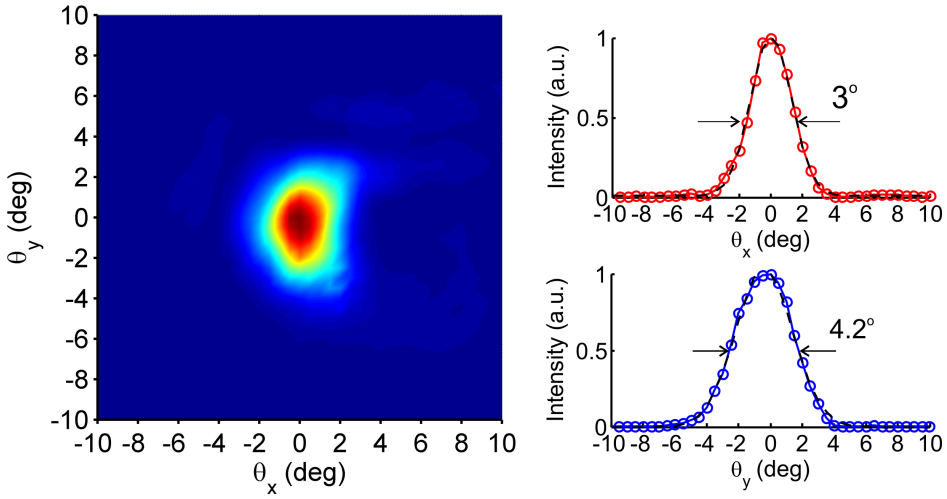

Figure 5.9: Beam pattern with 1D cuts in θ_x and θ_y directions for the QC-VECSEL using OC-3.

internal quantum efficiency at 77 K is $\eta_i = 0.45$. These values are relatively insensitive to the estimated value of T^2. The bulk gain increase per injected current density was extracted as $\sigma\tau_{eff}/eL_p = 0.64$ cm/A. This value was obtained assuming $\xi = 1.63\times10^{-2}$ cm from simulation data as in Sec. 3.4; however there is some uncertainty in ξ if VECSEL is in fact lasing slightly detuned from the metasurface resonance. Direct measurements of the metasurface reflectance and gain will be necessary in the future to directly measure this value. This QC-VECSEL also exhibits a directive near-Gaussian beam profile with $3° \times 4.2°$ FWHM divergence, showing an improvement from the previous demonstration with the polarizer (see Fig. 5.4(b)). This is likely attributed to the removal of phase discontinuity caused by the passive Au reflector that might disrupt the cavity mode.

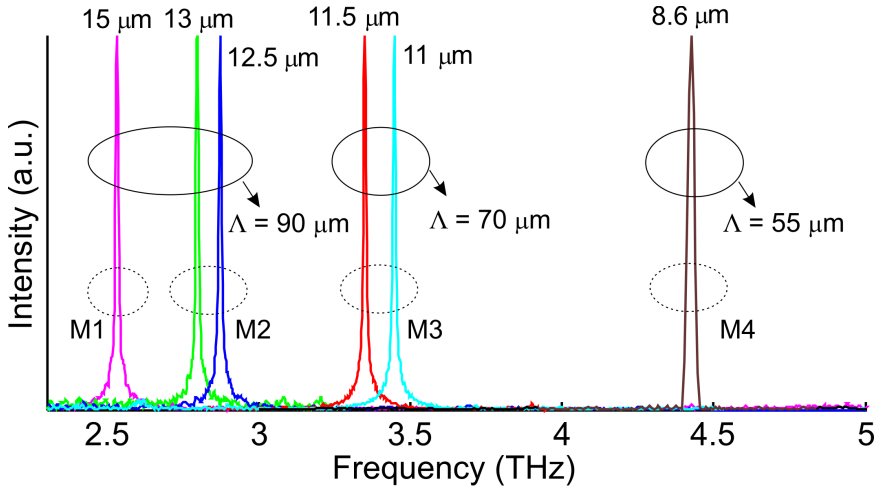

Figure 5.10: Measured lasing spectra for some demonstrated QC-VECSELs based on various metasurfaces designed with different ridge widths and periods Λ fabricated on different active QC-laser materials labeled as M1-4.

5.5 Spectral coverage

So far various QC-VECSELs have been demonstrated lasing in a range from 2.5–4.4 THz. This is achieved by designing metasurfaces with different periods Λ and ridge widths w and pairing them with various resonant-phonon QCL active region designs [97, 76]. The wide spectral coverage demonstrates the frequency flexibility of metasurface QC-VECSEL approach. Fig. 5.10 shows a family of lasing spectra from different THz QC-VECSELs, all of which were taken using the OC outside the cryostat (except the 4.4 THz demonstrated with a intra-cryostat cavity explained in Chapter 7). As expected, there is an approximate inverse relationship between ridge width w and the lasing frequency. Typically the lasing is in single-mode when the cavity length is optimized to achieve a maximum power output. This is attributed to the frequency dependence of the metasurface gain response, in conjunction with the etalon filter effect of the cryostat window. As the cavity is tuned away from its optimum length, hopping between longitudinal modes separated by the window's FSR and

lasing in multiple longitudinal modes are occasionally observed. Temperature change can also induce a longitudinal mode hop [174].

CHAPTER 6

External cavity QC-VECSELs with focusing metasurface

The ability to engineer the phase of scattered light from planar surfaces is a powerful tool for beam engineering, which allows one to replace bulky optical components with thin and flat equivalents. This concept was introduced in the microwave regime in the form of the reflectarray antenna, often used to replace space-fed parabolic reflectors [186–188]. In its most common realization, a reflectarray comprises arrays of resonant patch antennas, which are used to engineer a spatially dependent reflection phase by varying a critical dimension of the patch; reflectarray lenses of this type have been demonstrated in the mm-wave, THz, and mid-IR ranges [135, 189–191]. The concept has been further generalized across the infrared and visible spectrum, with both metallic, plasmonic, and dielectric antennas types used to create a huge variety of reflectarray and transmitarray metasurface optical components, including lenses for focusing and imaging [107, 192], flat optics for optical vortex generation [116]. As a critical building block for QC-VECSELs, the active metasurface provide an ideal platform to integrate advanced metasurface designs with the laser cavity to enhance the performance and develop new functionality.

This chapter focuses on the design and demonstration of QC-VECSELs using the inhomogeneous active metasurface in replacement of the uniform metasurface. Such an inhomogeneous reflectarray metasurface acts as a focusing element by mimicking a parabolic concave mirror, imposing a phase shift on the reflected wave that increases quadratically as the distance from the center. Since the reflectarray antenna elements are loaded with QC active materials, when electrically biased the metasurface amplifies the reflected beam as it focuses. In conjunction with a flat OC reflector, we use the focusing metasurface to create a QC-VECSEL in a hemispherical cavity as shown in Fig. 6.1(b), which is essentially a stable cavity. Thanks to the focusing effect, a significant improvement is observed in cavity stability and output beam pattern compared to a uniform metasurface configuration [174].

6.1 Focusing metasurface design

The focusing metasurface is composed of an array of inhomogeneous MM waveguide ridges, as shown in Figs. 6.1(a) and (c). Each MM waveguide is intended to operate around its TM_{01} mode cutoff, similar to the uniform metasurface design. Each ridge is tapered to the passive and lossy wire bonding areas on both ends, which helps to suppress the self-lasing in propagating waveguide modes. The focusing effect is achieved by spatially modulating the ridge width both along and transverse to the ridges (see Fig. 6.1(c)). Because of the resonance characteristics of MM waveguides, at a fixed frequency nearly 2π change in reflection phase can be obtained by altering the ridge width w around the resonance condition. Fig. 6.2(a) shows that a phase change of 311° is achieved by varying w from 9 μm to 14 μm. The designed 2×2 mm^2 focusing metasurface is made up of 29 tapered MM

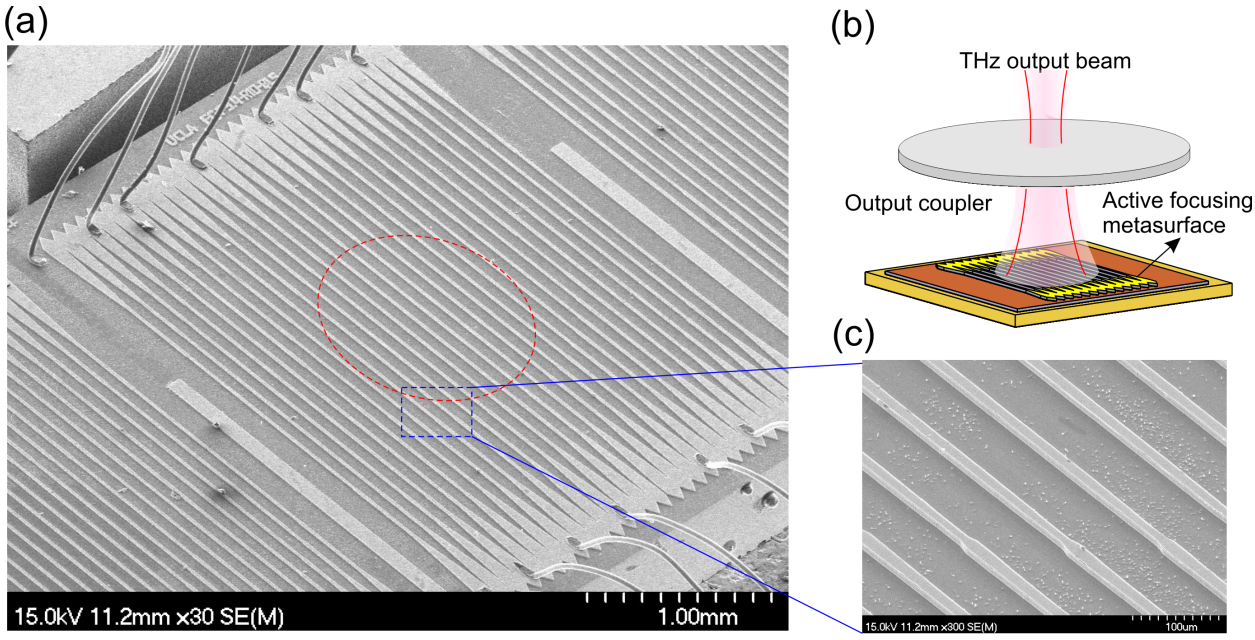

Figure 6.1: (a) SEM image of a 2×2 mm^2 active focusing metasurface with wire bonds. Only the part of ridges within the red dashed circle (1 mm diameter) are electrically biased; the area outside has a SiO_2 insulation layer between the top metal contact and the QC material. (b) Schematic for a THz QC-VECSEL based on an active focusing metasurface acting as an amplifying concave mirror. (c) Zoom-in SEM image of a part of the focusing metasurface showing the ridge width variation along and across the ridges

waveguide ridges spaced with a period of $\Lambda = 70$ μm, which is chosen to be smaller than the free space wavelength λ_0 to suppress Bragg scattering. The modulation in ridge width is designed to achieve the target parabolic phase profile (for paraxial focusing) of $2\pi r^2/R\lambda_0$, where r is the radial distance to the metasurface center and R is the effective radius of curvature (i.e. twice the desired focal length). The ridge width w at the metasurface center is chosen to match the resonant frequency of the element to intersubband gain spectrum peak. The fact that the reflectance is highest near the resonance frequency provides an approximate self-selection of the correct frequency to obtain the desired phase profile. As an example, a focusing metasurface designed with $R = 10$ mm at 3.4 THz has its transverse ridge width distribution through the center as shown in Fig. 6.2(b). Its focusing effect is verified by numerically simulating the reflection of a plane wave from it in 2D (see Fig. 6.2(c)) and confirmed by the result that the simulated phase profile matches with the target parabolic profile as shown in Fig. 6.2(b). Focusing metasurfaces with $R = 10$ and 20 mm for four different frequencies covering 3.2-3.5 THz are designed to overlap with the QC material bulk gain peak (designs labeled M3.2, M3.3, M3.4, M3.5). The active region design is similar to Ref. [97] (RPC163-M1 design). Not only is the phase spatially modulated, but the gain is as well. Oxide isolation is used such that only a 1-mm diameter circular region in the center of the metasurface receives current injection. This is a form of integrated spatial filtering which encourages lasing of the fundamental Gaussian cavity mode, since the center of the beam has the largest transverse confinement factor Γ_t with the gain.

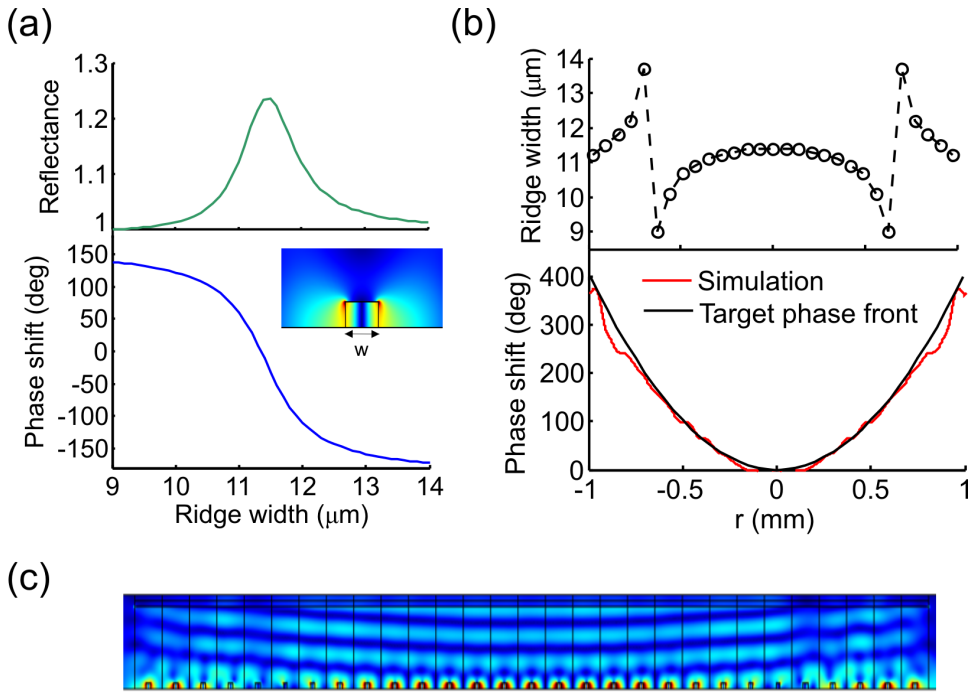

Figure 6.2: (a) Simulated reflectance (top) and reflection phase shift (bottom) versus ridge width for a MM waveguide array with period of 70 μm, with 30 cm^{-1} bulk gain assumed in the QC gain medium. Inset is the electric field amplitude profile of the excited TM_{01} mode in the reflection simulation. (b) Designed ridge width distribution for a focusing metasurface of $R = 10$ mm at 3.4 THz (top), and simulated phase front of reflected wave with a plane wave incident on it, in comparison with the target parabolic phase front (bottom). (c) Simulated electric field magnitude profile of a plane wave normally incident on a focusing metasurface of $R = 10$ mm at 3.4 THz.

6.2 Experimental demonstration

The experimental configuration for the focusing metasurface QC-VECSEL is shown in Fig. 6.3(a). The cavity length is 9 mm — the shortest length allowed by the experimental setup. The output coupler used here is either an inductive metal mesh on a 100 μm-thick quartz substrate (OC1) or a capacitive metal mesh on a 75 μm-thick quartz substrate (OC2), whose transmittance is measured to vary between 10–24% for the former and 40–60% for the latter, depending on the frequency within 3.2–3.5 THz due to the substrate's etalon effect.

Upon testing, it was immediately apparent that the focusing designs were easier to align and more tolerant of misalignment compared to uniform metasurface designs. This was quantified by first optimizing the alignment of the cavity to achieve parallelism, and then intentionally introducing angular misalignment in either the x or y axis represented by tilt angles δ_x and δ_y respectively (see Fig. 6.3(a)). A host of pulsed optical power-current-voltage (P-I-V) curves (see Fig. 6.3(b)) were measured for increased tilt angles in both axes for QC-VECSELs built upon three metasurfaces: focusing ones of R = 10 mm and 20 mm, and a uniform metasurface similar to the design in Sec. 5.1. The pulsed P-I-V measurements were conducted with 0.25% overall duty cycle (500 ns-long pulses repeated at 10 kHz, modulated by a slow 5 Hz pulse train with lock-in detection). To make a fair comparison, for each device the measured change in threshold current density J_{th} is plotted normalized to J_{th} measured at optimum alignment (see Fig. 6.3(c)). The threshold current increases with the tilt angle in both axes in a modest manner for the two focusing metasurface QC-VECSELs — devices still lase even with 4° misalignment. In contrast, the uniform metasurface exhibits a more dramatic rise in J_{th} with misalignment, and ceases to lase entirely

for misalignments greater than 3.5°. This is the case even though the uniform metasurface has a larger circular biased area of 1.5-mm diameter and consumes more current. We conclude that the focusing effect significantly reduces the cavity's sensitivity to misalignment, as expected for the hemispherical Gaussian resonator. The experimental result matches the trend of our simulated results, in which modified Fox-and-Li cavity calculation is used to estimate the threshold bulk gain g_{th} for each QC-VECSEL to lase at different misaligned angles. The threshold bulk gain is found by using a root finder algorithm to find the value of the metasurface reflectivity for which the computed round-trip cavity loss is zero, as detailed in Sec. 4.4. The angular misalignment is introduced as a linear shift of the OC's reflection phase. The calculation results reveal a slower trend of threshold bulk gain increase with misalignment for the two focusing metasurfaces than for the uniform one, as shown in the top part of Fig. 6.3(c). Because not all loss mechanisms are included in this simulation, it should only be used to identify the trend in threshold current density.

High power output and slope efficiency are demonstrated from the focusing metasurface QC-VECSELs. All four separate metasurfaces designed for four frequencies covering 3.2–3.5 THz were observed to lase, with the one designed for 3.4 THz (M3.4) showing the best power performance. At perfect alignment and 77 K, the R = 10 mm metasurface QC-VECSEL designed for 3.4 THz generates a peak power of 46 mW with the slope efficiency $dP/dI = 413$ mW/A when paired with OC2, and 31 mW peak power with $dP/dI = 227$ mW/A with OC1, *P-I-V* curves of which are plotted in Fig. 6.4(a). At 6 K, the pulsed peak power increases to 78 mW, with $dP/dI = 572$ mW/A with OC2 and a peak wall-plug efficiency reaching 1.15%. cw lasing is achieved at 6 K with peak power of 40 mW, $dP/dI = 339$ mW/A, and wall-plug

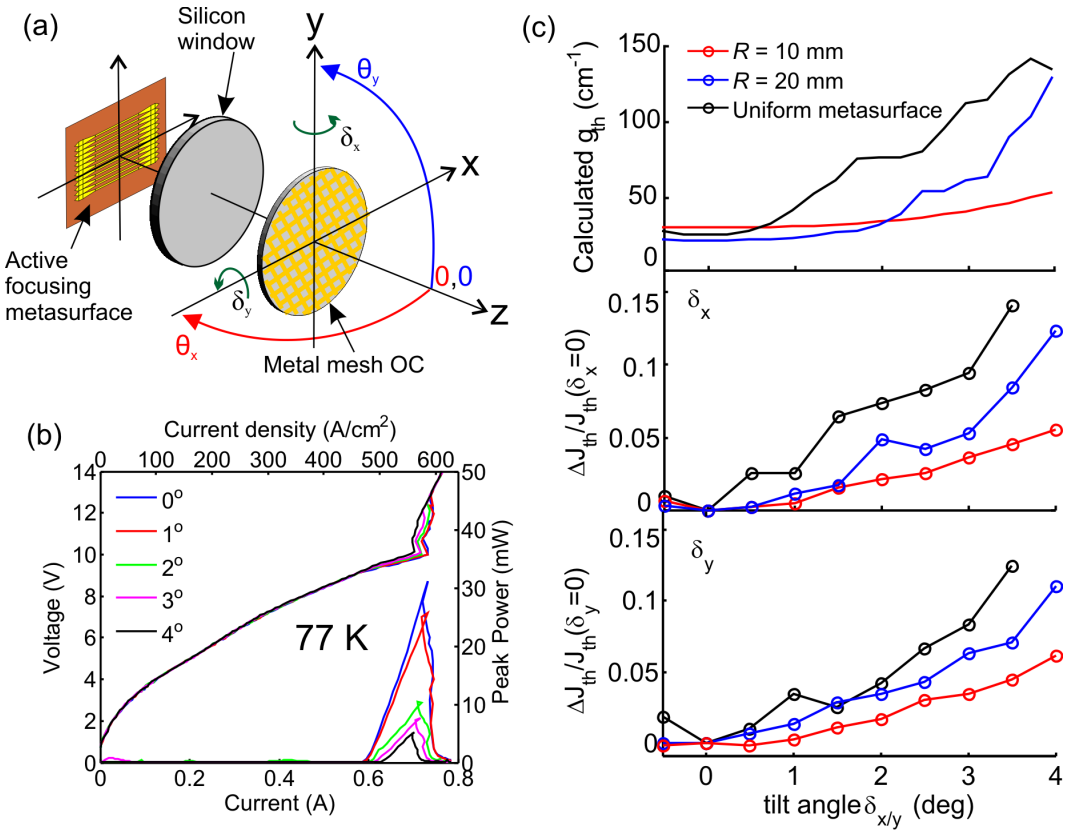

Figure 6.3: (a) Experimental configuration of a focusing metasurface QC-VECSEL. The tilt angle $\delta_{x/y}$ indicates the degree of OC tilting around y/x axis from the perfectly aligned position, as the green arrows show. (b) Pulsed P-I-V curves at 77 K for different y (with $\delta_x = 0$) for a $R = 10$ mm focusing metasurface (M3.4). (c) The measured threshold current density change ratio with respect to J_{th} at perfect alignment with δ_x and δ_y for QC-VECSELs based upon three different metasurfaces: $R = 10$ mm and 20 mm with 1 mm diameter circular bias area, and a uniform metasurface with 1.5 mm diameter circular bias area. The solid lines in the top part are the calculated threshold bulk gain g_{th} change with the tilt angle δ_y.

efficiency of 0.6%. (see Fig. 6.4(b)). The power is measured using a pyroelectric detector, which has been calibrated using a Thomas-Keating THz absolute power meter with 100% collection efficiency, given directive beam pattern. For a comparison, the 77 K *P-I-V* of a uniform metasurface QC-VECSEL is measured and shows $dP/dI = 234$ mW/A when paired with OC1. The output power drops dramatically when this uniform metasurface is paired with OC2. Even though the focusing metasurface is designed with a smaller circular bias area (1-mm diameter) than the uniform metasurface (1.5 mm diameter), higher efficiency performance is obtained from the focusing metasurface VECSEL, with the slope efficiency among the best reported numbers so far from a THz QCL. The smaller biased area of the focusing design has reduces the total current consumption and benefits cw operation. Further reduction of the biased area may help to obtain cw performance at higher temperature >77 K. The lasing spectra for four separate focusing metasurface VECSELs designed for 3.2–3.5 THz at 77 K are shown in Fig. 6.4(c). The spectra are generally close to the designed metasurface frequencies, which is primarily determined by the ridge width at the metasurface center. All lased in single-mode over their entire bias range. This is attributed to the etalon filter effect of the cryostat window. This effect, in combination with the limited bandwidth of the metasurface reflective gain, and the QC material gain lineshape, strongly favors single-mode operation.

The benefit of the focusing metasurface can also be seen by looking at the beam quality. The far-field beam at 77 K is measured as shown in Fig. 6.3(a) using a 2-axis spherical scanning pyroelectric detector. Beams from the focusing QC-VECSELs both exhibit a narrower and more circular near-Gaussian beam profile than the beam pattern reported in [174] or in

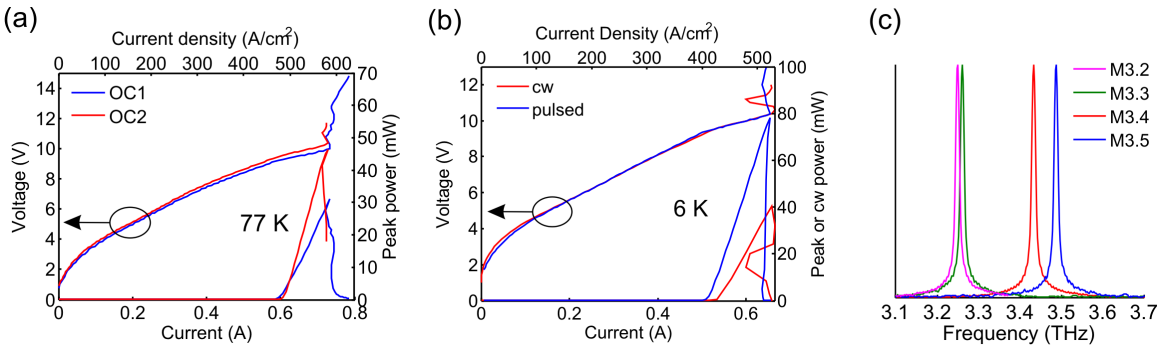

Figure 6.4: (a) Pulsed P-I-V curves for the $R = 10$ mm focusing metasurface QC-VECSEL designed for 3.4 THz, paired with OC1 and OC2 respectively at 77 K. (b) Pulsed and cw P-I-V curves for the QC-VECSEL composed of the $R = 10$ mm focusing metasurface and OC2 at 6 K. (c) Lasing spectra measured using a Nicolet FTIR using 0.25 cm^{-1} resolution for QC-VECSELs based on four focusing metasurfaces M3.2, M3.3, M3.4, and M3.5 paired with either OC1 or OC2

Sec. 5.4 from a uniform metasurface. As shown in Figs. 6.5(a) and (b), the QC-VECSEL on $R = 20$ mm focusing metasurface produces a beam with $3.5° \times 3.6°$ FWHM angular divergence, and the QC-VECSEL with the $R = 10$ mm metasurface produces a beam with $4.8° \times 4.3°$ divergence. This agrees with the expected divergence behavior of Gaussian modes in hemispherical resonators — the smaller value of R produces a smaller spot on the output coupler, with consequent faster divergence in the far-field. The beam is well fit by a Gaussian intensity profile at least down to 25 dB, and in some cases down to 40 dB.

The iterative Fox-and-Li approach is applied to calculate the intracavity mode profiles. To evaluate the impact of the nonuniform distribution of reflectance on the metasurface focusing effect, the cavity mode profiles and far-field beam patterns are calculated and compared for four cases: (i) ideal Gaussian cavity with a smooth parabolic phase for $R = 10$ mm and uniform unity reflectance, (ii) the actual $R = 10$ mm focusing metasurface design with phase profile modulated by the ridge width distribution transverse to the ridge array and a fictitious uniform reflectance, and the actual $R = 10$ mm focusing metasurface design with

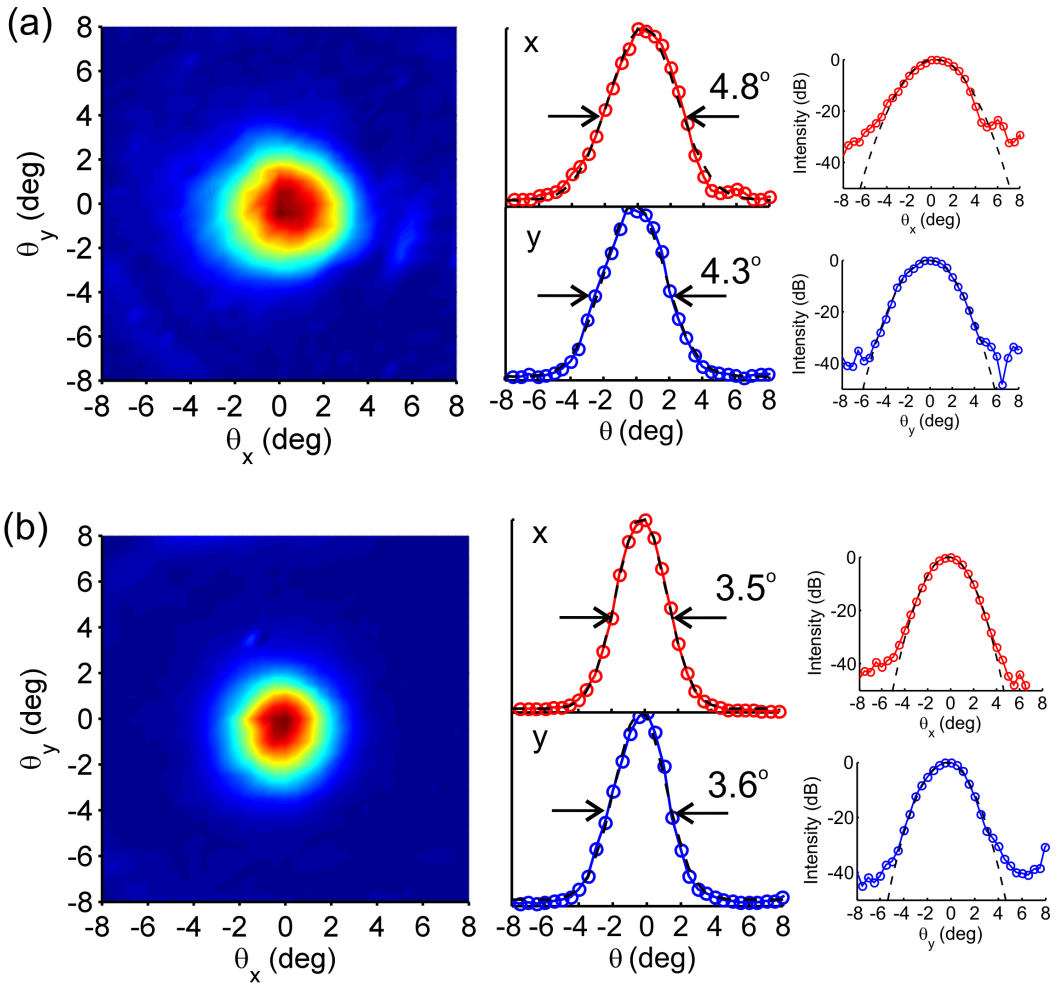

Figure 6.5: (a) The measured beam pattern from a focusing metasurface QC-VECSEL with $R = 10$ mm. (b) The measured beam pattern from a focusing metasurface QC-VECSEL with $R = 20$ mm. The angular resolution in measurement is 0.5°. Black dashed lines are Gaussian curve fits to the 1D beam cuts through the beam center. 1D beams cuts are also plotted dB scale. Beams are measured at 77 K.

a nonuniform reflectance distribution for 30 cm^{-1} (iii) and 60 cm^{-1} (iv) gain within the active material. Fig. 6.6(a) shows the associated metasurface reflectivity magnitude and phase distributions. The nonuniform reflectance data was obtained by using finite-element simulation to obtain the metasurface reflectance as a function of ridge width. It is assumed that sub-cavity elements within the center 1 mm are biased to produce a bulk gain coefficient of 30–60 cm^{-1} within the active material, and the other elements outside are unbiased so that they are lossy. The range of gain values considered corresponds to operation with different OCs, i.e. a more transmissive output coupler will require larger threshold gain to oscillate. Since the metasurface resonance is approximately Lorentzian in lineshape, the modulation of the ridge width to produce the desired phase profile also produces a spatially varying gain profile at a fixed frequency, whose variation depends upon the total cavity loss. Fig. 6.6(b) shows the calculated intensity far-field beam pattern, as well as the modal profiles on the metasurface and the output coupler, for each of the four cases. The results show that the field distributions are very similar. Therefore we believe that the nonuniform reflectance distribution has only a minor effect on the focusing metasurface cavity mode.

6.3 M^2 factor characterization of output beams

To further assess the beam quality, the beam propagation factor M^2 is measured using a knife edge method through the focus of the beam along the propagation direction [193]. The M^2 factor is the ratio of the angle of divergence of a laser beam to that of a fundamental Gaussian TEM_{00} mode with the same beam waist diameter; it has a value of unity for a fundamental Gaussian beam [194]. Following the standard procedures detailed in [195], a value of M^2 =

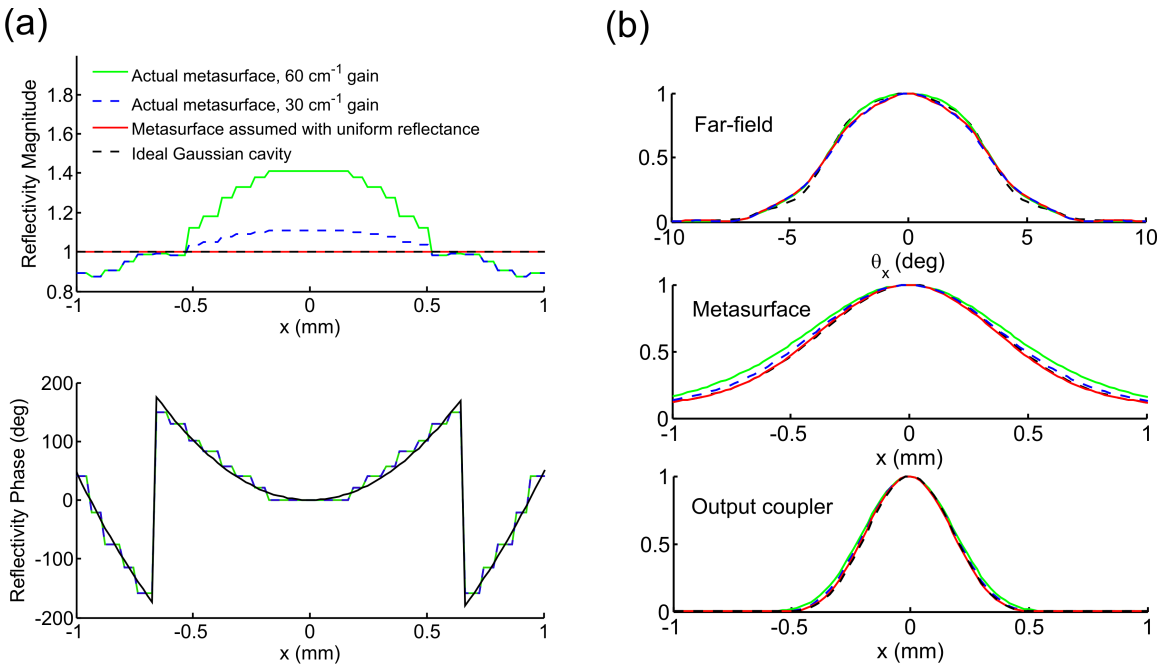

Figure 6.6: (a) Reflectivity magnitude and phase distributions for the four calculation cases. (b) Calculated far-field beam patterns, cavity mode intensity profiles on metasurface and OC for the four cases.

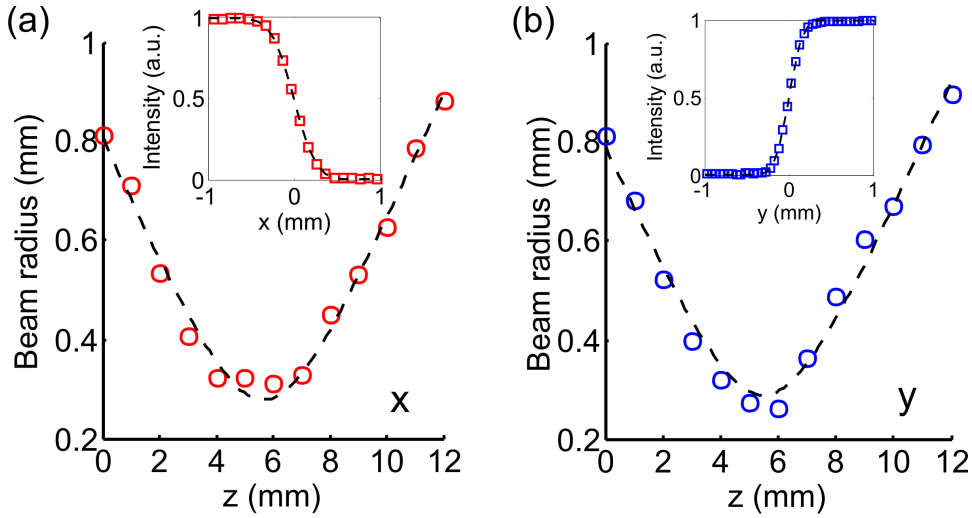

Figure 6.7: M^2 factor measurement results for the output beam directly from a focusing metasurface QC-VECSEL with $R = 20$ mm. The beam radius is measured along the optical axis (z axis) in both x and y direction after being focused by a TPX lens of 50-mm focal length which is placed 17 cm away from the VECSEL, and is represented by red and blue circles in (a) and (b), with the curve fitting results plotted in black dashed line. The inset shows the knife-edge measurement raw data at beam waist position with curve fitting shown in black dashed curve.

1.3 is measured in both the x and y directions for $R = 20$ mm metasurface QC-VECSEL, which is the best reported M^2 factor directly from a THz QC-laser based on MM waveguide geometry with no spatial filtering [194]. The beam waist evolution along the optical axis is shown in Fig. 6.7, with parameter fitting results. The peak power associated with this beam is 27 mW at 77 K, which leads to a high value of brightness $B_r = 1.86 \times 10^6$ $\mathrm{Wsr^{-1}m^{-2}}$ given by $B_r = P/(M_x^2 M_y^2 \lambda^2)$, where P is the output power. The M^2 value for $R = 10$ mm metasurface QC-VECSEL with OC2 is measured to be 2.2 and 2.5 in x and y directions respectively, with the output power of 46 mW and $B_r = 1.07 \times 10^6$ $\mathrm{Wsr^1m^2}$. The slight beam degradation may be due to the stronger diffraction occurring for such a cavity where the cavity length is closer to the focusing curvature radius. We note that only providing electrical bias to the center circular area with diameter of 1 mm is important in achieving high beam quality. By pumping only the center of the metasurface, the fundamental Gaussian mode exhibits the highest overlap, and is selectively excited. Also, even for the $R = 10$ mm design, the ridge widths w are relatively uniform within the center biased region (see Fig. 6.2(b)), which limits the spectral broadening of the gain due to metasurface inhomogeneity.

CHAPTER 7

Intra-cryostat cavity QC-VECSELs

The metasurface QC-VECSELs implemented in the external cavity have demonstrated the success in achieving high power in combination with excellent beam pattern. One direction of advancing QC-VECSELs is to further improve its compactness and performance by designing a miniatured cavity that can be contained within the cryostat, namely an intra-cryostat cavity. This type of cavity removes the loss and etalon filtering effect associated with the cryostat window and atmosphere. Besides, a much shorter cavity length is possible with the intra-cryostat setup, which leads to a lower diffraction loss and less sensitivity to cavity misalignment. Once built and aligned, this type of intra-cryostat cavity is robust and free of further alignment, making it a convenient THz source with high performance for many applications. This chapter focuses on the design and experimental demonstration of intra-cryostat QC-VECSELs, highlighted with record-high slope efficiency and cw power at >77 K in conjunction with a near-Gaussian beam pattern.

7.1 Intra-cryostat cavity design

A miniatured mechanical mount is designed to hold the OC, which is typically a metal mesh OC, right on top of the metasurface mounted on a heat-sunk copper chip carrier, a schematic

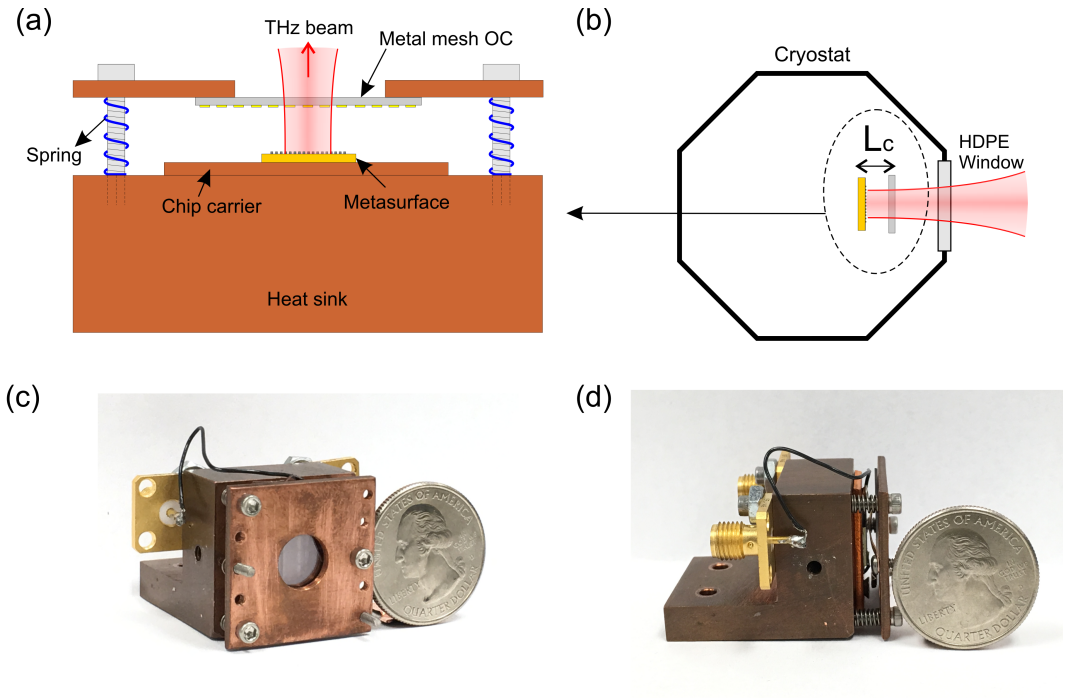

Figure 7.1: (a) Schematic of the intra-cryostat cavity design. (b) Schematic of the intra-cryostat QC-VECSEL mounted inside a cryostat. Front (c) and side (d) views of the actual intra-cryostat cavity setup.

of which is shown in Fig. 7.1(a). The actual cavity setup is shown in Fig. 7.1(c) and (d). Three screws through the OC holder are each supported by a compression spring, providing a mechanism for fine tuning the parallelism between the OC and metasurface. This tuning is conducted at RT externally with the aid of a He-Ne laser, after which the entire cavity is mounted onto the cold stage inside the cryostat. To avoid the elton filtering effect on the power transmitting through the cryostat window, the silicon window is replaced with a relatively rough high-density polyethylene (HDPE) window whose etalon effect is suppressed, as shown in Fig. 7.1(b), the transmittance of which is measured ~62% within 3–4 THz. After cooldown, it is possible that thermal contraction may introduce angular misalignment and we lack access to correct it. To mitigate the effect, it is helpful to use short cavity length of 2–3 mm in order to keep the diffraction loss due to OC misalignment at a low level.

Use of a focusing metasurface is also helpful, although not essential, to reduces the effect of misalignment.

7.2 Experimental results

7.2.1 Record-high slope efficiency at 77 K

Some of the best performing QC-VECSELs to date have been achieved in this intra-cryostat cavity. An example is a device with a high peak power of 140 mW in pulsed mode at 77 K, which is based on a 2-by-2 mm^2 uniform metasurface with 11.5-μm ridge width and 70-μm periodicity, and with a center circular area of 1 mm diameter biased. The power is corrected with the HDPE window transmittance taken into account. The pulsed *P-I-V* curve measured is shown in Fig. 7.2(a). The slope efficiency is a record-high 745 mW/A for a THz QC-laser at 77 K, which corresponds o roughly 0.33 photons emitted per electron per stage above threshold. The peak wall-plug efficiency reaches 1.5%. The OC (labeled as OC1) used has its transmittance at 18–20% in the lasing frequency range. The measured spectra show lasing in two neighboring longitudinal modes at low biases, which gradually evolves to the high frequency mode with a higher bias due to the Stark effect in quantum wells. At the peak power bias, the lasing is essentially single-mode. The two modes are separated by 61 GHz (measured with a FTIR spectrometer with 7.5 GHz resolution), from which we can infer that the cavity length is 2.5 mm. Accompanied with the high power output is a near-Gaussian circular beam pattern with a FWHM divergence angle of $4.9^\circ \times 4.3^\circ$, as plotted in Fig. 7.2(c).

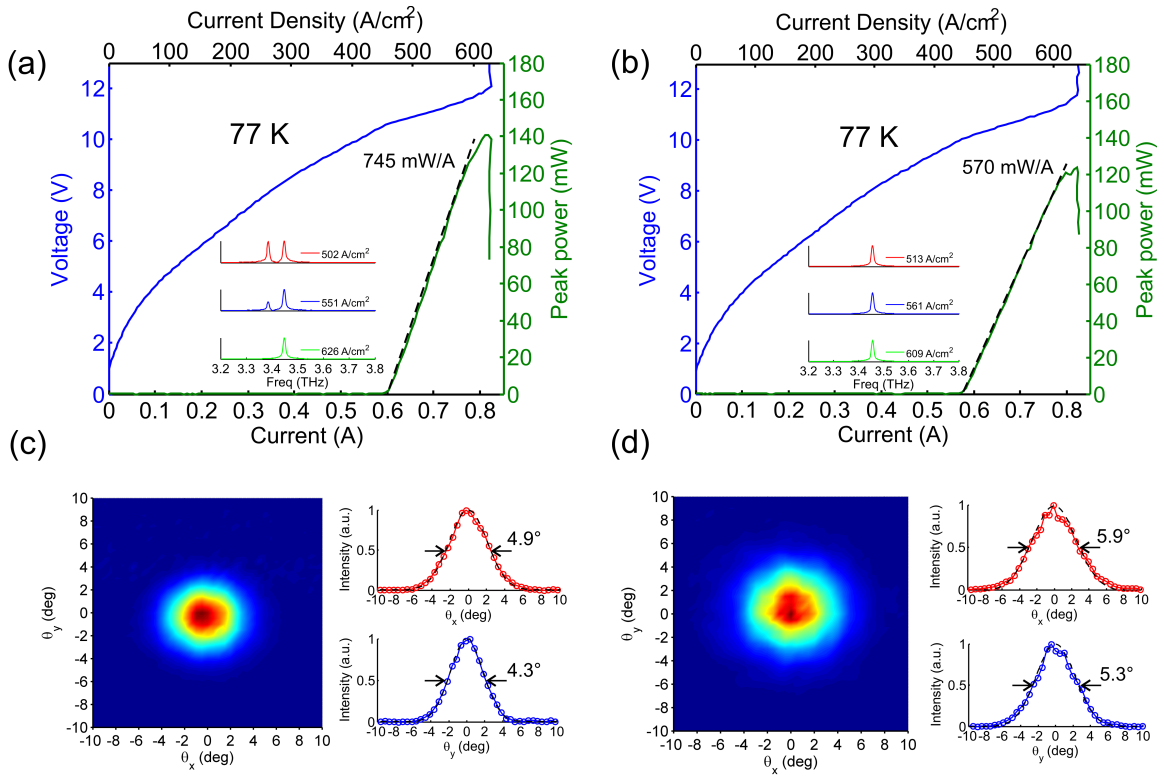

Figure 7.2: (a) Pulsed *P-I-V* for the intra-cryostat QC-VECSEL based on the uniform metasurface. Inset is the lasing spectra at different injection current levels. Its beam pattern is shown in (c). (b) Pulsed *P-I-V* for the intra-cryostat QC-VECSEL based on the focusing metasurface. Inset is the lasing spectra at different injection current levels. It beam pattern is shown in (d). Black dashed lines are the fitted curve.

Comparative performance is achieved from another demonstration with a 2-by-2 mm^2 focusing metasurface designed with $R = 20$ mm and a center circular bias area of 1-mm diameter, paired with OC1 also. The pulsed *P-I-V* curve of which is shown in Fig. 7.2(b). A peak power of 120 mW is achieved, with a slope efficiency of 570 mW/A. Single-mode lasing is observed over the entire dynamic range at 3.457 THz, which might be the cause of slightly lower slope efficiency than the uniform metasurface QC-VECSEL as a result of spectral hole burning. A near-Gaussian far-field beam pattern is measured with $5.9° \times 5.3°$ FWHM divergence. The calculated results using the Fox-and-Li approach also suggests a broader far-field divergence with the focusing metasurface than the uniform metasurface.

We attribute the high power and efficiency performance from this intra-cryostat QC-VECSEL to the removal of cryostat window loss and air absorption loss, as well as the shortened cavity length that reduces the cavity diffraction loss. This is reflected in the reduced threshold current density J_{th} as the OC is placed inside the cryostat for an identical metasurface, as shown in Fig. 7.3. The loss minimization is also very critical to achieving cw operation at a high temperature (at or above 77 K). In fact, these two QC-VECSELs have been tested in cw at 77 K. The uniform device does not lase, while the focusing device exhibits non-steady lasing with the power peaked at 35 mW, which however rolls off with time until lasing ceases. Compared with the uniform one (with $J_{th} = 455$ A/cm^2), the temporary lasing is likely due to a lower threshold current density of 435 A/cm^2 for this focusing device. The non-steady cw lasing suggests that the total power consumption of $\sim$9 W still exceeds the thermal dissipation capability of the cryostat, which results in a significant rise of electronic temperature in QC material that kills lasing. Therefore it is

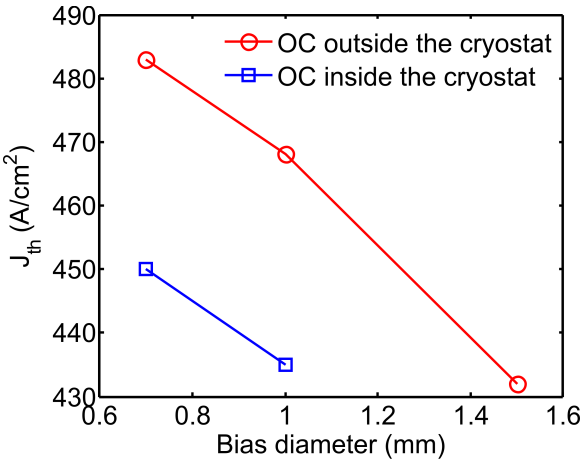

Figure 7.3: Measured threshold current densities for focusing metasurface VECSELs based on an identical metasurface design with the only difference in the diameter of the center circular bias area. They are paired with the same OC in two cavity geometries: OC mounted outside and inside the cryostat with cavity length of ∼9 mm and 2-3 mm respectively.

concluded that to achieve steady cw operation at 77 K the total power consumption has to been further reduced below ∼9 W.

7.2.2 Record-high cw power at 77 K

In an attempt to achieve cw lasing at 77 K, a focusing metasurface (with $R = 20$ mm) is designed with a smaller than usual bias area (with 0.7-mm bias diameter) and built into a cryostat cavity with a more reflective OC (with $\sim 5\%$ transmittance). Steady cw operation with an output power of >5 mW is obtained from this QC-VECSEL at 82 K, which is further improved to 14 mW at 16 K, as shown in Fig. 7.4(a). This is much higher than previous records for cw power at 77 K, which have typically been from 1–2 mW in MM waveguides [85, 76, 84]. The pulsed and cw lasing spectra at different biases are shown in Fig. 7.4(b). The single-mode cw lasing fixed at 3.403 THz is also seen at 6 K. The only drawback of reducing bias area is the resulting increase in threshold current density shown in Fig. 7.3,

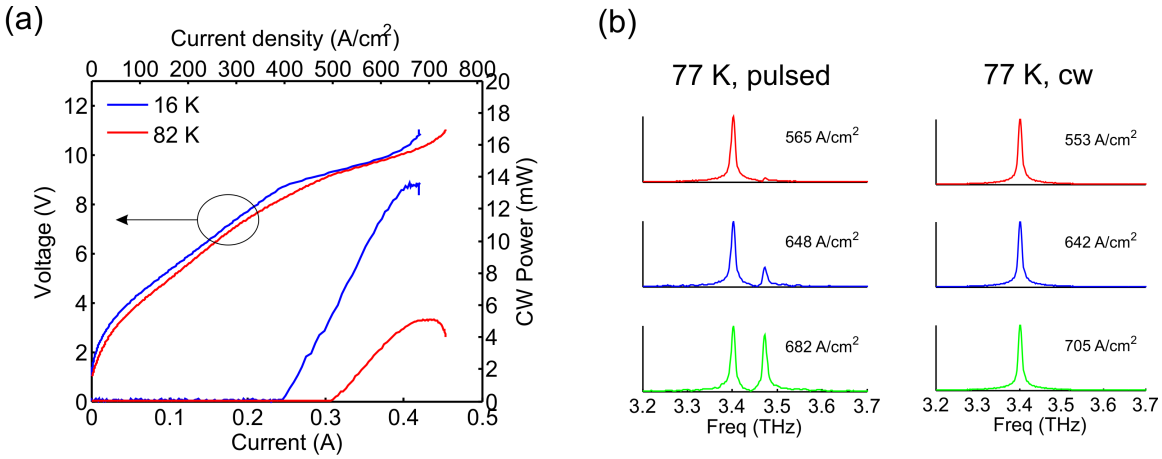

Figure 7.4: (a) cw *P-I-V*s at 16 K and 82 K for the intra-cryostat QC-VECSEL based on a focusing metasurface designed with 0.7-mm diameter circular bias area. (b) Lasing spectra at 77 K for pulsed and cw mode at different current injection levels.

due to the reduced transverse confinement factor Γ_t (see Sec. 3.3). The beam pattern from this QC-VECSEL is first measured in pulsed mode, which exhibits a near-Gaussian beam profile with $5.3^\circ \times 5.3^\circ$ FWHM divergence as shown in Fig. 7.5(a). The 1D beam profiles are also measured in cw mode, which match with the pulsed beam profiles very well as plotted in Fig. 7.5(b). It indicates that the thermal lensing effect, which is noticeable for VECSELs in the visible and near-infrared range [98], has a negligible effect on THz QC-VECSELs operated at cryogenic temperature. This is attributed to the fact that the refractive index does not change strongly with temperature in GaAs for low lattice temperatures [196], which is also reflected in the very limited frequency tuning of $\sim 4 \times 10^{-3}$ with a operating temperature change of ~90 K for a THz QCL [197]. In summary, a high-performance compact cavity QC-VECSEL has been demonstrated with record-high cw power at 77 K in a high-quality near-Gaussian beam pattern.

The thermal performance of this cw QC-VECSEL is further evaluated by measuring a host of pulsed *P-I-V*s at various cryostat temperature. This is a standard characterization of

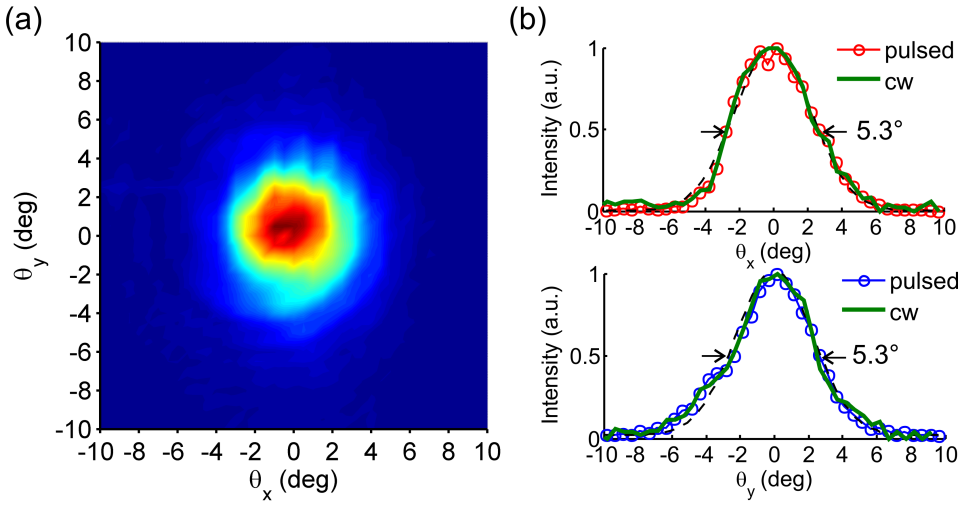

Figure 7.5: (a) Beam pattern measured at 77 K in pulsed mode. (b) 1D beam profiles measured at 77 K in cw mode, compared with the pulsed mode profiles. Black dashed lines are the fitted curves.

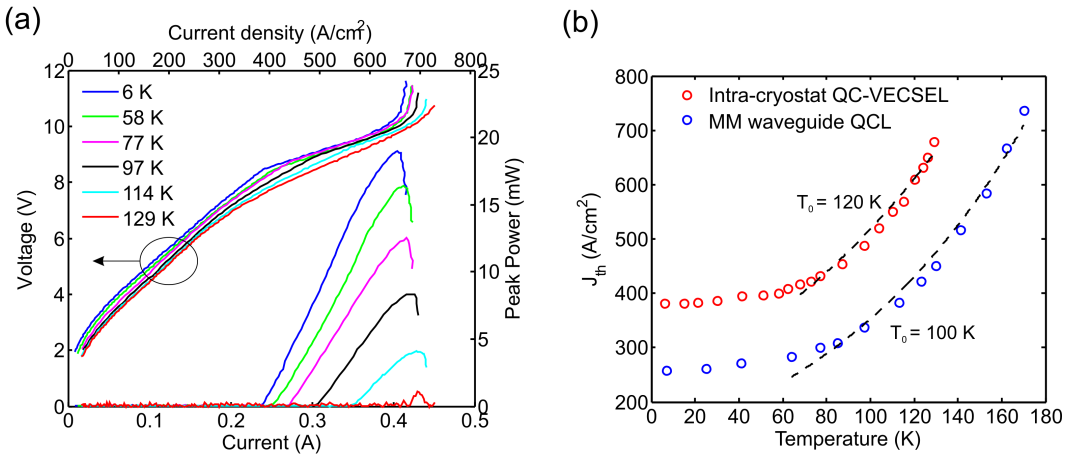

Figure 7.6: (a) Pulsed P-I-Vs at different cryostat temperature. (b) Measured threshold current density J_{th} versus cryostat temperature, with curve fits plotted in black dashed line.

a laser's thermal performance, but it is not very feasible for the external cavity QC-VECSELs because changing temperature in a large range causes lasing to turn on and off; this is because the thermal expansion on the metasurface side alters the cavity length, which disrupts the phase matching that satisfies the Si window's etalon effect. Now with the intra-cryostat cavity, this characterization is allowed with no etalon filter. The threshold current density J_{th} is extracted and plotted against the temperature in Fig. 7.6(d), which demonstrates $T_{max} =$ 129 K as shown in Fig. 7.6(c). The characteristic temperature $T_0 = 120$ K is extracted by fitting the data points above 65 K to the exponential function $J_{th} = J_0 \exp(T/T_0)$. The lasing is single-mode in pulsed mode over the most of dynamic range until another longitudinal mode develops at very high bias, as shown in Fig. 7.2(b). For comparison, the J_{th} dependence on temperature is also measured for a conventional MM waveguide QCL with 1.47-mm length and 50-μm width fabricated on the same QC material, which exhibits $T_{max} = 170$ K and $T_0 = 100$ K. Given that the total bias area of MM waveguide QCL is very close to the QC-VECSEL, a higher T_0 for QC-VECSEL could be an indication of better heat dissipation efficiency of the metasurface with a sparse thermal density than a single big MM ridge with all power aggregated together. But more evidence is needed to substantiate this point, since the small difference of T_0 might as well be a result of different temperature ranges for the two data groups. The lower T_{max} for the QC-VECSEL is attributed to the much higher J_{th}, which shows an offset of $\sim$120 A/cm^2 above J_{th} for the MM waveguide QCL, as seen in Fig. 7.6(b). This could be a consequence of multiple factors: (a) MM microcavities operated at TM_{01} mode on the metasurface is intrinsically lossier than the fundamental TM_{00} mode that the MM waveguide operates in, (b) there exists additional losses in the QC-VECSEL than the MM waveguide, including diffraction loss, absorption loss of metal mesh OC, and

excess absorption on the metasurface, (c) QC-VECSEL has a higher optical output coupling loss (estimated to be 12%) than the MM waveguide with cleaved facets (typically less than 5%), (d) there might exist current leakage channels either through non-perfect insulation layer or lateral electrical conductance on the metasurface. Putting aside improvements in the underlying QC-active material, further improvements in intra-cryostat QC-VECSELs are possible by (a) minimizing any source of loss and channels of current leakage to reduce the threshold current density, (a) improving heat removal via better heat sinking (no substrate thinning has been performed for the current devices), (b) reducing the bias area to reduce the total drive current, (c) reducing the thermal density on the metasurface by designing sparse antenna reflectarrays (such as the patch metasurface design discussed in Sec. 2.5). Even though an excess amount of threshold current density is paid as a cost in the demonstrated intra-cryostat QC-VECSEL, it has achieved significant performance improvement — high pulsed (13 mW) and cw power (5 mW) output in combination with a near-Gaussian beam pattern of $5.3^\circ \times 5.3^\circ$ FWHM divergence. In contrast, the MM waveguide QCL produces a peak pulsed power of 3.6 mW and cw power of 1.6 mW in forms of a divergent beam pattern. The superiority of intra-cryostat QC-VECSEL approach is fully illustrated.

CHAPTER 8

Polarization-switchable metasurface QC-VECSELs

The active metasurface provides a highly flexible platform for integrating new functionality into QC-VECSELs, and this chapter dwells on the integration of polarization switchability. This idea builds on the concept of polarimetric metasurface with engineerable and switchable polarizations; it is further married with the QC-VECSEL scheme, leading to the successful demonstration of QC-VECSEL with electrically-switchable polarization [198]. This chapter provides a comprehensive picture of this work, including the research background, metasurface design, experimental results and analysis.

8.1 Methods of polarization control

The ability to control the polarization state of light from a laser is fundamental, as well as being desirable for a variety of applications, including polarization sensitive imaging, measurements of Faraday rotation, and circular dichroism spectroscopy. Typically, external elements (e.g. polarizers and waveplates) are used to control polarization — less common is the direct switching of the polarization state of the laser itself. Classical methods of changing the polarization direction of lasers generally rely on mechanical means such as movable optics or electromechanical piezo components [199–201], which are bulky and expensive. One

exception is in some VCSELs which exhibit optical bistability and can be switched between nearly degenerate orthogonally polarized modes using injection current [202, 203]. However, since the dependence upon injection current can be hard to predict, injection locking or an adjustable external cavity is often needed to improve stability [204–206]. Meanwhile, several passive metamaterial/metasurface structures have displayed the ability to select a specific circular polarization using chiral plasmonic structures [207, 123, 208]. A compact semiconductor laser with dynamic polarization control capability integrated on chip is desirable, especially in the THz range where many basic optical components are not readily available. There have been several efforts to engineer the polarization of QCLs. In the mid-infrared, plasmonic polarizers have been integrated onto the QCL facet to generate linear or circularly polarized light [209]; in another case a modified ridge waveguide acted as a TM to TE polarization mode converter [210]. In the THz region, circularly polarized emission from a THz QC-laser has been obtained by patterning surface emitting gratings comprising sets of orthogonally oriented slots [211]. However, these are essentially static devices, with the polarization determined at the time of fabrication. To our knowledge, only two examples of dynamic polarization tuning of a QCL have been demonstrated: one instance in which a TE to TM waveguide mode converter was biased to tune linear polarization over 45° [212], and one instance in which two side-by-side and $\sim\pi/2$ phased-shifted QCLs feed surface emitting gratings composed of orthogonally oriented antennas, which demonstrated linear to near-circular polarization tuning controlled by the current injection difference between the two lasers [213]. Nevertheless, dynamic modulation of THz polarization still mostly relies on external modulator elements, such as rotating polarizers/waveplates [214], active THz metamaterials [208, 215], and liquid crystal based waveplates [216, 122], all of which are subject

to insertion loss and modulation speed limits. Photoelastic techniques for rapid polarization modulation are not available at THz frequencies.

Since THz photons are expensive to generate, wasting them in the external elements is unwanted. Ideally it is desirable to build a THz QCL with built-in electrically-switchable polarization, combined with high output power, a single-mode spectrum, and an excellent beam pattern, all of which are nearly unaffected as the polarization is switched.

8.2 Design and modeling of polarimetric metasurface and QC-VECSEL

Aimed at developing a QC-VECSEL that can be electrically switched between two crossed linear polarization states, a polarimetric metasurface is designed based around two interleaved sets of cross-polarized antennas, a concept which has been previously demonstrated in the microwave range using leaky-wave antennas [217]. Fig. 8.1 shows a SEM image of a fabricated polarization-selective metasurface. It is most intuitive to consider each zigzag antenna as a set of patch antennas that couple to the incident electric field polarized along the patch width (13 μm in this case), and are resonant at a frequency that corresponds approximately to when the width is equal to half of the wavelength within the semiconductor. Sets of patches are rotated either at an angle of 45° or 135° from the x-axis; these patches are then connected by narrower segments needed to allow a continuous dc injection current path for each antenna (as seen in Fig. 8.1(a)). Patches of one orientation type are all electrically connected to one wire bonding area and thus can be biased separately from the other

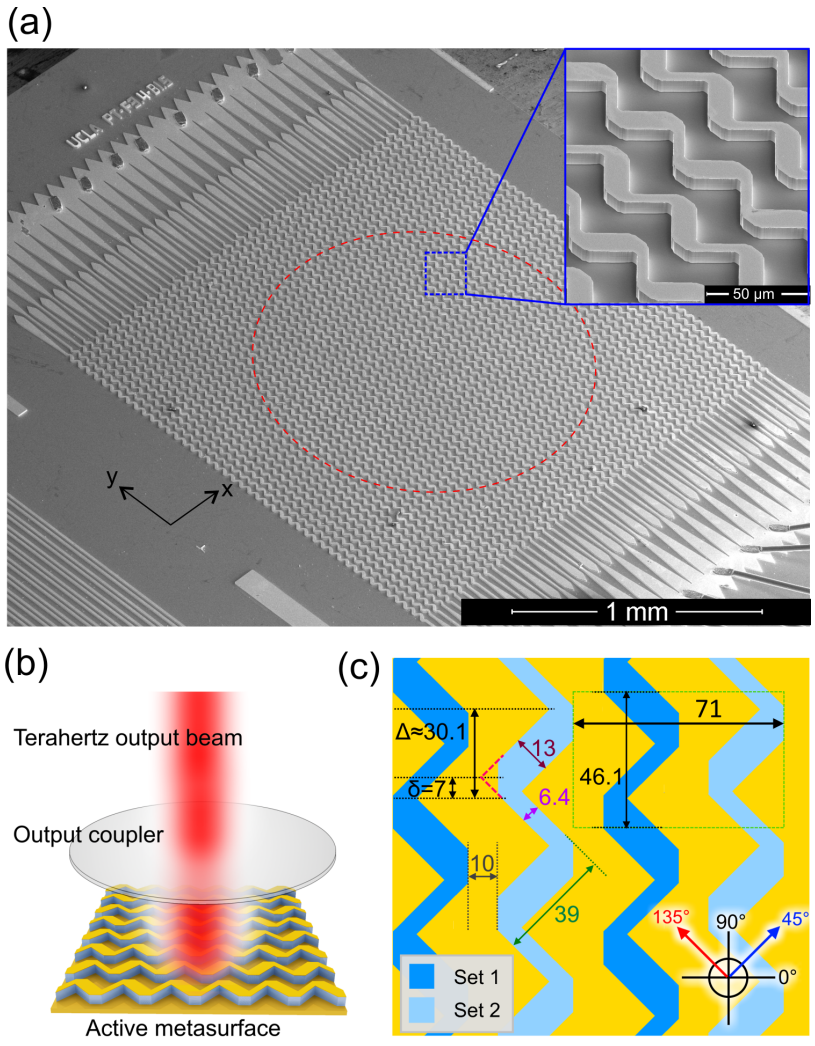

Figure 8.1: (a) An SEM image of the fabricated metasurface. The zigzag metasurface covers an area of 2×2 mm^2. Only a center circular region of 1.5-mm diameter is biased, shown by the red dashed circle. The inset shows a zoom-in SEM image. (b) A schematic of the plano-plano VECSEL cavity. (c) Top view of a portion of the metasurface illustrated with dimensions given in microns. One set of antennas — the ones interacting with radiation linearly polarized at 45° — is shown in dark blue, while the second set of antennas, which interacts with radiation linearly polarized at 135°, is shown in light blue. For brevity, the former set will be referred to as Set 1, while the latter will be referred to as Set 2. The region inside the green dashed rectangle is one unit cell.

type. By switching the electrical bias between the two sets, one can select the polarization preference that the metasurface amplifies and reflects. By pairing such a metasurface with an output coupler that is insensitive to polarization (see Fig. 8.1(b)), a QC-VECSEL with electrically-controlled polarization switching capability is created. Because the cavity mode profile does not depend upon the detailed antenna structure, high power and excellent beam pattern can be consistently maintained as polarization is switched.

The design goal for the metasurface is straightforward: first, when injection current is applied to a single set of antennas we wish to obtain net reflectance gain at a narrow range of frequencies for a single incident polarization (i.e. $|\Gamma_{45^\circ-45^\circ}| > 1$, while $|\Gamma_{135^\circ-135^\circ}| < 1$ when Set 1 is biased and Set 2 is unbiased). Second, to ensure polarization purity, we must suppress cross-polarized scattering at those same frequencies ($|\Gamma_{45^\circ-135^\circ}| \approx |\Gamma_{135^\circ-45^\circ}| \approx 0$). Fig. 8.1(c) shows a top view of the metasurface design and dimensions. Due to their geometry, Set 1 patches (drawn in darker blue) respond to light polarized at 45°, while Set 2 patches respond to light polarized at 135°. These patches, appearing as the thicker portion of the zigzags (13 μm wide), have width of approximately $\lambda/2n$, where λ is the free space wavelength of designed frequency, and n is the index of refraction in the GaAs/AlGaAs quantum-well medium. The period is 71 μm in the horizontal direction and approximately 46.1 μm in the vertical direction (with the exact value being a function of the patch length of 39 μm, the connector width of 6.4 μm, and the right angle they form). The periodicity of the metasurface is chosen to be sufficiently small to avoid Bragg scattering at 3.4 THz for normally incident waves.

While the concept of using rotated sets of patch antennas is straightforward, the detailed

implementation has several subtleties involved with minimizing the effect of the connector segments needed to provide a continuous top metalization, and with preventing cross-coupling between the two sets of antennas. First, cross-polarized scattering is reduced by clipping off the right-angled "elbow" bends along the zigzags, shown as dashed red lines in the upper corner of Fig. 8.1(c). Second, we suppress cross-coupling between adjacent, separately biased antennas by introducing a vertical offset $\Delta \approx 30.1$ μm (with exact value being a sum of the variable $\delta = 7$ μm defined in Fig. 8.1(c) and a geometric constant rounded to 23.1 μm). Zero offset leads to a structure with adjacent ridges being mirror images with respect to the y-axis (i.e. 90° axis shown in Fig. 8.1(c)). The value of the offset and amount of clipping has been optimized by a parametric study of the effect of each parameter on the amount of cross-coupling, using single-cell periodic simulations, with the goal to suppress the unwanted cross-polarized scattering (i.e. ensure $|\Gamma_{45^\circ-135^\circ}| \approx |\Gamma_{135^\circ-45^\circ}| \approx 0$) to ensure the purity of generated linear polarization (see Fig. 8.3).

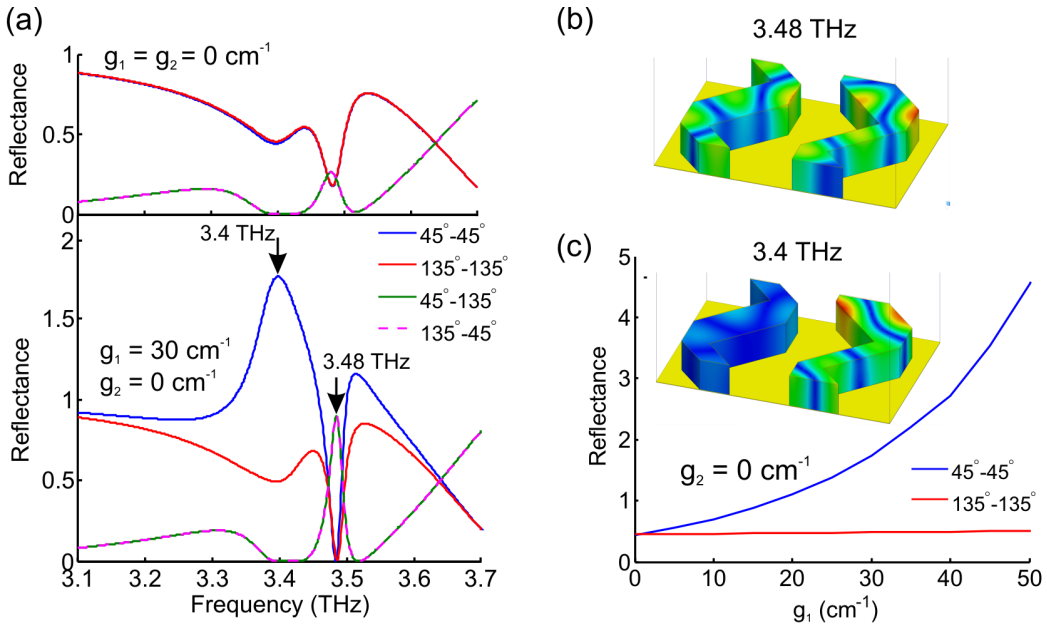

Figure 8.2: (a) Top: Co-polarization and cross-polarization reflectance of the metasurface when Set 1 and Set 2 are both passive. The 45°-45° reflectance $|\Gamma_{45°-45°}|^2$ designates the reflectance of light linearly polarized at 45° (defined according to the coordinates given in Fig. 8.1(c)) into light linearly polarized at 45°, and so on. Bottom: Co-polarization and cross-polarization reflectance of the metasurface when a QC gain of $g_1 = 30$ cm^{-1} is assumed for Set1 patches and Set2 is kept passive. (b) Simulated electric field intensity pattern of a unit cell at 3.48 THz for an incident electric field polarized at 45°. (c) The peak reflectance for 45°-45° and 135°-135° reflectance plotted against the gain g_1 supplied to Set 1 with Set 2 kept passive throughout. Inset is the simulated electric field intensity pattern of a unit cell at 3.4 THz for an incident electric field polarized at 45°.

Modeling was performed using full-wave 3D finite-element simulations (Ansys HFSS), which is done in major collaboration with Daguan Chen, an undergraduate student researcher in our lab. Reflection mode simulations at normal incidence were performed for a unit cell using periodic boundary conditions to simulate infinitely periodic arrays. For clarity, we define gain coefficients g_1 and g_2 to represent the mount of gain supplied to Set 1 and Set 2 patches respectively. Fig. 8.2(a) shows the simulated co- and cross-polarization reflectance $|\Gamma_{ij}|^2$ of the metasurface for two cases: the metasurface is passive ($g_1 = g_2 = 0$) as well as the case where Set 1 patches only are supplied with a gain of $g_1 = 30$ cm^{-1} (emulating

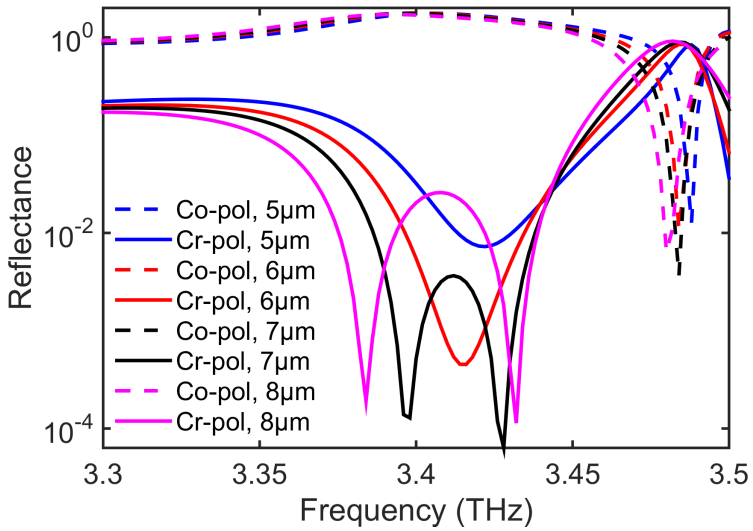

Figure 8.3: Simulated co-polarization reflectance (45°-45°) and cross-polarization reflectance (45°-135°) as the vertical offset (described by variable δ listed in μm) between neighboring patches varies. A gain of $g_1 = 30$ cm^{-1} is supplied to Set 1 patches while Set 2 was kept passive; gain is assumed uniform over the frequency range simulated.

turning on Set 1 patches using bias current) and Set 2 patches kept passive ($g_2 = 0$). When gain is supplied to Set 1 only, net gain is observed for incident E-field polarized at 45° near the target frequency of 3.4 THz, while the orthogonal polarization 135° is almost unchanged compared to the fully passive case. A closer investigation of reflectance change against gain in Set 1 at 3.4 THz confirms the effectiveness of selectively amplifying one specific polarization via the bias switch (see Fig. 8.2(c)); indeed, examination of the E-field profile shows the field mostly localized to the Set 1 antennas. Furthermore, the design shows high effectiveness in suppressing cross-polarization near the target frequency ($|\Gamma_{45°-135°}|^2$ and $|\Gamma_{135°-45°}|^2 < 0.01$ across a bandwidth of 51 GHz). The asymmetric reflectance lineshape is likely a characteristic of Fano resonance owing to the interactions and coupling paths between the complex set of resonances present within the metasurface lattice. One consequence of this is the strong cross-polarized scattering seen at 3.48 THz, particularly when gain is applied

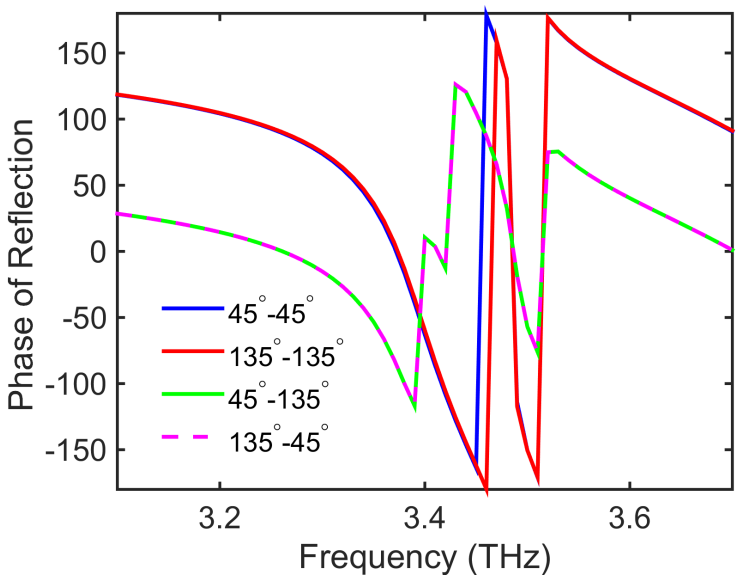

Figure 8.4: Phase of the co-polarized and cross-polarized reflection of the metasurface when a QC gain of $g_1 = 30$ cm^{-1} is assumed for Set 1 patches and Set 2 is kept passive (Phase is wrapped to +180° to -180° range). Gain is assumed uniform over the frequency range simulated. The 45°-45° reflectance designates the reflectance of light linearly polarized at 45° into light linearly polarized at 45°, and so on.

(see Fig. 8.2(b) for the field profile at 3.48 THz).

The expected polarization state of this laser is calculated by applying the polarization repeatability to the cavity round-trip propagation matrix, i.e. $\gamma\vec{E} = \Gamma_{\mathrm{M}}\vec{E}$, where the matrices for the output coupler, free space and the cryostat window are ignored since they have no effect on the polarization. The metasurface field reflection matrix Γ_M is defined as

$$\Gamma_{\mathrm{M}} = \begin{bmatrix} \Gamma_{45^\circ-45^\circ} & \Gamma_{45^\circ-135^\circ} \\ \Gamma_{135^\circ-45^\circ} & \Gamma_{135^\circ-135^\circ} \end{bmatrix} \tag{8.1}$$

and the values are obtained from the simulated complex reflection spectrum (see Fig. 8.4 for simulated reflection phase data). We are able to predict the cavity polarization eigenstate $\vec{E}$ by calculating the eigenvector of Γ_M. γ is the eigenvalue associated with the eigenvec-

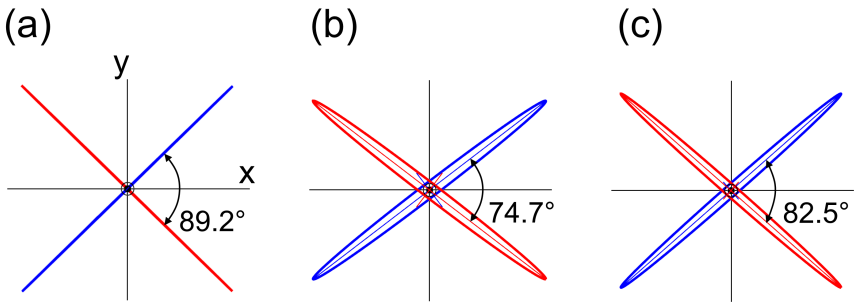

Figure 8.5: (a) Simulated polarization eigenstate ellipses for the output beam when operating at the peak reflectance frequency of 3.397 THz. The two selectable polarization states, shown in blue (Set 1 switched on) and red (Set 2 switched on), differ by a rotation of 89.2° and the intensity axial ratio of the ellipse's major axis to its minor axis is 55 dB for both. The polarization eigenstate ellipse for the output beam when operating at 3.384 THz and 3.41 THz are plotted in (b) and (c). For these calculations, the co-polarized reflectance is held constant at its value at 3.397 THz in order to simulate all three cases with the same lasing threshold, with only the cross-polarized reflectance varied.

tor, representing the reflection amplitude experienced by the solved polarization eigenstate. At the resonant frequency of 3.40 THz, the calculated polarization ellipses exhibits linear polarization with a high electric field intensity axial ratio of 55 dB; furthermore, we expect the two possible bias states to produce beams whose polarization direction is separated by 89.2°, as illustrated in Fig. 8.5(a). However, if the laser is forced to oscillate away from the reflectance peak for any reason, we can expect increased cross-polarized scattering, and decreased orthogonality. This is shown by calculating the expected eigenstate for operating frequencies approximately 13 GHz below and above the resonant frequency in Fig. 8.5(b) and (c); the polarization becomes slightly elliptically polarized, with the intensity axial ratios decreased to 26.2 dB and 28.1 dB respectively, as well as 6°–15° deviation in the angular separation between two bias states.

Similar to the previous metasurface designs, the patch arrays are terminated with lossy tapers to suppress any self-lasing of antenna ridges in propagating mode. Additionally, to

ensure that self-lasing of the antenna sub-cavity doesn't occur before the VECSEL lasing, 3D Floquet-Bloch eigenmode finite-element simulations are performed including both radiative and material losses, to ensure that there were no high quality factor modes close in frequency to the design frequency.

8.3 Experimental results

A resonant phonon depopulation active region design very similar to Ref. [97] around 3.4 THz is used for the polarimetric metasurface (RPC163-M1 design, wafer number VB0739). The demonstrated VECSEL is based on a plano-plano FP cavity defined by the polarimetric metasurface mounted inside a cryostat and an OC in parallel mounted externally. The cavity length is approximately 9 mm. The OC used here is an inductive metal mesh on a 100 μm-thick crystal quartz substrate, whose transmission is approximately 20% around 3.4 THz.

Electrical, power, and spectral characteristics were evaluated for a fixed VECSEL cavity alignment, where Set 1 and Set 2 antennas were switched on one at a time. As shown in Fig. 8.6, pulsed *P-I-V* curves were measured at 77 K for each set with 0.25% overall duty cycle (500 ns-long pulses repeated at 10 kHz, modulated by a 150 Hz pulse train with lock-in detection). The power is measured using a pyroelectric detector and calibrated by a Thomas-Keating THz absolute power meter with 100% collection efficiency (given the directive beam pattern achieved). The measured *P-I-V* curves are very similar for the two sets, both exhibiting a threshold current density of 420 A/cm^2, a slope efficiency of 190 mW/A, and a peak power of $\sim$93 mW. Single-mode lasing operation is observed for both

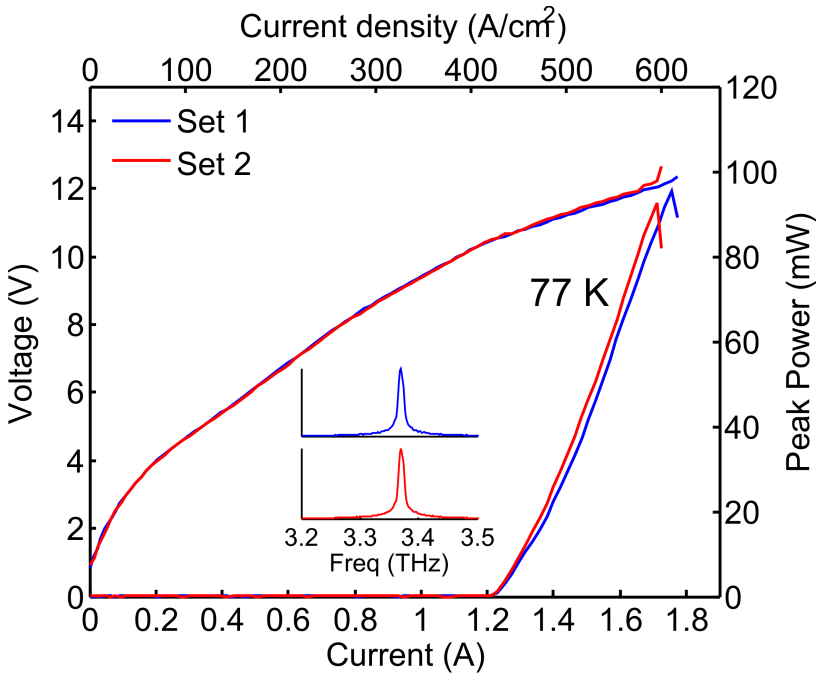

Figure 8.6: Pulsed *P-I-V* curves measured for Set 1 and Set 2 in the same cavity setup at 77 K. The inset is the spectra measured for the two sets.

sets at an identical frequency of 3.37 THz (within the FTIR spectrometer's resolution of 7.5 GHz), which does not change with electrical bias.

To analyze the polarization state of the output, we placed a wire-grid polarizer (Infraspecs model P03) in between the output coupler and the detector, and measured the power as the polarizer is rotated. This measurement was conducted for Set 1 and Set 2 by switching on one set at a time. The results shown in Fig. 8.7(a) demonstrates a polarization switching between linear polarized states separated by 80°. The slight deviation from the ideal value of 90° is likely due to non-ideal cross-polarized scattering from the metasurface, the reasons for which are discussed below. Far-field beam patterns were characterized using a 2-axis spherical scanning pyroelectric detector for Set 1 and Set 2 at the same bias point near the maximum power output. As it can be seen in Fig. 8.7(b)–(e), the measured beams are almost identical as the bias is switched between 2 sets, both exhibiting a directive and narrow

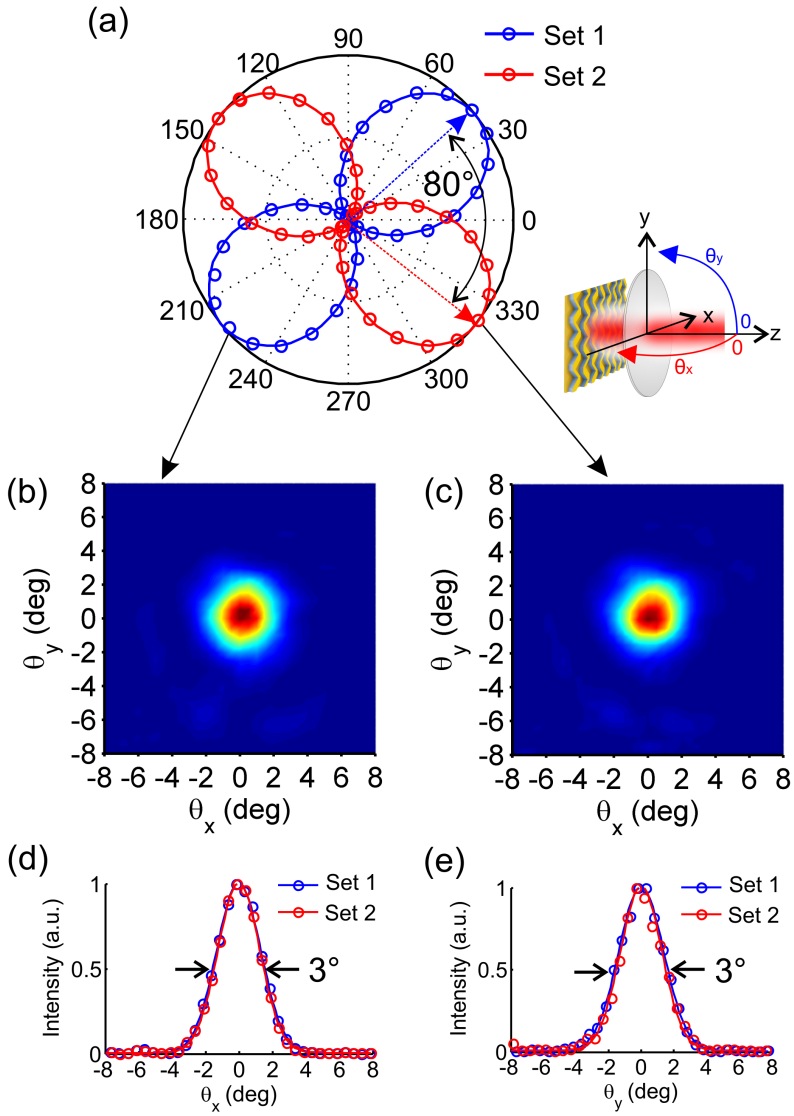

Figure 8.7: (a) Measured total power through the polarizer versus the polarizer angle for two sets. 80° linear polarization angle switching is shown in arrow. Circles are experimental data, and the solid lines in red and blue are the fitting curves (to Eq. 8.2). The schematic on the bottom right of (a) shows the 2-axis far-field beam pattern measurement scheme. The measured 2D beam patterns for Set 1 and Set 2 are shown in (b) and (c), with an angular resolution of 0.5°. The 1D cuts along x and y directions through the beam center for Set 1 and Set 2 are plotted in colored circle in (d) and (e), with the Gaussian curve fitting results plotted in solid colored lines.

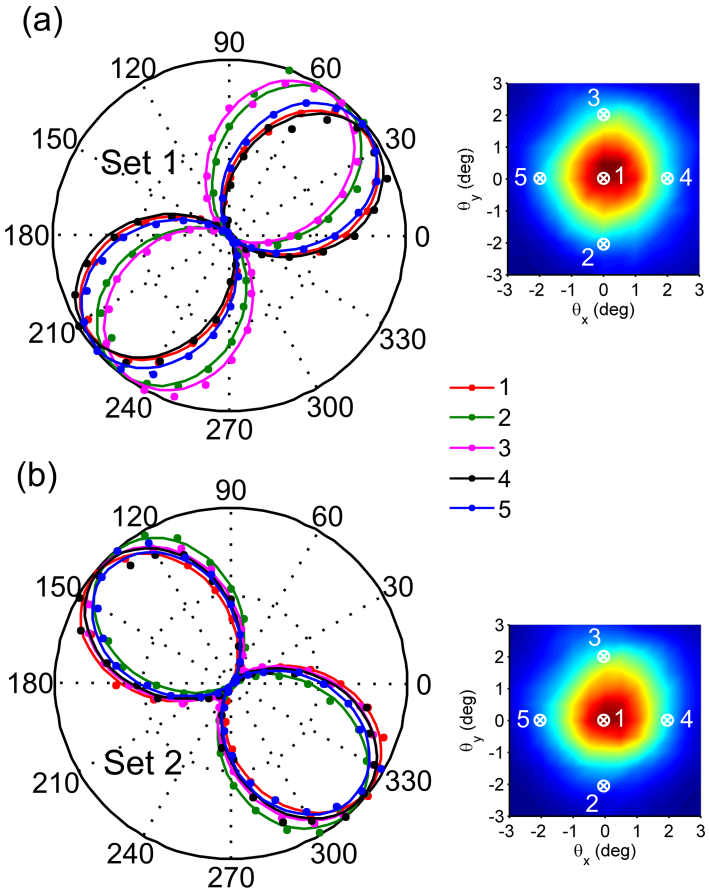

Figure 8.8: Measured power through the polarizer against the polarizer angle at five spots on the output beam for Set 1 (a) and Set 2 (b). Dots are experimental data, and the solid lines in are the fitting curves (to Eq. 8.2).

near-Gaussian pattern with FWHM angular divergence of $\sim 3^\circ \times 3^\circ$. Hence, the electrically-controlled polarization switching is conducted nearly without affecting the output beam, spectrum, or total power.

The uniformity of polarization over the beam was further evaluated by measuring the power vs. polarizer orientation at different beam spots. Fig. 8.8 presents the mapping results at five different beam spots, including one at the center and the other four that are 2° away from the center in four directions. It can be seen that the polarization is very uniform across the x-axis. It is slightly less uniform across the y-axis with a maximum deviation of 22° for

Set 1 and 13° for Set 2 rotated towards the y-axis. We further assessed the linear polarization purity by fitting the power against polarizer angle data to the expression:

$$I = a_0(T_s + T_p) + a_1(T_s - T_p)cos(2\theta_p - 2\varphi) \tag{8.2}$$

where α_0, α_1, and φ are the fitting parameters, and θ_p is the varying angle that the axis of the polarizer makes with respect to the 0° direction. The derivation of this formula is detailed in Appendix C. T_s and T_p are respectively the wire-grid polarizer's transmittance for electric field polarized crossed and parallel to the wires' direction, the values of which in THz range are $T_s = \sim 0.8$ and $T_p = \sim 10^{-4}$. The linear polarization purity is evaluated by the intensity ratio between the dominant polarization and the cross polarization of obtained as $\frac{a_0+a_1}{a_0-a_1}$. This value is ideally infinite for pure linear polarization. The extracted intensity axial ratios for the total beam and five beam spots are listed in Table 8.1, which are all greater than 10 dB. The purity level is lowest at Spot 3 on the beam pattern for both sets, which suggests that the cross-polarized field component induced by the cross-polarized scattering on the metasurface is out-of-phase with the dominant polarized field, leading to slight elliptical polarization. We believe that this moderate amount of polarization non-uniformity, including the linear polarization rotation and slight elliptical polarization, can be attributed to the not fully suppressed cross-polarized reflection on the metasurface. Two major factors could lead to an increased strength of cross-polarization. First, the lasing frequency likely has some deviation from the ideal resonance frequency of the fabricated metasurface. As detailed in Sec. 8.2 above, a slight deviation of the VECSEL lasing frequency away from the designed metasurface resonance frequency of 3.4 THz can result in a slightly elliptically polarized beam

and a deviation of angular separation from the ideal value of 90°. An exact match between is difficult to achieve in experiment, since the lasing frequency is determined by a combination of factors, including the cryostat window's etalon filter effect (with a free spectral range of 13 GHz), the active medium gain profile, and the metasurface resonance peak. The effects of this frequency deviation on cross-polarized scattering may be exacerbated by the fact that the metasurface dimensions are slightly smaller than design (i.e. a 0.5-μm change in the patch width) due to photolithography. Second, enhanced cross-polarized scattering may also result from the obliquely incident field component in the Gaussian cavity mode profile, which was not accounted for in our simulation of normal incidence plane waves.

Table 8.1: Axial ratios of field intensity (in unit of dB) for the total beam and different beam spots from Set 1 and Set 2 patches

	Total beam	**1**	**2**	**3**	**4**	**5**
Set1	16.8	15.4	17.7	12.1	24.5	20.4
Set2	13.8	18.3	30	10.7	15.2	22.9

8.4 Polarimetric metasurface self-lasing

The metasurface QC-VECSEL is designed to operate with only one antenna set switched on at a time. Nonetheless, a natural question arises — what if both antenna sets are switched on together? For example, might one be able to continuously vary the polarization of output state as in the case of passive cross-polarized antennas? Unfortunately the answer is no — due to cross coupling between antennas sets, introduction of gain into both sets significantly changes the reflectance spectrum, and results in lasing at different frequencies than the original design at 3.40 THz. However this behavior is interesting in its own right.

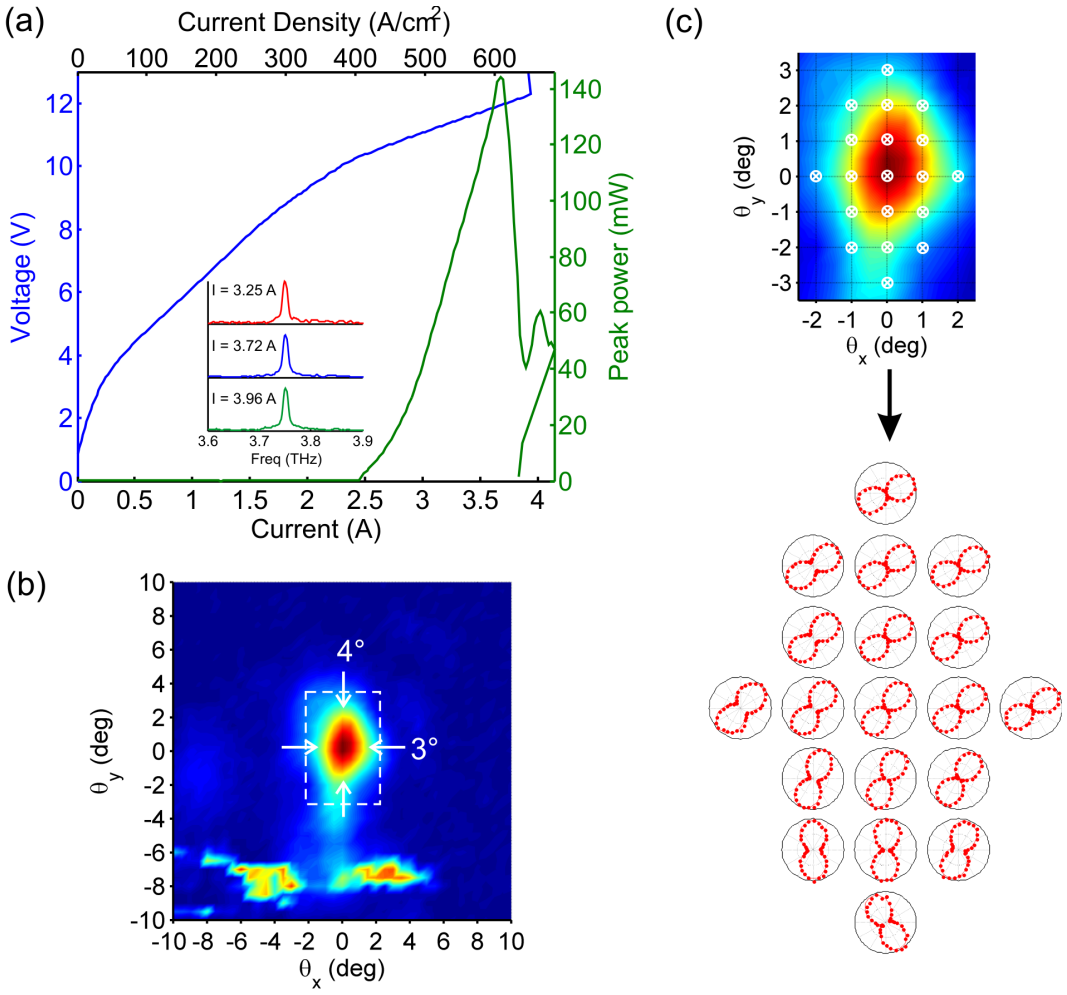

Figure 8.9: (a) Measured P-I-V curve for the polarimetric metasurface without an external cavity. Nominally identical bias is provided to both Set 1 and Set 2. The inset shows the spectra at different injection current levels. (b) Measured far-field beam pattern for the metasurface self-lasing near the peak power, with FWHM divergence angles in x and y direction labeled. The polarization is mapped at different beam spots within the white dashed box. (c) Measured power through the polarizer at different spots on the beam pattern indicated by the circled white cross marks.

In experiment, when both sets of antennas were biased together, we observed self-lasing of the metasurface alone without any OC. The measured *P-I-V* curve and spectra at different biases are shown in Fig. 8.9(a). Single-mode lasing at a frequency of 3.75 THz is observed, and is unchanged with bias within the resolution of FTIR. The power peaks at 144 mW with a slope efficiency estimated at 139 mW/A. The threshold current density is 400 A/cm^2, lower than the threshold for the polarimetric VECSEL, although the larger bias area results in a larger total threshold current. The power output is in the surface normal direction and exhibits a directive and narrow beam of 3°×4° FWHM divergence, as shown in Fig. 8.9(b), which is measured with the metasurface positioned as the origin of the measurement setup as Fig. 8.7(a) shows. Some excess power below the main lobe is observed; it is speculated that this may result from scattering from the wire bonds. The polarization over the output beam is found to be largely linearly over the beam, but with a very non-uniform distribution of polarization direction, as shown in Fig. 8.7(c). We speculate that this behavior is associated with the complex and spatially varying phase relation between the coupled modes in Set 1 and Set 2, along with inhomogeneities in fabrication, structure, and biasing which break the expected symmetry between 45°- and 135°-polarized radiation. This is not fully understood, and will require further detailed simulation and experimental study.

The self-lasing phenomenon is consistent with behavior predicted both by eigenmode type simulations and driven reflection mode simulations if both antenna sets are supplied with the same amount of gain. A low self-lasing threshold of ∼17 cm^{-1} is found lower than the value of 28 cm^{-1} estimated for the polarimetric VECSEL lasing. This self-lasing is attributed to a standing wave mode resonance along the antenna patch length; the mode is "bright" in that

it radiates strongly in the far field with even parity. If only one set is biased, simulations predict that the gain threshold is much larger — approximately 30–35 cm^{-1}.

The self-lasing phenomenon is first observed in the reflectance spectra simulation for both sets supplied with the same amount of gain. As shown in Fig. 8.10, two pronounced peaks show up in the results at 3.48 THz and 3.8 THz. The cross-polarized scattering peak at 3.48 THz is observed when one set is biased (see $g_1 = 30$ cm^{-1} and $g_2 = 0$ cm^{-1}) as shown in Fig. 8.2(b). This peak is further enhanced when both sets are supplied with $30\,\text{cm}^{-1}$ gain, accompanied by a peak in co-polarized reflectance at 3.48 THz. This is attributed to the high-Q resonance associated with the strong coupling between Set 1 and Set 2 when they are supplied with a balanced gain. The other peak at 3.80 THz shows a sharp Fano-type resonance for $g_1 = g_2 = 20$ cm^{-1} in both the co- and cross-polarization reflectance, which suggests it is likely to lase on its own with a threshold gain close to 20 cm^{-1}. The field excited at 3.80 THz is shown in Fig. 8.10.

A series of finite-element eigenmode simulations are performed to identify self-lasing modes and estimate their threshold gain for self-lasing. The purpose is twofold. First, as a design strategy, we wish to ensure that the threshold gain for self-lasing is sufficiently larger so that the external cavity VECSEL mode is preferred for oscillation. Second, we wish to understand the origin of the self-lasing behavior measured at 3.75 THz. The simulations are performed for a metasurface unit cell with an upper impedance boundary condition applied to account for the radiation loss, and periodic Floquet-Bloch boundary conditions used on the sides. Material losses are kept identical to the reflection simulation. Then, the material gain applied to the active material is iteratively increased until the calculated quality factor

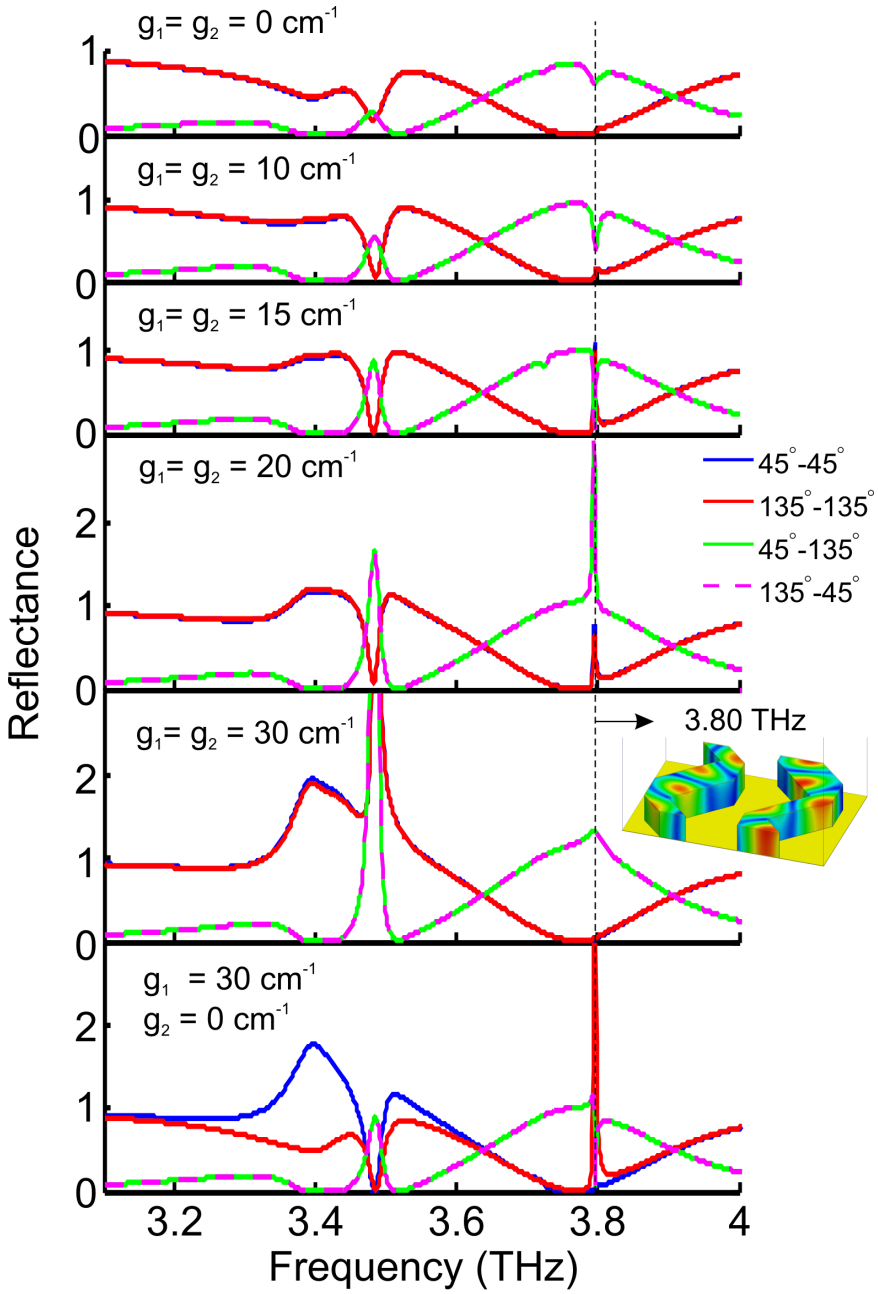

Figure 8.10: Simulated reflectance spectra for both Set 1 and Set 2 supplied with the same amount of gain varied from 0 to 30 cm^{-1}, compared with the reflectance spectrum for Set 1 biased only with 30 cm^{-1} gain in the bottom plot. The inset shows the electric field intensity excited at 3.80 THz.

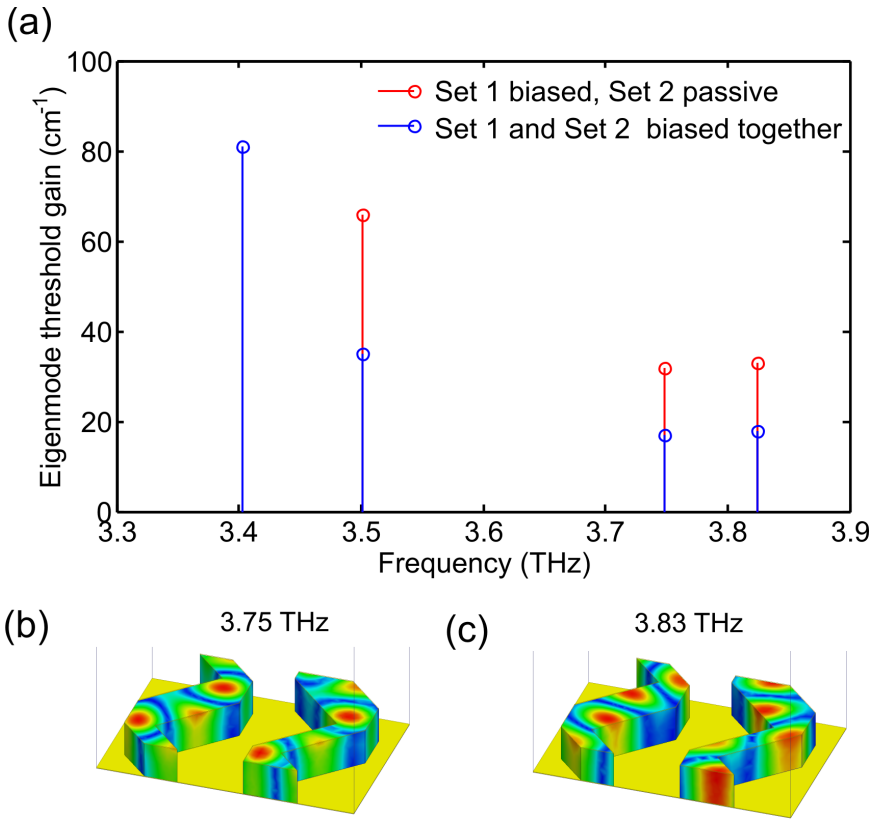

Figure 8.11: (a) Simulated eigenmode frequency and the corresponding lasing threshold gain for two cases: Set 1 and Set 2 are biased together and only Set 1 is biased with Set 2 kept passive. (b) Eigenmode field intensity plot at 3.75 THz for both sets biased. (c) Eigenmode field intensity plot at 3.83 THz for both sets biased.

diverges for a particular mode. The value of material gain is termed the threshold gain value. Two bias scenarios are studied: Set 1 and Set 2 are biased together and supplied with equal gain ($g_1 = g_2 > 0$), and Set 1 is biased only with Set 2 kept passive ($g_1 > 0, g_2 = 0$). Multiple self-lasing eigenmodes are found within 3.3–4 THz range, the frequencies and lasing gain thresholds for which are plotted in Fig. 8.11(a). Although the modes at 3.40 and 3.50 THz are well aligned with the intersubband gain peak, they should have sufficiently large threshold gain so that there is little risk of them self-lasing if an external cavity is present or only one antenna set is biased at a time. This ensures lasing in the polarimetric VECSEL mode as designed. However, when both antenna sets are biased two modes at 3.75 THz and 3.83 THz are estimated to have a very low gain threshold of $\sim$17 cm^{-1}; their field plots are presented in Fig. 8.11(b) and (c). The field profile for 3.83 THz self-lasing mode matches with the field excited in the reflection simulation at 3.80 THz (see Fig. 8.10), which implies that these are in fact the same mode, with the slight frequency mismatch occurring due to differences in the two simulation conditions. The fact that it is observed in reflectance indicates that this is a bright mode which strongly couples to free space radiation. The other self-lasing mode at 3.75 THz is not observed in the reflectance simulation; it appears to be a dark mode with radiation to free space forbidden by parity. This is further confirmed by a lossless eigenmode simulation where all material losses are eliminated so that radiation is the only loss channel. This simulation shows a diverging radiative quality factor (i.e. a vanishing radiation loss) for the 3.75 THz eigenmode, but not for the 3.83 THz eigenmode. Therefore we attribute the experimentally measured self-lasing at 3.75 THz to be the same as the lasing in the 3.83 THz bright eigenmode (i.e. the 3.80 THz mode in reflectance). The frequency mismatch is likely caused by the fabrication deviation and nonuniformity. Another

factor to this mismatch is that the eigenmode simulation is for a unit cell in a periodical boundary condition to depict an infinite structure, while the actual self-lasing occurs in a finite structure containing a limited number of unit cells and terminated by lossy boundaries (i.e. lossy taper areas).

This self-lasing phenomenon can be considered to be an unintentional realization of a laser array phase-locked through mutual antenna coupling, similar to that reported in Ref. [95]. The self-lasing mode relies on strong coupling between sets of antennas, as is revealed by the strong cross-polarized scattering shown in simulation results at 3.80 THz, and the fact that the gain threshold is much higher when only one set of antennas is biased (see Fig. 8.10 and 8.11). The fact that such a narrow far-field beam was obtained indicates that phase-locking is obtained over the entire 1.5-mm diameter bias area (19 wavelengths), which encompasses ∼1080 patch elements. The performance of this self-lasing phenomenon could be further improved, if the metasurface was designed by intention to bring the self-lasing frequency down to better match the QC material optimal gain region of 3.3–3.5 THz.

CHAPTER 9

Conclusion and future work

In this thesis, I have described the development of terahertz metasurface quantum cascade vertical-external-cavity surface emitting lasers (QC-VECSELs). The research conducted over the course of this thesis spans the design, optimization and fabrication of metasurface, development of QC-VECSEL laser model, numerical modeling of VECSEL cavities, experimental demonstration and testing results. A variety of metasurfaces and VECSEL cavities have been designed, modeled and experimentally implemented, leading to a wealth of high-performance demonstrations with high power and high-quality beam patterns combined. Novel metasurface designs have also been exploited to integrate new functionality into QC-VECSELs, proving the potential of leveraging advanced metasurfaces to further advance QC-VECSELs.

Some of the major accomplishments and experimental observations that contributed to our understanding of QC-VECSEL and the general research community include the following. The performances of a few state-of-the-art QC-VECSELs are listed in Table 9.1 in comparison with the best performances reported from other THz QCLs.

- The demonstration of metasurface THz QC-VECSEL marks the first successful implementation of VECSEL scheme in the THz range. It exhibits considerable power

output, low-divergence near-Gaussian beam pattern, and tunable output coupling efficiency. The primary enabling component is the active metasurface reflector that makes the"intersubband selection rule" in QC materials satisfied. The QC-VECSEL not only inherits a host of merits known for VECSELs in visible and near-infrared, but also enables new features and potential contributed by the flexible metasurface design.

- The metasurface resonance primarily relies on the locally self-resonant microcavities, rather than the periodicity-dependent grating mode, which in fact suppresses the desired specular reflection. The reflection spectroscopy measurement and simulation of multiple passive metasurfaces reveals that it is critical to choose an appropriate value for periodicity Λ to fully suppress the grating-mode excitation on a metasurface for a finite-size beam. To balance against the desire to keep a low thermal density, it is advisable to have the periodicity $\Lambda \sim 0.7$–$0.8\lambda_0$, where λ_0 is the free-space wavelength of interest.

- The optimization of metasurface is theoretically studied based on the laser model developed for QC-VECSELs. Setting the QC active material improvement aside, the output power at the optimal output coupling point is optimizable with the transparency gain g_{tr} and fitting coefficient ξ — two parameters characterizing a metasurface design. It is found that this optimization depends on the external cavity loss — generally a lossier cavity prefers a higher ξ.

- Focusing metasurface QC-VECSELs have been demonstrated with higher geometric cavity stability and better beam quality, compared with its counterpart based on the uniform metasurface. Near-diffraction limited beams are exhibited with the M^2 factor

measured as low as 1.3, which is the best reported M^2 factor directly from a THz QCL based on MM waveguide with no spatial filtering. The focusing design is particularly useful for external cavities with long cavity lengths, as long as the cavity length is kept smaller than the effective curvature radius.

- Intra-cryostat metasurface QC-VECSELs have led to some of the best power output and cw operation at >77 K, combined with a near-Gaussian beam. It is learned that a sufficiently low consumption of total power is critical to cw operation at >77 K. This has been achieved by reducing the bias area diameter on metasurfaces from 1 mm to 0.7 mm to keep the total injected power below 5 W. Compared with its external cavity counterparts, the intra-cryostat cavity shows lower threshold current density with higher power output, thanks to the removal of cryostat window and atmospheric loss, as well as reduced diffraction loss. The demonstrated high-performance intra-cyostat QC-VECSELs are highly preferable for many applications such as local oscillator for THz heterodyne detection.

- A QC-VECSEL with electrically-switchable polarization has been demonstrated based on a polarimetric metasurface, the power and beam pattern of which are consistently maintained as the polarized is switched. It exemplifies the potential of exploiting novel metasurface designs to empower QC-VECSEL with new functionality, while preserving its high performance. Besides, the self-lasing is observed from the polarimetric metasurface alone, which results from the complex antenna mutual-coupling between neighboring patches. This is in itself an interesting phenomenon worth further studying.

Despite a number of high-performance demonstrations, the development of QC-VECSELs is still in the early stage. It sits at the intersection of VECSEL, metasurface, and QCL technologies, thus calling for multidisciplinary knowledge and experience to bring QC-VECSELs towards the next level. Immediate future work aimed at high performance and new functionality include but not limited to the following.

- Towards higher performance in cw operation at >77 K
  - Use sparse patch array metasurface designs to further reduce the power consumption and thermal density.
  - Thin the metasurface substrate and use better heat sinking to improve thermal dissipation efficiency.
  - Evaporate a layer of Au on the Cu ground to minimize the excess loss due to rough and oxidized Cu surface.
- Towards high pulsed power >500 mW
  - Enlarge TM_{01} metasurface area or use TM_{03} metasurface designs with a higher current injection density to scale up the power.
  - Design focusing metasurfaces with large effective curvature radius to obtain a large modal size on the metasurface with a large bias area, i.e. to keep a high uniformity factor η_u.
  - Use the appropriate output coupler to reach the optimal output coupling point.
- Reflection spectroscopy study of active metasurface

  This study necessitates the development of a THz time-domain spectroscopy (THz-

TDS) system to conduct coherent measurement of amplified reflectance from metasurfaces. Phase response is also extractable from THz-TDS measurement. Direct measurement of reflective amplification and phase response will provide valuable information on the interplay between the QC material gain profile and metasurface resonance, and sheds light upon new designs.

- Generation of vector beams

  Since microcavity antennas on the metasurface have a strong polarization dependence, their spatial distribution can be deliberately designed to preferentially provide gain to a cavity mode with a specific polarization state, such as vector beams with azimuthal or radial polarization [218]. Radially-polarized beams are of particular interest as they can be focused to smaller spot size than for linear polarization and exhibit a purely longitudinal E-field at the focal point [219, 220].

- Generation of vortex beams

  Vortex beams with Orbital Angular Momentum (OAM) have been directly generated from the optically-pumped VECSEL in near-infrared, enabled by integrating a metasurface with azimuthally-varying phase onto the gain mirror [165]. It is anticipated that QC-VECSELs based on a metasurface with azimuthally-varying phase response are also promising to directly generate THz vortex beams. Overall, the key task is to design the metasurfaces that have azimuthally-varying phase responses as desired, appropriate bias lines connecting all the elements, and self-lasing effectively suppressed. Besides, given a larger modal size associated vector and vortex beams than TEM_{00} Gaussian mode, the metasurface size needs to be enlarged and a focusing design might

be beneficial.

- Broadband metasurface

  The metasurfaces demonstrated so far in this work use an array of metal-metal microcavities with one microcavity assigned to one period, the bandwidth of which is limited within 100–200 GHz. Broadband metasurfaces are of interest in realizing QC-VECSELs with frequency tunability, multi-longitudinal-mode lasing, and frequency combs generation. The last feature also needs a flat group velocity dispersion from metasurface over the bandwidth or external dispersion compensation elements. Coupled resonances from multiple microcavities can be explored to produce a broadband response.

- Multi-beams and arbitrary beam generation

  Although QC-VECSELs are mostly designed to support fundamental TEM_{00} Gaussian mode, it is also possible to incorporate inhomogeneous metasurfaces and adapt cavity designs to generate higher-order Hermite-Gaussian modes. Their multi-beams output is useful to pump a THz heterodyne detector array of many elements, which is highly desired in astrophysics. Hologram metasurface concepts can also be integrated with QC-VECSELs to explore the possibility of arbitrary beam generation.

- Pancharatnam-Berry metasurface

  Metasurfaces based on Pancharatnam-Berry (PB) phase has been a heated research topic recently. It has demonstrated a broad bandwidth and the capability of manipulating phase and polarization simultaneously. It offers another degree of freedom in metasurface designs. Potentials exist in integrating the PB metasurface with QC

materials to devise active PB metasurfaces that can selectively amplify a wavefront with polarization and phase as designed over a large bandwidth and in developing PB metasurface QC-VECSELs with new functionalities such as circularly-polarized light generation.

Table 9.1: State-of-the-art QC-VECSELs in comparison with the performance records from other THz QCLs reported. η_{slp} is the slope efficiency. WPE is the wall-plug efficiency. $\star$ Data is not measured. $\star\star$ No lasing is observed. $\star\star\star$ Beam pattern does not appear near-Gaussian and circular. $*$ The external cavity QC-VECSEL is based on a focusing metasurface with $R = 10$ mm and the output coupler is mounted external to the cryostat. $**$ 1 mm and 0.7 mm refer to the diameter of the circular bias area on the metasurface.

Performance	External cavity QC-VECSEL $*$	Intra-cryostat QC-VECSEL (1 mm$**$)	Intra-cryostat QC-VECSEL (0.7 mm$**$)	Record performance
Beam pattern	$\mathbf{3.5}^\circ \times \mathbf{3.6}^\circ$ $M^2 = 1.3$	$4.9^\circ \times 4.3^\circ$	$5.3^\circ \times 5.3^\circ$	$4^\circ \times 4^\circ$ [91] $\star\star\star$
$P_{pulsed,77K}$	46 mW	140 mW	13 mW	**1.8 W** [74]
$P_{pulsed,4K}$	78 mW	$\star$	19 mW	**2.4 W** [74]
$P_{cw,77K}$	$\star\star$	$\star\star$	**5 mW**	1.7 mW [85]
$P_{cw,4K}$	40 mW	$\star$	14 mW	**230 mW** [221]
$\eta_{slp,pulsed,77K}$	413 mW/A	**745 mW/A**	95 mW/A	700 mW/A [72]
$\eta_{slp,pulsed,6K}$	572 mW/A	$\star$	131 mW/A	**900 mW/A** [72]
$\eta_{slp,cw,77K}$	$\star\star$	$\star\star$	**53 mW/A**	28 mW/A [78]
$\eta_{slp,cw,4K}$	339 mW/A	$\star$	92 mW/A	**678 mW/A** [72]
$\text{WPE}_{pulsed,4K}$	1.15%	1.5% (77 K)	0.5%	**2.7%** [222]
$\text{WPE}_{cw,4K}$	0.6%	$\star$	0.3%	**2.05%** [72]
$T_{max,pulsed}$	$\star$	$\star$	129 K	**200 K** [75]
$T_{max,cw}$	$\star$	$\star$	$\star$	**129 K** [78]

APPENDIX A

Drude expression for metal and QC active material

A.1 Bulk Drude expression

The bulk Drude model is used to describe the free carrier scattering loss in the metal and semiconductor material in metasurface simulations, which leads to the following expression of frequency-dependent permittivity ϵ

$$\epsilon = \epsilon_{core} + i\frac{\sigma(\omega)}{\omega}, \tag{A.1}$$

where ϵ_{core} is the core permittivity excluding the free carrier contributions. The frequency-dependent conductivity $\sigma(\omega)$ is derived from the Drude model that depicts an electron placed in a driving field $\mathbf{E}(t) = Re(\mathbf{E}(\omega)e^{-i\omega t})$ and given by

$$\sigma(\omega) = \frac{Ne^2\tau}{m^*}\frac{1}{1 - i\omega\tau}, \tag{A.2}$$

where N represents the free carrier density in the bulk material, m^* is the effective carrier mass, e is the carrier's charge, and τ is the free carrier effect lifetime. The values of N, τ, m^*, and ϵ_{core} for Au and GaAs used in the simulation are given in Table 2.1.

A.2 Anisotropic expression of permittivity for QC material with gain

Even though the QC quantum-well material is in fact an anisotropic material system, for simplicity the loss inside the active region is generally considered using the bulk Drude model, where an average carrier density and the corresponding bulk mobility are used. This consideration excludes the complexity arising from the carrier confinement along the material growth direction, which effectively shifts the oscillator frequency from zero to various intersubband transition frequencies, each weighted by their oscillator strength [1]. Considering that the confinement effect might be mitigated by small oscillator strength and equalization of subband population and its description involves many uncertainties such as intersubband transition lifetime, it is reasonable to approximate free carrier loss in the QC active material with the bulk Drude model.

However, for QC active material with a nonzero mount of gain g this confinement effect should be accounted for due to the enhanced stimulated emission. Since the intersubband gain only interacts with the electric field polarized along the growth direction, the bulk Drude expression $\epsilon(\omega)$ needs to be expanded into an anisotropic tensor expression to incorporate the gain properly, as given by

$$\bar{\bar{\epsilon}}(\omega) = \begin{bmatrix} \epsilon_{GaAs} & 0 & 0 \\ 0 & \epsilon_{GaAs} & 0 \\ 0 & 0 & \epsilon_{GaAs} + i\epsilon_g(\omega) \end{bmatrix}, \tag{A.3}$$

where the growth direction is assumed long the z direction, ϵ_{GaAs} is obtained from the bulk Drude model using Eq. A.1 and A.2, and $\epsilon_g(\omega) = \frac{g\sqrt{\epsilon_r}c}{\omega}$. $\epsilon_r = 12.9$ is the relative permittivity for GaAs and c is the speed of light in vacuum.

APPENDIX B

Metasurface fabrication procedures and recipes

- Cu-Cu thermocompression wafer bonding

    1. Deposit Ta (30 nm, 1 Å/s)/Cu (300 nm, 3 Å/s) on top of the highly-doped GaAs receiving wafer and QCL wafer (Perform buffer oxide etch (BOE) dip to remove any native oxide on the surface right before the metal evaporation).
    2. Perform wafer bonding using Karl Suss bonder.
    3. Perform annealing process using Karl Suss bonder.

- Substrate removal

    1. Deposit ∼300 nm SiO_2 to protect the back side of GaAs receiving wafer.
    2. Mechanically lap the GaAs substrate on the QCL wafer side till its thickness is a little below 50 nm.
    3. Remove the remaining GaAs till the etch stop layer is reached using PA wet etching, i.e. an Ammonium hydroxide and hydrogen peroxide solution (NH_4OH:H_2O_2 = 1:25).
    4. Remove the etch stop layer using hydrofluoric acid (HF) etching.

5. Remove the highly-doped GaAs layer by diluted PA etching (NH_4OH:H_2O_2:H_2O = 5:3:240).

- Insulation layer deposition and patterning

1. Deposit ∼200 nm high-quality SiO_2 on top. A test run on a dummy wafer is suggested.
2. Pattern AZ5214 positive photoresist mask
   (a) Pre-bake at 150 °C for 5 mins.
   (b) Soak in HMDS vapor chamber for 8 mins.
   (c) Spin coat AZ5412 at 500/100 RPM for 5 s, 3000/1000 RPM for 30 s.
   (d) Soft-bake at 110 °C for 1 min.
   (e) Perform photolithography at 8 W for 9 s.
   (f) Develop with the solution of AZ400K:H_2O = 1:4.
   (g) Hard-bake at 150 °C for 2 mins.
3. Perform BOE wet etching to remove SiO_2 area not covered by the positive photoresist. Check SiO_2 thickness to make sure it is all removed.
4. Remove the remaining photoresist mask using acetone.

- Metal mask and Au contact evaporation and patterning

1. Pattern NLOF2020 negative photoresist mask
   (a) Pre-bake at 150 °C for 2 mins.
   (b) Soak in HDMS vapor chamber for 8 mins.

(c) Spin coat NLOF2020 at 500/250 RPM for 6 s, 750/250 RPM for 6s, 2000/250 RPM for 30 s.

(d) Soft-bake at 110 °C for 1 min.

(e) Perform photolithography at 8 W for 8.5 s.

(f) Post-exposure bake at 110 °C for 1 min.

(g) Develop with AZ300 MIF.

2. Evaporate Ti (15 nm, 1 Å/s)/Au (250 nm, 3 Å/s)/Ni (200 nm, 3 Å/s).

3. Perform metal lift-off.

- Metal-metal ridge definition by ICP-RIE dry etching

1. Run O_2 cleaning recipe for 30 mins.

2. Stick the sample wafer on a Si wafer with $\sim$ 2 μm SiO_2 on top with thermal grease.

3. Run ATGAAS recipe (BCl_3 flow rate = 50, Cl_2 flow rate = 3, N_2 flow rate = 3) on the sample. The etch rate is about 0.5 μm/min. Closely watch the sample while etching and stop it once the copper ground plane gets exposed.

4. Remove Ni layer by Nickel etcher.

- Backside metal contact evaporation Evaporate Cr (20 nm, 1 Å/s)/Au (250 nm, 3 Å/s) on the sample backside. (Do a quick BOE dip right before the metal evaporation).

APPENDIX C

Linear polarization evaluation: axial ratio

Let's assume that the output field takes the form of elliptical polarization, which allows us to represent the laser output field in a linear polarization basis by $\langle L \mid E_o \rangle = \begin{pmatrix} |E_x| \\ |E_y|\, e^{i\phi} \end{pmatrix}$. The x and y axes of the linear basis are respectively aligned with the 0° and 90° direction defined in Fig. 8.1(c). The Jones matrix for a wire-grid polarizer with the wire direction rotated by an angle of θ_p from x-axis is given by $\langle L|P(\theta_p)|L\rangle = \langle L|R(-\theta_p)|L\rangle \begin{pmatrix} T_p & 0 \\ 0 & T_s \end{pmatrix} \langle L|R(\theta_p)|L\rangle$, where $\langle L|R(\theta_p)|L\rangle = \begin{pmatrix} \cos\theta_p & \sin\theta_p \\ -\sin\theta_p & \cos\theta_p \end{pmatrix}$ is the corresponding rotation matrix. T_t and T_p are the wire-grid polarizer transmittance for electrical field polarized transverse and parallel to the wires direction. The relative power received by the detector is therefore given by

$$
\begin{aligned}
I &= \left| \langle L|R(-\theta_p)|L\rangle \begin{pmatrix} T_p & 0 \\ 0 & T_s \end{pmatrix} \langle L|R(\theta_p)|L\rangle \langle L \mid E_o\rangle \right|^2 \\
&= a_0(T_s + T_p) + a_1(T_s - T_p)\cos(2\theta_p - 2\varphi)
\end{aligned}
\tag{C.1}
$$

where $a_0 = \frac{1}{2}\left(|E_x|^2 + |E_y|^2\right)$,$a_1 = \sqrt{\frac{1}{4}\left(|E_x|^2 - |E_y|^2\right)^2 + |E_x|^2\,|E_y|^2\cos^2\phi}$, and φ is the angle that the dominant polarization direction rotates from the y-axis. The intensity axial ratio

measured with an ideal polarizer ($T_t = 1$ and $T_p = 0$) is given by the ratio of maximum and minimum of the above formula, i.e. $\frac{a_0+a_1}{a_0-a_1}$. This ratio is employed in the Sec. 8.3 to describe the linear polarization purity. The nonideality of actual polarizer used is accounted for by plugging in $T_s = \sim 0.8$ and $T_p = \sim 10^{-4}$ in Eq. C.1. It can be seen that when $\phi = 0^{\circ}$ or 180°, which represents a purely linear polarization with E-field components in x- and y-axis in-phase , the obtained axial ratio $\frac{a_0+a_1}{a_0-a_1}$ is infinite.

APPENDIX D

Laser power calibration

The detector used for power-current-voltage (P-I-V) curve measurement in this work is a pyroelectric detector purchased from Gentec (QS9-THZ-BL). The active detection area is 9×9 mm^2. Given the narrow and directive beam pattern from QC-VECSEL devices, this detection area is large enough to capture all the power with a collection efficiency of 100%.

An intra-cryostat QC-VECSEL lasing at 3.45 THz is used to calibrate the pyroelectric detector's responsivity. The device is operated at a fixed bias point throughout the calibration. First, the device is driven by continuous voltage pulses with repetition rate of f_0 (Hz) and pulse width of w_0 (s). The power is measured by a thermopile detector (Scientec AC2500), where reads P_0 (W). The thermopile accuracy has been validated by a Thomas-Keating detector. So the absolute peak power of this device is

$$P_{peak} = \frac{P_0}{f_0 \times w_0}. \tag{D.1}$$

Second, the device is driven by a voltage pulse train composed of continuous pulses with f_{pyro} (Hz) repetition rate and w_{pyro} (s) pulse width, modulated by a square wave of f_t (Hz). The modulation frequency f_t is kept between 5–200 Hz to ensure a considerable response of

the pyroelectric detector. The voltage output V_{pyro} from the pyroelectric detector is given by

$$V_{pyro} = R_v(f_t) \times f_{pyro} \times w_{pyro} \times P_{peak} \tag{D.2}$$

where R_v (V/W) is the responsivity of the pyroelectric detector to be calibrated. It depends on the modulation frequency f_t. Combining Eq. D.1 and Eq. D.2, we obtain the calibration result for R_v at the chopping frequency f_t as

$$R_v(f_t) = \frac{V_{pyro} \times f_0 \times w_0}{P_0 \times f_{pyro} \times w_{pyro}}. \tag{D.3}$$

For example, following this approach we calibrated the responsivity for the pyroelectric detector at a pulse modulation frequency of $f_t = 150$ Hz, which gives $R_v(150\,\mathrm{Hz}) = 1.2 \times 10^3$ V/W.

For pulsed-mode measurement, the peak power of QC-VECSEL driven by a pulse train with repetition rate of f (Hz), pulse width of w (s), and modulation frequency of 150 Hz can be obtained as $\frac{V_{pyro}}{R_v(150\,\mathrm{Hz}) \times f \times w}$. For cw-mode measurement, the absolute output power is directly calibrated by the thermopile.

References

[1] B. S. Williams, *Terahertz quantum cascade laser*. PhD thesis, Massachusetts Institute of Technology, 2003.

[2] S. Kumar, *Development of terahertz quantum-cascade lasers*. PhD thesis, Massachusetts Institute of Technology, 2007.

[3] B. S. Williams, "Terahertz quantum-cascade lasers," *Nat. Photon.*, vol. 1, no. 9, pp. 517–525, 2007.

[4] O. G. Okhotnikov, ed., *Semiconductor Disk Lasers: Physics and Technology*. Wiley, 2010.

[5] C. L. Holloway, E. F. Kuester, J. a. Gordon, J. O'Hara, J. Booth, and D. R. Smith, "An overview of the theory and applications of metasurfaces: The two-dimensional equivalents of metamaterials," *IEEE Antennas Propag. Mag.*, vol. 54, no. 2, pp. 10–35, 2012.

[6] C. Walker, C. Kulesa, J. Kloosterman, D. Lesser, T. Cottam, C. Groppi, J. Zmuidzinas, M. Edgar, S. Radford, P. Goldsmith, W. Langer, H. Yorke, J. Kawamura, I. Mehdi, D. Hollenbach, J. Stutzki, H. Huebers, J. R. Gao, and C. Martin, "Large format heterodyne arrays for observing far-infrared lines with SOFIA," in *SPIE Astron. Telesc. + Instrum.* (W. S. Holland and J. Zmuidzinas, eds.), pp. 77410Z–77410Z–6, International Society for Optics and Photonics, 2010.

[7] P. H. Siegel, "Terahertz technology," *IEEE Trans. Microw. Theory Tech.*, vol. 50, p. 910, 2002.

[8] D. T. Leisawitz, W. C. Danchi, M. J. DiPirro, L. D. Feinberg, D. Y. Gezari, M. Hagopian, W. D. Langer, J. C. Mather, S. H. Moseley, Jr., M. Shao, R. F. Silverberg, J. G. Staguhn, M. R. Swain, H. W. Yorke, and X. Zhang, "Scientific motivation and technology requirements for the SPIRIT and SPECS far-infraredisubmillimeter space interferometers," *UV, Opt. IR Sp. Telesc. Instruments*, vol. 4013, pp. 36–46, 2000.

[9] C. Kulesa, "Terahertz spectroscopy for astronomy: From comets to cosmology," *IEEE Trans. Terahertz Sci. Technol.*, vol. 1, no. 1, pp. 232–240, 2011.

[10] H. Richter, M. Wienold, L. Schrottke, K. Biermann, H. T. Grahn, and H.-w. Hübers, "4.7-THz Local Oscillator for the GREAT Heterodyne Spectrometer on SOFIA," *IEEE Trans. Terahertz Sci. Technol.*, vol. 5, no. 4, pp. 539–545, 2015.

[11] G. L. Pilbratt, J. R. Riedinger, T. Passvogel, G. Crone, D. Doyle, U. Gageur, A. M. Heras, C. Jewell, L. Metcalfe, S. Ott, and M. Schmidt, "Herschel Space Observatory - An ESA facility for far-infrared and submillimetre astronomy," *Astron. Astrophys.*, vol. 518, p. L1, 2010.

[12] E. T. Young, E. E. Becklin, P. M. Marcum, T. L. Roellig, J. M. De Buizer, T. L. Herter, R. Güsten, E. W. Dunham, P. Temi, B.-G. Andersson, D. Backman, M. Burgdorf, L. J. Caroff, S. C. Casey, J. A. Davidson, E. F. Erickson, R. D. Gehrz, D. A. Harper, P. M. Harvey, L. A. Helton, S. D. Horner, C. D. Howard, R. Klein, A. Krabbe, I. S. McLean,

A. W. Meyer, J. W. Miles, M. R. Morris, W. T. Reach, J. Rho, M. J. Richter, H.-P. Roeser, G. Sandell, R. Sankrit, M. L. Savage, E. C. Smith, R. Y. Shuping, W. D. Vacca, J. E. Vaillancourt, J. Wolf, and H. Zinnecker, "Early science with SOFIA, the stratospheric observatory for infared astronomy," *Astrophys. J.*, vol. 749, no. 2, p. L17, 2012.

[13] E. R. Mueller, R. Henschke, W. E. Robotham, Jr., L. a. Newman, L. M. Laughman, R. a. Hart, J. Kennedy, and H. M. Pickett, "Terahertz local oscillator for the Microwave Limb Sounder on the Aura satellite," *Appl. Opt.*, vol. 46, no. 22, p. 4907, 2007.

[14] H.-B. Liu, H. Zhong, N. Karpowicz, Y. Chen, and X.-C. Zhang, "Terahertz Spectroscopy and Imaging for Defense and Security Applications," *Proc. IEEE*, vol. 95, no. 8, pp. 1514–1527, 2007.

[15] P. Dean, M. U. Shaukat, S. P. Khanna, S. Chakraborty, M. Lachab, A. Burnett, G. Davies, and E. H. Linfield, "Absorption-sensitive diffuse reflection imaging of concealed powders using a terahertz quantum cascade laser," *Opt. Express*, vol. 16, no. 9, p. 5997, 2008.

[16] Y. C. Shen, T. Lo, P. F. Taday, B. E. Cole, W. R. Tribe, and M. C. Kemp, "Detection and identification of explosives using terahertz pulsed spectroscopic imaging," *Appl. Phys. Lett.*, vol. 86, no. 24, p. 241116, 2005.

[17] C. A. Schmuttenmaer, "Exploring dynamics in the far-infrared with terahertz spectroscopy," *Chem. Rev.*, vol. 104, no. 4, pp. 1759–1779, 2004.

[18] D. Burghoff, T.-Y. Kao, N. Han, C. W. I. Chan, X. Cai, Y. Yang, D. J. Hayton, J.-R.

Gao, J. L. Reno, and Q. Hu, "Terahertz laser frequency combs," *Nat. Photon.*, vol. 8, no. 6, pp. 462–467, 2014.

[19] Y. Yang, D. Burghoff, D. J. Hayton, J.-R. Gao, J. L. Reno, and Q. Hu, "Terahertz multiheterodyne spectroscopy using laser frequency combs," *Optica*, vol. 3, no. 5, p. 499, 2016.

[20] Z. D. Taylor, R. S. Singh, D. B. Bennett, P. Tewari, C. P. Kealey, N. Bajwa, M. O. Culjat, A. Stojadinovic, H. Lee, J. P. Hubschman, E. R. Brown, and W. S. Grundfest, "THz medical imaging: In vivo hydration sensing," *IEEE Trans. Terahertz Sci. Technol.*, vol. 1, no. 1, pp. 201–219, 2011.

[21] J. P. Dougherty, G. D. Jubic, W. L. Kiser, Jr., and W. L. Kiser Jr., "Terahertz imaging of burned tissue," in *Proc. SPIE 6472*, vol. 6472, p. 64720N, International Society for Optics and Photonics, 2007.

[22] D. B. Bennett, Z. D. Taylor, P. Tewari, R. S. Singh, M. O. Culjat, W. S. Grundfest, D. J. Sassoon, R. D. Johnson, J.-P. Hubschman, and E. R. Brown, "Terahertz sensing in corneal tissues," *J. Biomed. Opt.*, vol. 16, no. 5, p. 57003, 2011.

[23] R. M. Woodward, V. P. Wallace, R. J. Pye, B. E. Cole, D. D. Arnone, E. H. Linfield, and M. Pepper, "Terahertz pulse imaging of ex vivo basal cell carcinoma," *J. Invest. Dermatol.*, vol. 120, no. 1, pp. 72–78, 2003.

[24] Y. B. Ji, E. S. Lee, S.-H. Kim, J.-H. Son, and T.-I. Jeon, "A miniaturized fiber-coupled terahertz endoscope system.," *Opt. Express*, vol. 17, no. 19, pp. 17082–17087, 2009.

[25] A. J. Fitzgerald, B. E. Cole, and P. F. Taday, "Nondestructive Analysis of Tablet Coating Thicknesses Using Terahertz Pulsed Imaging," *J. Pharm. Sci.*, vol. 94, no. 1, pp. 177–183, 2005.

[26] C. P. Chiou, R. B. Thompson, W. P. Winfree, E. I. Madaras, and J. Seebo, "Modeling and processing of terahertz imaging in space shuttle external tank foam inspection," in *AIP Conf. Proc.*, 2006.

[27] C. Stoik, M. Bohn, and J. Blackshire, "Nondestructive evaluation of aircraft composites using reflective terahertz time domain spectroscopy," *NDT E Int.*, vol. 43, no. 2, pp. 106–115, 2010.

[28] G. C. Walker, J. W. Bowen, W. Matthews, S. Roychowdhury, J. Labaune, G. Mourou, M. Menu, I. Hodder, and J. B. Jackson, "Sub-surface terahertz imaging through uneven surfaces: visualizing Neolithic wall paintings in {Ç}atalh{ö}y{ü}k," *Opt. Express*, vol. 21, no. 7, p. 8126, 2013.

[29] T. Nagatsuma, G. Ducournau, and C. C. Renaud, "Advances in terahertz communications accelerated by photonics," *Nat. Publ. Gr.*, vol. 10, 2016.

[30] J. Ma, F. Vorrius, L. Lamb, L. Moeller, and J. F. Federici, "Experimental Comparison of Terahertz and Infrared Signaling in Laboratory-Controlled Rain," *J. Infrared, Millimeter, Terahertz Waves*, vol. 36, no. 9, pp. 856–865, 2015.

[31] "R P.840-6: Attenuation due to Clouds and Fog," tech. rep., International Telecommunication Union ITU, 2013.

[32] M. A. Khalighi and M. Uysal, "Survey on Free Space Optical Communication: A Communication Theory Perspective," *IEEE Commun. Surv. & Tutorials*, vol. 16, no. 4, pp. 2231–2258, 2014.

[33] D. L. Woolard, E. R. Brown, M. Pepper, and M. Kemp, "Terahertz frequency sensing and imaging: A time of reckoning future applications?," *Proc. IEEE*, vol. 93, no. 10, pp. 1722–1743, 2005.

[34] E. Wasige, K. H. Alharbi, A. Al-Khalidi, J. Wang, A. Khalid, G. C. Rodrigues, and J. Figueiredo, "Resonant tunnelling diode terahertz sources for broadband wireless communications," *Proc. SPIE*, vol. 10103, p. 101031J, 2017.

[35] A. Khalid, G. M. Dunn, R. F. Macpherson, S. Thoms, D. Macintyre, C. Li, M. J. Steer, V. Papageorgiou, I. G. Thayne, M. Kuball, C. H. Oxley, M. Montes Bajo, A. Stephen, J. Glover, and D. R. S. Cumming, "Terahertz oscillations in an $In_{0.53}Ga_{0.47}As$ submicron planar Gunn diode," *J. Appl. Phys.*, vol. 115, no. 11, p. 114502, 2014.

[36] K. Higuchi, H. Matsumoto, T. Mishima, H. Zhong Yinghui, W. Xiantai, S. Yongbo, A. Endoh, Y. Yamashita, K. Shinohara, J.-C. Huang, W.-C. Hsu, C.-S. Lee, B.-H. Lee, S.-D. Kim, J.-K. Rhee, T. Takahashi, Y. Kawano, K. Makiyama, S. Shiba, M. Sato, Y. Nakasha, and N. Hara, "Maximum frequency of oscillation of 1.3 THz obtained by using an extended drain-side recess structure in 75-nm-gate InAlAs/InGaAs high-electron-mobility transistors," *Appl. Phys. Express*, vol. 10, 2017.

[37] A. Maestrini, B. Thomas, H. Wang, C. Jung, J. Treuttel, Y. Jin, G. Chattopadhyay,

I. Mehdi, and G. Beaudin, "Schottky diode-based terahertz frequency multipliers and mixers Multiplicateurs," *Comptes Rendus Phys.*, vol. 11, no. 7-8, pp. 480–495, 2010.

[38] X. Mei, W. Yoshida, M. Lange, J. Lee, J. Zhou, P. H. Liu, K. Leong, A. Zamora, J. Padilla, S. Sarkozy, R. Lai, and W. R. Deal, "First Demonstration of Amplification at 1 THz Using 25-nm InP High Electron Mobility Transistor Process," *IEEE Electron Device Lett.*, vol. 36, no. 4, pp. 327–329, 2015.

[39] N. M. Burford and M. O. El-Shenawee, "Review of terahertz photoconductive antenna technology," *Opt. Eng.*, vol. 56, no. 1, p. 10901, 2017.

[40] N. T. Yardimci, S.-H. Yang, C. W. Berry, and M. Jarrahi, "High-Power Terahertz Generation Using Large-Area Plasmonic Photoconductive Emitters," *IEEE Trans. Terahertz Sci. Technol.*, vol. 5, no. 2, pp. 223–229, 2015.

[41] S.-H. Yang and M. Jarrahi, "Frequency-tunable continuous-wave terahertz sources based on GaAs plasmonic photomixers," *Appl. Phys. Lett.*, vol. 107, no. 13, p. 131111, 2015.

[42] C. W. Berry, M. R. Hashemi, S. Preu, H. Lu, A. C. Gossard, and M. Jarrahi, "High power terahertz generation from ErAs: InGaAs plasmonic photomixers," *Int. Conf. Infrared, Millimeter, Terahertz Waves, IRMMW-THz*, vol. 011121, no. 2014, pp. 10–14, 2014.

[43] M. Shalaby, C. P. Hauri, X.-C. Zhang, F. Ardana1, and A. M. Rappe, "Demonstration of a low-frequency three-dimensional terahertz bullet with extreme brightness," *Nat. Commun.*, vol. 6, p. 5976, 2015.

[44] C. Vicario, B. Monoszlai, and C. P. Hauri, "GV/ m single-cycle terahertz fields from a laser-driven large-size partitioned organic crystal," *Phys. Rev. Lett.*, vol. 112, no. 21, pp. 1–5, 2014.

[45] M. A. Belkin, F. Capasso, F. Xie, A. Belyanin, M. Fischer, A. Wittmann, and J. Faist, "Room temperature terahertz quantum cascade laser source based on intracavity difference-frequency generation," *Appl. Phys. Lett.*, vol. 92, no. 20, pp. 1–3, 2008.

[46] S. Jung, A. Jiang, Y. Jiang, K. Vijayraghavan, X. Wang, M. Troccoli, and M. A. Belkin, "Broadly tunable monolithic room-temperature terahertz quantum cascade laser sources.," *Nat. Commun.*, vol. 5, no. May, p. 4267, 2014.

[47] Q. Y. Lu, S. Slivken, N. Bandyopadhyay, Y. Bai, and M. Razeghi, "Widely tunable room temperature semiconductor terahertz source," *Appl. Phys. Lett.*, vol. 105, no. 20, p. 201102, 2014.

[48] Y. Jiang, K. Vijayraghavan, S. Jung, F. Demmerle, G. Boehm, M. C. Amann, and M. A. Belkin, "External cavity terahertz quantum cascade laser sources based on intra-cavity frequency mixing with 1.2–5.9 THz tuning range," *J. Opt.*, vol. 16, no. 9, p. 094002, 2014.

[49] M. Razeghi, Q. Y. Lu, N. Bandyopadhyay, W. Zhou, D. Heydari, Y. Bai, and S. Slivken, "Quantum cascade lasers: from tool to product," *Opt. Express*, vol. 23, no. 7, pp. 8462–8475, 2015.

[50] T. Y. Chang and T. J. Bridges, "Laser action at 452, 496, and 541 μm in optically pumped CH_3F," *Opt. Commun.*, vol. 1, no. 9, pp. 423–426, 1970.

[51] M. Inguscio, G. Moruzzi, K. M. Evenson, and D. A. Jennings, "A review of frequency measurements of optically pumped lasers from 0.1 to 8 THz," *J. Appl. Phys.*, vol. 60, no. 12, pp. R161–R192, 1986.

[52] G. L. Carr, M. C. Martin, W. R. McKinney, K. Jordan, G. R. Neil, and G. P. Williams, "High-power terahertz radiation from relativistic electrons," *Nature*, vol. 420, no. 6912, pp. 153–156, 2002.

[53] P. Tan, J. Huang, K. Liu, Y. Xiong, and M. Fan, "Terahertz radiation sources based on free electron lasers and their applications," *Sci. China Inf. Sci.*, vol. 55, no. 1, pp. 1–15, 2012.

[54] E. Gornik and A. A. Andronov, "Far-infrared semiconductor lasers," *Opt. Quantum Electron.*, vol. 23, no. 2, pp. v–v, 1991.

[55] S. G. Pavlov, R. K. Zhukavin, E. E. Orlova, V. N. Shastin, A. V. Kirsanov, H.-W. Hübers, K. Auen, and H. Riemann, "Stimulated Emission from Donor Transitions in Silicon," *Phys. Rev. Lett.*, vol. 84, no. 22, pp. 5220–5223, 2000.

[56] H.-W. Hübers, S. G. Pavlov, and V. N. Shastin, "Terahertz lasers based on germanium and silicon," *Semicond. Sci. Technol.*, vol. 20, no. 7, pp. S211–S221, 2005.

[57] Y. P. Gousev, I. V. Altukhov, K. A. Korolev, V. P. Sinis, M. S. Kagan, E. E. Haller, M. A. Odnoblyudov, I. N. Yassievich, and K. A. Chao, "Widely tunable continuous-wave THz laser," *Appl. Phys. Lett.*, vol. 75, no. 6, p. 757, 1999.

[58] L. Li, I. Kundu, P. Dean, E. H. Linfield, and A. G. Davies, "High-power GaAs/AlGaAs

quantum cascade lasers with emission in the frequency range 4.75.6 THz," in *Int. Quantum Cascade Lasers School and Workshop*, 2016.

[59] R. Köhler, A. Tredicucci, F. Beltram, H. E. Beere, E. H. Linfield, a. G. Davies, D. a. Ritchie, R. C. Iotti, and F. Rossi, "Terahertz semiconductor-heterostructure laser.," *Nature*, vol. 417, no. 6885, pp. 156–159, 2002.

[60] R. F. Kazarinov and R. A. Suris, "Possibility of the Amplification of Electromagnetic Waves in a Semiconductor with a Superlattice," *Sov. PhysicsSemiconductors*, vol. 5, no. 4, p. 707, 1971.

[61] J. Faist, F. Capasso, D. L. Sivco, C. Sirtori, A. L. Hutchinson, and A. Y. Cho, "Quantum Cascade Laser," *Science*, vol. 264, no. 5158, pp. 553–556, 1994.

[62] Y. Yao, A. J. Hoffman, and C. F. Gmachl, "Mid-infrared quantum cascade lasers," *Nat. Photon.*, vol. 6, no. 7, pp. 432–439, 2012.

[63] F. Capasso, "High-performance midinfrared quantum cascade lasers," *Opt. Eng.*, vol. 49, no. 11, p. 111102, 2010.

[64] M. Rochat, L. Ajili, H. Willenberg, J. Faist, H. Beere, G. Davies, E. Linfield, and D. Ritchie, "Low-threshold terahertz quantum-cascade lasers," *Appl. Phys. Lett.*, vol. 81, no. 8, pp. 1381–1383, 2002.

[65] B. Williams, H. Callebaut, S. Kumar, Q. Hu, and J. Reno, "3.4 THz quantum cascade laser based on longitudinal-optical-phonon scattering for depopulation," *Appl. Phys. Lett.*, vol. 82, no. 7, p. 1015, 2003.

[66] B. S. Williams, S. Kumar, H. Callebaut, Q. Hu, and J. L. Reno, "3.4THz quantum cascade laser operating above liquid nitrogen temperature," *Electron. Lett.*, vol. 39, no. 12, pp. 915–916, 2003.

[67] G. Scalari, L. Ajili, J. Faist, H. Beere, E. Linfield, D. Ritchie, and G. Davies, "Far-infrared ($\lambda \sim$87 μm) bound-to-continuum quantum-cascade lasers operating up to 90 K," *Appl. Phys. Lett.*, vol. 82, no. 3165, pp. 3165–3167, 2003.

[68] S. Kumar, Q. Hu, and J. L. Reno, "186 K operation of terahertz quantum-cascade lasers based on a diagonal design," *Appl. Phys. Lett.*, vol. 94, no. 13, 2009.

[69] S. Kumar, C. W. I. Chan, Q. Hu, and J. L. Reno, "Two-well terahertz quantum-cascade laser with direct intrawell-phonon depopulation," *Appl. Phys. Lett.*, vol. 95, no. 14, 2009.

[70] G. Scalari, N. Hoyler, M. Giovannini, and J. Faist, "Terahertz bound-to-continuum quantum-cascade lasers based on optical-phonon scattering extraction," *Appl. Phys. Lett.*, vol. 86, no. 18, pp. 1–3, 2005.

[71] M. I. Amanti, G. Scalari, R. Terazzi, M. Fischer, M. Beck, J. Faist, A. Rudra, P. Gallo, and E. Kapon, "Bound-to-continuum terahertz quantum cascade laser with a single-quantum-well phonon extraction/injection stage," *New J. Phys.*, vol. 11, 2009.

[72] Y.-Y. Li, J.-Q. Liu, F.-Q. Liu, J.-C. Zhang, S.-Q. Zhai, N. Zhuo, L.-J. Wang, S.-M. Liu, and Z.-G. Wang, "High power-efficiency terahertz quantum cascade laser," *Chinese Phys. B*, vol. 25, no. 8, p. 084206, 2016.

[73] B. S. Williams, S. Kumar, Q. Hu, and J. L. Reno, "High-power terahertz quantum-cascade lasers," *Electron. Lett.*, vol. 42, no. 2, pp. 18–19, 2006.

[74] L. Li, L. Chen, J. Freeman, M. Salih, P. Dean, A. Davies, and E. Linfield, "Multi-Watt high-power THz frequency quantum cascade lasers," *Electron. Lett.*, pp. 10–11, 2017.

[75] S. Fathololoumi, E. Dupont, C. W. I. Chan, Z. R. Wasilewski, S. R. Laframboise, D. Ban, A. Mátyás, C. Jirauschek, Q. Hu, and H. C. Liu, "Terahertz quantum cascade lasers operating up to 200 K with optimized oscillator strength and improved injection tunneling.," *Opt. Express*, vol. 20, no. 4, pp. 3866–76, 2012.

[76] B. S. Williams, S. Kumar, Q. Hu, and J. L. Reno, "Operation of terahertz quantum-cascade lasers at 164 K in pulsed mode and at 117 K in continuous-wave mode," *Opt. Express*, vol. 13, p. 3331, 2005.

[77] S. Kumar, Q. Hu, and J. L. Reno, "186 K operation of terahertz quantum-cascade lasers based on a diagonal design," *Appl. Phys. Lett.*, vol. 94, no. 13, 2009.

[78] M. Wienold, B. Röben, L. Schrottke, R. Sharma, A. Tahraoui, K. Biermann, and H. T. Grahn, "High-temperature, continuous-wave operation of terahertz quantum-cascade lasers with metal-metal waveguides and third-order distributed feedback," *Opt. Express*, vol. 22, no. 3, p. 3334, 2014.

[79] K. Unterrainer, R. Colombelli, C. Gmachl, F. Capasso, H. Y. Hwang, A. M. Sergent, D. L. Sivco, and A. Y. Cho, "Quantum cascade lasers with double metal-semiconductor waveguide resonators," *Appl. Phys. Lett.*, vol. 80, no. 17, pp. 3060–3062, 2002.

[80] M. S. Vitiello, G. Scalari, B. Williams, and P. D. Natale, "Quantum cascade lasers: 20 years of challenges," *Opt. Express*, vol. 23, no. 4, pp. 5167–5182, 2015.

[81] H. Hirayama, W. Terashima, T.-T. Lin, and M. Sasaki, "Recent progress and future prospects of THz quantum-cascade lasers," in *Proc. SPIE* (A. A. Belyanin and P. M. Smowton, eds.), vol. 9382, pp. 938211–938217, International Society for Optics and Photonics, mar 2015.

[82] B. A. Burnett and B. S. Williams, "Design strategy for terahertz quantum dot cascade lasers," *Opt. Express*, vol. 24, no. 22, p. 25471, 2016.

[83] M. Brandstetter, C. Deutsch, M. Krall, H. Detz, D. C. MacFarland, T. Zederbauer, A. M. Andrews, W. Schrenk, G. Strasser, and K. Unterrainer, "High power terahertz quantum cascade lasers with symmetric wafer bonded active regions," *Appl. Phys. Lett.*, vol. 103, no. 17, p. 171113, 2013.

[84] M. I. Amanti, G. Scalari, F. Castellano, M. Beck, and J. Faist, "Low divergence Terahertz photonic-wire laser.," *Opt. Express*, vol. 18, no. 6, pp. 6390–6395, 2010.

[85] G. Xu, R. Colombelli, S. P. Khanna, A. Belarouci, X. Letartre, L. Li, E. H. Linfield, A. G. Davies, H. E. Beere, and D. A. Ritchie, "Efficient power extraction in surface-emitting semiconductor lasers using graded photonic heterostructures.," *Nat. Commun.*, vol. 3, p. 952, 2012.

[86] A. J. L. Adam, I. Kasalynas, J. N. Hovenier, T. O. Klaassen, J. R. Gao, E. E. Orlova, B. S. Williams, S. Kumar, Q. Hu, and J. L. Reno, "Beam patterns of terahertz quantum

cascade lasers with subwavelength cavity dimensions," *Appl. Phys. Lett.*, vol. 88, no. 15, p. 151105, 2006.

[87] E. Bründermann, M. Havenith, G. Scalari, M. Giovannini, J. Faist, J. Kunsch, L. Mechold, and M. Abraham, "Turn-key compact high temperature terahertz quantum cascade lasers: imaging and room temperature detection.," *Opt. Express*, vol. 14, no. 5, pp. 1829–1841, 2006.

[88] A. W. M. Lee, Q. Qin, S. Kumar, B. S. Williams, Q. Hu, and J. L. Reno, "High-power and high-temperature THz quantum-cascade lasers based on lens-coupled metal metal waveguides," *Opt. Lett.*, vol. 32, no. 19, pp. 2840–2842, 2007.

[89] T.-Y. Kao, Q. Hu, and J. L. Reno, "Perfectly phase-matched third-order distributed feedback terahertz quantum-cascade lasers," *Opt. Lett.*, vol. 37, pp. 2070–2072, 2012.

[90] M. I. Amanti, M. Fischer, G. Scalari, M. Beck, and J. Faist, "Low-divergence single-mode terahertz quantum cascade laser," *Nat. Photon.*, vol. 3, no. 10, pp. 586–590, 2009.

[91] C. Wu, S. Khanal, J. L. Reno, and S. Kumar, "Terahertz plasmonic laser radiating in an ultra-narrow beam," *Optica*, vol. 3, no. 7, pp. 734–740, 2016.

[92] S. Kumar, B. S. Williams, Q. Qin, A. W. Lee, Q. Hu, and J. L. Reno, "Surface-emitting distributed feedback terahertz quantum-cascade lasers in metal-metal waveguides," *Opt. Express*, vol. 15, no. 1, p. 113, 2007.

[93] T.-Y. Kao, Q. Hu, and J. L. Reno, "Phase-locked arrays of surface-emitting terahertz quantum-cascade lasers," *Appl. Phys. Lett.*, vol. 96, no. 10, p. 101106, 2010.

[94] Y. Chassagneux, R. Colombelli, W. Maineult, S. Barbieri, S. P. Khanna, E. H. Linfield, and a. G. Davies, "Graded photonic crystal terahertz quantum cascade lasers," *Appl. Phys. Lett.*, vol. 96, no. 3, p. 031104, 2010.

[95] T.-Y. Kao, J. L. Reno, and Q. Hu, "Phase-locked laser arrays through global antenna mutual coupling," *Nat. Photon.*, vol. 10, no. 8, pp. 541–546, 2016.

[96] Y. Halioua, G. Xu, S. Moumdji, L. Li, J. Zhu, E. H. Linfield, A. Davies, H. E. Beere, D. a. Ritchie, and R. Colombelli, "Phase-locked arrays of surface-emitting graded-photonic-heterostructure terahertz semiconductor lasers," *Opt. Express*, vol. 23, no. 5, p. 6915, 2015.

[97] L. Li, L. Chen, J. Zhu, J. Freeman, P. Dean, A. Valavanis, A. G. Davies, and E. H. Linfield, "Terahertz quantum cascade lasers with >1 W output powers," *Electron. Lett.*, vol. 50, no. 4, pp. 309–311, 2014.

[98] A. J. Kemp, A. J. MacLean, J. E. Hastie, S. A. Smith, J. M. Hopkins, S. Calvez, G. J. Valentine, M. D. Dawson, and D. Burns, "Thermal lensing, thermal management and transverse mode control in microchip VECSELs," *Appl. Phys. B Lasers Opt.*, vol. 83, no. 2, pp. 189–194, 2006.

[99] M. Kuznetsov, F. Hakimi, R. Sprague, and A. Mooradian, "High-power (>0.5-W CW) diode-pumped vertical-external-cavity surface-emitting semiconductor lasers with circular TEM_{00} beams," *IEEE Photon. Tech. Lett.*, vol. 9, pp. 1063–1065, 1997.

[100] B. Heinen, T.-L. Wang, M. Sparenberg, a. Weber, B. Kunert, J. Hader, S. W. Koch, J. V. Moloney, M. Koch, and W. Stolz, "106 W continuous-wave output power from

vertical-external-cavity surface-emitting laser," *Electron. Lett.*, vol. 48, no. 9, p. 516, 2012.

[101] F. Zhang, B. Heinen, M. Wichmann, C. Möller, B. Kunert, A. Rahimi-Iman, W. Stolz, and M. Koch, "A 23-watt single-frequency vertical-external-cavity surface-emitting laser," *Opt. Express*, vol. 22, no. 11, p. 12817, 2014.

[102] K. G. Wilcox, A. C. Tropper, H. E. Beere, D. A. Ritchie, B. Heinen, and W. Stolz, "4.35 kW peak power femtosecond pulse mode- locked VECSEL for supercontinuum generation," *Opt. Express*, vol. 21, no. 2, pp. 1599–1605, 2013.

[103] M. Mangold, V. J. Wittwer, C. A. Zaugg, S. M. Link, M. Golling, B. W. Tilma, and U. Keller, "Femtosecond pulses from a modelocked integrated external-cavity surface emitting laser (MIXSEL)," *Opt. Express*, vol. 21, no. 21, pp. 24904–24911, 2013.

[104] A. Bousseksou, M. El Kurdi, M. Salik, I. Sagnes, and S. Bouchoule, "Wavelength tunable InP-based EP-VECSEL operating at room temperature and in CW at 1.55 μm," *Electron. Lett.*, vol. 40, no. 23, p. 1490, 2004.

[105] M. ElKurdi, S. Bouchoule, A. Bousseksou, I. Sagnes, A. Plais, M. Strassner, C. Symonds, A. Garnache, and J. Jacquet, "Room-temperature continuous-wave laser operation of electrically-pumped 1.55 μm VECSEL," *Electron. Lett.*, vol. 40, no. 11, p. 671, 2004.

[106] H.-T. Chen, A. J. Taylor, and N. Yu, "A review of metasurfaces: physics and applications," *Reports Prog. Phys.*, vol. 79, no. 7, p. 76401, 2016.

[107] N. Yu, P. Genevet, F. Aieta, M. A. Kats, R. Blanchard, G. Aoust, J. P. Tetienne, Z. Gaburro, and F. Capasso, "Flat Optics: Controlling Wavefronts With Optical Antenna Metasurfaces," *IEEE J. Sel. Top. Quantum Electron.*, vol. 19, no. 3, p. 4700423, 2013.

[108] N. Yu and F. Capasso, "Flat optics with designer metasurfaces," *Nat. Mater.*, vol. 13, no. 2, pp. 139–150, 2014.

[109] N. Yu, J. Fan, Q. J. Wang, C. Pflügl, L. Diehl, T. Edamura, M. Yamanishi, H. Kan, and F. Capasso, "Small-divergence semiconductor lasers by plasmonic collimation," *Nat. Photon.*, vol. 2, no. 9, pp. 564–570, 2008.

[110] N. Yu, Q. J. Wang, M. A. Kats, J. A. Fan, S. P. Khanna, L. Li, A. G. Davies, E. H. Linfield, and F. Capasso, "Designer spoof surface plasmon structures collimate terahertz laser beams.," *Nat. Mater.*, vol. 9, pp. 730–5, 2010.

[111] G. Liang, E. Dupont, S. Fathololoumi, Z. R. Wasilewski, D. Ban, H. K. Liang, Y. Zhang, S. F. Yu, L. H. Li, A. G. Davies, E. H. Linfield, H. C. Liu, and Q. J. Wang, "Planar integrated metasurfaces for highly-collimated terahertz quantum cascade lasers," *Sci. Rep.*, vol. 4, p. 7083, 2014.

[112] N. Yu, P. Genevet, M. A. Kats, F. Aieta, J.-P. Tetienne, F. Capasso, and Z. Gaburro, "Light propagation with phase discontinuities: generalized laws of reflection and refraction.," *Science*, vol. 334, no. 6054, pp. 333–7, 2011.

[113] S. Sun, K.-Y. Yang, C.-M. Wang, T.-K. Juan, W. T. Chen, C. Y. Liao, Q. He, S. Xiao, W.-T. Kung, G.-Y. Guo, L. Zhou, and D. P. Tsai, "High-E ffi ciency Broadband

Anomalous Re fl ection by Gradient Meta- Surfaces," *Nano Lett.*, vol. 12, pp. 6223–6229, 2012.

[114] F. Aieta, A. Kabiri, P. Genevet, N. Yu, M. A. Kats, Z. Gaburro, and F. Capasso, "Out-of-Plane Reflection and refraction of light from metasurfaces with phase discontinuities," *J. Nanophotonics*, vol. 6, no. 1, p. 063532, 2012.

[115] L. Huang, X. Chen, H. Mühlenbernd, G. Li, B. Bai, Q. Tan, G. Jin, T. Zentgraf, and S. Zhang, "Dispersionless Phase Discontinuities for Controlling Light Propagation," *Nano Lett.*, vol. 12, no. 11, pp. 5750–5755, 2012.

[116] P. Genevet, N. Yu, F. Aieta, J. Lin, M. A. Kats, R. Blanchard, M. O. Scully, Z. Gaburro, and F. Capasso, "Ultra-thin plasmonic optical vortex plate based on phase discontinuities," *Appl. Phys. Lett.*, vol. 100, no. 1, p. 013101, 2012.

[117] D. Lin, P. Fan, E. Hasman, and M. L. Brongersma, "Dielectric gradient metasurface optical elements," *Science*, vol. 345, no. 6194, pp. 298–302, 2014.

[118] N. Yu, F. Aieta, P. Genevet, M. A. Kats, Z. Gaburro, and F. Capasso, "A Broadband, Background-Free Quarter-Wave Plate Based on Plasmonic Metasurfaces," *Nano Lett.*, vol. 12, no. 12, pp. 6328–6333, 2012.

[119] F. Aieta, P. Genevet, M. A. Kats, N. Yu, R. Blanchard, Z. Gaburro, and F. Capasso, "Aberration-Free Ultrathin Flat Lenses and Axicons at Telecom Wavelengths Based on Plasmonic Metasurfaces," *Nano Lett.*, vol. 12, no. 9, pp. 4932–4936, 2012.

[120] J. Cheng, D. Ansari-Oghol-Beig, and H. Mosallaei, "Wave manipulation with designer dielectric metasurfaces," *Opt Lett*, vol. 39, no. 21, pp. 6285–6288, 2014.

[121] L. Verslegers, P. B. Catrysse, Z. Yu, J. S. White, E. S. Barnard, M. L. Brongersma, and S. Fan, "Planar lenses based on nanoscale slit arrays in a metallic film," *Nano Lett.*, vol. 9, no. 1, pp. 235–238, 2009.

[122] Y. Yang, W. Wang, P. Moitra, I. I. Kravchenko, D. P. Briggs, and J. Valentine, "Dielectric meta-reflectarray for broadband linear polarization conversion and optical vortex generation," *Nano Lett.*, vol. 14, no. 3, pp. 1394–1399, 2014.

[123] E. Plum and N. I. Zheludev, "Chiral mirrors," *Appl. Phys. Lett.*, vol. 106, no. 22, 2015.

[124] S. Sun, Q. He, S. Xiao, Q. Xu, X. Li, and L. Zhou, "Gradient-index meta-surfaces as a bridge linking propagating waves and surface waves," *Nat. Mater.*, vol. 11, no. 5, pp. 426–431, 2012.

[125] I. P. Radko, V. S. Volkov, J. Beermann, A. B. Evlyukhin, T. Sondergaard, A. Boltasseva, and S. I. Bozhevolnyi, "Plasmonic metasurfaces for waveguiding and field enhancement," *Laser Photonics Rev.*, vol. 3, no. 6, pp. 575–590, 2009.

[126] B. H. Fong, J. S. Colburn, J. J. Ottusch, J. L. Visher, and D. F. Sievenpiper, "Scalar and tensor holographic artificial impedance surfaces," *IEEE Trans. Antennas Propag.*, vol. 58, no. 10, pp. 3212–3221, 2010.

[127] A. Vakil and N. Engheta, "Transformation Optics Using Graphene," *Science*, vol. 332, no. 6035, pp. 1291–1294, 2011.

[128] G. Gok and A. Grbic, "Tailoring the phase and power flow of electromagnetic fields," *Phys. Rev. Lett.*, vol. 111, no. 23, pp. 1–5, 2013.

[129] H.-T. Chen, W. J. Padilla, M. J. Cich, A. K. Azad, R. D. Averitt, and A. J. Taylor, "A metamaterial solid-state terahertz phase modulator," *Nat. Photon.*, vol. 3, no. 3, pp. 148–151, 2009.

[130] C. R. Williams, S. Andrews, S. A. Maier, A. I. Fernández-Domínguez, L. Martín-Moreno, and F. J. García-Vidal, "Highly confined guiding of terahertz surface plasmon polaritons on structured metal surfaces," *Nat. Photon.*, vol. 2, pp. 175–179, 2008.

[131] X. Zhang, Z. Tian, W. Yue, J. Gu, S. Zhang, J. Han, and W. Zhang, "Broadband terahertz wave deflection based on C-shape complex metamaterials with phase discontinuities," *Adv. Mater.*, vol. 25, no. 33, pp. 4567–4572, 2013.

[132] R. Blanchard, G. Aoust, P. Genevet, N. Yu, M. a. Kats, Z. Gaburro, and F. Capasso, "Modeling nanoscale V-shaped antennas for the design of optical phased arrays," *Phys. Rev. B*, vol. 85, no. 15, p. 155457, 2012.

[133] D. M. Pozar, S. D. Targonski, and H. D. Syrigos, "Design of millimeter wave microstrip reflectarrays," *IEEE Trans. Antennas Propag.*, vol. 45, no. 2, pp. 287–296, 1997.

[134] J. A. Encinar, "Design of two-layer printed reflectarrays using patches of variable size," *IEEE Trans. Antennas Propag.*, vol. 49, no. 10, pp. 1403–1410, 2001.

[135] D. M. Pozar and T. A. Metzler, "Analysis of a reflectarray antenna using microstrip patches of variable size," *Electron. Lett.*, vol. 29, pp. 657–658, 1993.

[136] M. Farmahini-Farahani and H. Mosallaei, "Birefringent reflectarray metasurface for beam engineering in infrared," *Opt Lett*, vol. 38, no. 4, pp. 462–464, 2013.

[137] A. Pors and S. I. Bozhevolnyi, "Plasmonic metasurfaces for efficient phase control in reflection," *Opt. Express*, vol. 21, no. 22, pp. 27438–51, 2013.

[138] G. Zheng, H. Mühlenbernd, M. Kenney, G. Li, T. Zentgraf, and S. Zhang, "Metasurface holograms reaching 80% efficiency," *Nat. Nanotechnol.*, vol. 10, no. 4, pp. 308–312, 2015.

[139] D. M. Pozar, *Microwave Engineering*. Wiley, 2004.

[140] B. S. Williams, S. Kumar, H. Callebaut, Q. Hu, and J. L. Reno, "Terahertz quantum-cascade laser at $\lambda \approx 100$ μm using metal waveguide for mode confinement," *Appl. Phys. Lett.*, vol. 83, no. 11, pp. 2124–2126, 2003.

[141] P. W. C. Hon, A. A. Tavallaee, Q.-S. Chen, B. S. Williams, and T. Itoh, "Radiation Model for Terahertz Transmission-Line Metamaterial Quantum-Cascade Lasers," *IEEE Trans. Terahertz Sci. Technol.*, vol. 2, no. 3, pp. 323–332, 2012.

[142] P. W. C. Hon, Z. Liu, T. Itoh, and B. S. Williams, "Leaky and bound modes in terahertz metasurfaces made of transmission-line metamaterials," *J. Appl. Phys.*, vol. 113, no. 3, p. 33105, 2013.

[143] S. Pancharatnam, "Generalized theory of interference, and its applications," *Proc. Indian Acad. Sci.*, vol. A, no. 44, pp. 247–262, 1956.

[144] M. V. Berry, "Quantal Phase Factors Accompanying Adiabatic Changes," *Proc. R. Soc. London A Math. Phys. Eng. Sci.*, vol. 392, no. 1802, pp. 45–57, 1984.

[145] M. J. Escuti, J. Kim, and M. W. Kudenov, "Geometric-Phase Holograms," *Opt. Photonics News*, no. February, pp. 22–29, 2016.

[146] C. Menzel, C. Rockstuhl, and F. Lederer, "Advanced Jones calculus for the classification of periodic metamaterials," *Phys. Rev. A*, vol. 82, no. 5, pp. 1–9, 2010.

[147] M. Kang, T. Feng, H.-T. Wang, and J. Li, "Wave front engineering from an array of thin aperture antennas.," *Opt. Express*, vol. 20, no. 14, pp. 15882–90, 2012.

[148] J. P. Balthasar Mueller, N. A. Rubin, R. C. Devlin, B. Groever, and F. Capasso, "Metasurface polarization optics: Independent phase control of arbitrary orthogonal states of polarization," *Phys. Rev. Lett.*, vol. 118, p. 113901, 2017.

[149] W. Luo, S. Xiao, Q. He, S. Sun, and L. Zhou, "Photonic Spin Hall Effect with Nearly 100% Efficiency," *Adv. Opt. Mater.*, vol. 3, no. 8, pp. 1102–1108, 2015.

[150] C. Pfeiffer and A. Grbic, "Metamaterial Huygens' surfaces: Tailoring wave fronts with reflectionless sheets," *Phys. Rev. Lett.*, vol. 110, no. 19, pp. 1–5, 2013.

[151] N. Engheta, A. Salandrino, and A. Alù, "Circuit elements at optical frequencies: Nanoinductors, nanocapacitors, and nanoresistors," *Phys. Rev. Lett.*, vol. 95, no. 9, pp. 1–4, 2005.

[152] C. Pfeiffer, E. K. Emani, A. M. Shaltout, A. Boltasseva, V. M. Shalaev, and A. Grbic, "Efficient Light Bending with Isotropic Metamaterial Huygens' Surfaces," *Nano Lett.*, vol. 14, no. 5, pp. 2491–2497, 2014.

[153] F. Monticone, N. M. Estakhri, and A. Alù, "Full control of nanoscale optical transmission with a composite metascreen," *Phys. Rev. Lett.*, vol. 110, no. 20, pp. 1–5, 2013.

[154] M. Decker, I. Staude, M. Falkner, J. Dominguez, D. N. Neshev, I. Brener, T. Pertsch, and Y. S. Kivshar, "High-Efficiency Dielectric Huygens' Surfaces," *Adv. Opt. Mater.*, vol. 3, no. 6, pp. 813–820, 2015.

[155] H.-T. Chen, J. F. O'Hara, A. K. Azad, A. J. Taylor, R. D. Averitt, D. B. Shrekenhamer, and W. J. Padilla, "Experimental demonstration of frequency-agile terahertz metamaterials," *Nat. Photon.*, vol. 2, no. 5, pp. 295–298, 2008.

[156] H.-T. Chen, W. J. Padilla, J. M. O. Zide, A. C. Gossard, A. J. Taylor, and R. D. Averitt, "Active terahertz metamaterial devices," *Nature*, vol. 444, no. 7119, pp. 597–600, 2006.

[157] W. L. Chan, H. T. Chen, A. J. Taylor, I. Brener, M. J. Cich, and D. M. Mittleman, "A spatial light modulator for terahertz beams," *Appl. Phys. Lett.*, vol. 94, no. 21, 2009.

[158] M. Liu, H. Y. Hwang, H. Tao, A. C. Strikwerda, K. Fan, G. R. Keiser, A. J. Sternbach, K. G. West, S. Kittiwatanakul, J. Lu, S. a. Wolf, F. G. Omenetto, X. Zhang, K. a. Nelson, and R. D. Averitt, "Terahertz-field-induced insulator-to-metal transition in vanadium dioxide metamaterial.," *Nature*, vol. 487, no. 7407, pp. 345–8, 2012.

[159] J. Lee, M. Tymchenko, C. Argyropoulos, P.-Y. Chen, F. Lu, F. Demmerle, G. Boehm, M.-C. Amann, A. Alù, and M. a. Belkin, "Giant nonlinear response from plasmonic

metasurfaces coupled to intersubband transitions.," *Nature*, vol. 511, no. 7507, pp. 65–9, 2014.

[160] S. Campione, A. Benz, M. B. Sinclair, F. Capolino, and I. Brener, "Second harmonic generation from metamaterials strongly coupled to intersubband transitions in quantum wells," *Appl. Phys. Lett.*, vol. 104, no. 13, 2014.

[161] A. A. Tavallaee, P. W. C. Hon, Q.-S. Chen, T. Itoh, and B. S. Williams, "Active terahertz quantum-cascade composite right/left-handed metamaterial," *Appl. Phys. Lett.*, vol. 102, no. 2, p. 021103, 2013.

[162] S. Xiao, V. P. Drachev, A. V. Kildishev, X. Ni, U. K. Chettiar, H.-K. Yuan, and V. M. Shalaev, "Loss-free and active optical negative-index metamaterials," *Nature*, vol. 466, no. 7307, pp. 735–738, 2010.

[163] E. Plum, V. A. Fedotov, P. Kuo, D. P. Tsai, and N. I. Zheludev, "Towards the lasing spaser: controlling metamaterial optical response with semiconductor quantum dots," *Opt. Express*, vol. 17, no. 10, pp. 8548–8551, 2009.

[164] N. Meinzer, M. Ruther, S. Linden, C. M. Soukoulis, G. Khitrova, J. Hendrickson, J. D. Olitzky, H. M. Gibbs, and M. Wegener, "Arrays of Ag split-ring resonators coupled to InGaAs single-quantum-well gain," *Opt. Express*, vol. 18, no. 23, p. 24140, 2010.

[165] M. S. Seghilani, M. Myara, M. Sellahi, L. Legratiet, I. Sagnes, G. Beaudoin, P. Lalanne, and A. Garnache, "Vortex Laser based on III-V semiconductor metasurface: direct generation of coherent Laguerre-Gauss modes carrying controlled orbital angular momentum," *Sci. Rep.*, vol. 6, p. 38156, 2016.

[166] J. B. Khurgin, "How to deal with the loss in plasmonics and metamaterials," *Nat. Nanotechnol.*, vol. 10, no. 1, pp. 2–6, 2015.

[167] A. A. Tavallaee, B. S. Williams, P. W. C. Hon, T. Itoh, and Q.-S. Chen, "Terahertz quantum-cascade laser with active leaky-wave antenna," *Appl. Phys. Lett.*, vol. 99, p. 141115, 2011.

[168] Y. Todorov, L. Tosetto, J. Teissier, a. M. Andrews, P. Klang, R. Colombelli, I. Sagnes, G. Strasser, and C. Sirtori, "Optical properties of metal-dielectric-metal microcavities in the THz frequency range.," *Opt. Express*, vol. 18, no. 13, pp. 13886–13907, 2010.

[169] N. Laman and D. Grischkowsky, "Terahertz conductivity of thin metal films," *Appl. Phys. Lett.*, vol. 93, no. 5, pp. 1–4, 2008.

[170] W. J. Moore and R. T. Holm, "Infrared dielectric constant of gallium arsenide," *J. Appl. Phys.*, vol. 80, no. 12, p. 6939, 1996.

[171] P. Jouy, Y. Todorov, A. Vasanelli, R. Colombelli, I. Sagnes, and C. Sirtori, "Coupling of a surface plasmon with localized subwavelength microcavity modes," *Appl. Phys. Lett.*, vol. 98, no. 2, 2011.

[172] M. Malerba, T. Ongarello, B. Paulillo, J. M. Manceau, G. Beaudoin, I. Sagnes, F. De Angelis, and R. Colombelli, "Towards strong light-matter coupling at the single-resonator level with sub-wavelength mid-infrared nano-antennas," *Appl. Phys. Lett.*, vol. 109, no. 2, pp. 2–7, 2016.

[173] A. Liu, W. Hofmann, and D. Bimberg, "Two dimensional analysis of finite size high-

contrast gratings for applications in VCSELs," *Opt. Express*, vol. 22, no. 10, pp. 11804–11811, 2014.

[174] L. Xu, C. A. Curwen, P. W. C. Hon, Q.-S. Chen, T. Itoh, and B. S. Williams, "Metasurface external cavity laser," *Appl. Phys. Lett.*, vol. 107, no. 22, p. 221105, 2015.

[175] P. W. C. Hon, *Beam Battern Engineering of Metamaterial Terahertz Quantum-Cascade Devices*. PhD thesis, University of Califorina, Los Angeles, 2013.

[176] J. Faist, "Wallplug efficiency of quantum cascade lasers: Critical parameters and fundamental limits," *Appl. Phys. Lett.*, vol. 90, no. 25, p. 253512, 2007.

[177] T. Gresch, M. Giovannini, N. Hoyer, and J. Faist, "Quantum cascade lasers with large optical waveguides," *IEEE Photonics Technol. Lett.*, vol. 18, no. 3, pp. 544–546, 2006.

[178] L. Xu, P. Hon, T. Itoh, and B. S. Williams, "Terahertz quantum cascade metasurface external cavity laser," in *Intersubband Transitions Quantum Wells 2015*, (Vienna, Austria), 2015.

[179] R. Densing, A. Erstling, M. Gogolbwski, H.-P. Gemund, G. Lundershausen, and A. Gatesman, "Effective far infrared laser operation with mesh couplers," *Infrared Phys.*, vol. 33, no. 3, pp. 219–226, 1992.

[180] S. T. Shanahan and N. R. Heckenberg, "Transmission line model of substrate effects on capacitive mesh couplers," *Appl. Opt.*, vol. 20, no. 23, pp. 4019–4023, 1981.

[181] L. Xu, D. Chen, T. Itoh, J. L. Reno, and B. S. Williams, "Focusing metasurface

quantum-cascade laser with a near diffraction-limited beam," *Opt. Express*, vol. 24, no. 21, pp. 24117–24128, 2016.

[182] A. G. Fox and T. Li, "Resonant Modes in a Maser Interferometer," *Bell Syst. Tech. J.*, vol. 40, no. 453, 1961.

[183] A. G. Fox and T. Li, "Modes in a Maser Interferometer with Curved and Tilted Mirrors," *Proc. IEEE*, vol. 40, pp. 80–89, 1962.

[184] A. E. Siegman, *Lasers*. University Science Books, 1986.

[185] M. Razeghi, "High-performance InP-based mid-IR quantum cascade lasers," *IEEE J. Sel. Top. Quantum Electron.*, vol. 15, no. 3, pp. 941–951, 2009.

[186] J. Huang and J. A. Encinar, *Reflectarray Antennas*. Wiley-IEEE Press, 2007.

[187] Y. Rahmat-Samii, "Reflector antennas," in *Antenna Eng. Handb.* (J. L. Volakis, ed.), McGraw-Hill Companies, 2007.

[188] D. Berry, R. Malech, and W. Kennedy, "The reflectarray antenna," *IEEE Trans. Antennas Propag.*, vol. 11, no. 6, pp. 645–651, 1963.

[189] T. Niu, W. Withayachumnankul, B. S. Y. Ung, H. Menekse, M. Bhaskaran, S. Sriram, and C. Fumeaux, "Experimental demonstration of reflectarray antennas at terahertz frequencies," *Opt. Express*, vol. 21, no. 3, pp. 2875–2889, 2013.

[190] J. Ginn, B. Lail, J. Alda, and G. Boreman, "Planar infrared binary phase reflectarray," *Opt. Lett.*, vol. 33, no. 8, pp. 779–781, 2008.

[191] J. C. Ginn, B. A. Lail, and G. D. Boreman, "Phase Characterization of Reflectarray Elements at Infrared," *IEEE Trans. Antennas Propag.*, vol. 55, no. 11, pp. 2989–2993, 2007.

[192] P. Genevet and F. Capasso, "Holographic optical metasurfaces: a review of current progress," *Reports Prog. Phys.*, vol. 78, no. 2, p. 24401, 2015.

[193] A. E. Siegman, M. W. Sasnett, and T. F. Johnston, "Choice of clip levels for beam width measurements using knife-edge techniques," *IEEE J. Quantum Electron.*, vol. 27, no. 4, pp. 1098–1104, 1991.

[194] H. Richter, N. Rothbart, and H.-W. Hübers, "Characterizing the beam properties of terahertz quantum-cascade lasers," *J. Infrared Millim. THz Waves*, vol. 35, no. 8, pp. 686–698, 2014.

[195] "International Organization for Standardization, document no. ISO 11146, Lasers and laser-related equipment - Test methods for laser beam parameters - Beam width, divergence, angle and beam propagation factor," 1999.

[196] J. S. Blakemore, "Semiconducting and other major properties of gallium arsenide," *J. Appl. Phys.*, vol. 53, no. 10, 1982.

[197] B. S. Williams, S. Kumar, Q. Hu, and J. L. Reno, "Distributed-feedback terahertz quantum-cascade lasers with laterally corrugated metal waveguides," *Opt. Lett.*, vol. 30, no. 21, p. 2909, 2005.

[198] L. Xu, D. Chen, C. A. Curwen, M. Memarian, J. L. Reno, T. Itoh, and B. S. Williams,

"Metasurface quantum-cascade laser with electrically switchable polarization," *Optica*, vol. 4, no. 4, p. 468, 2017.

[199] R. J. Zhou, B. Ibarra-Escamilla, J. W. Haus, P. E. Powers, and Q. W. Zhan, "Fiber laser generating switchable radially and azimuthally polarized beams with 140 mW output power at 1.6 m wavelength," *Appl. Phys. Lett.*, vol. 95, no. 19, p. 191111, 2009.

[200] O. B. Yu, J. L. Cruz, and M. V. Andres, "Polarization switchable Erbium-doped all-fiber laser," *Laser Phys. Lett.*, vol. 5, no. 9, p. 676, 2008.

[201] A. Fraser, M. Bernier, J.-D. Deschênes, É. Weynant, J. Genest, and R. Vallée, "Polarization-switchable Q-switched DFB fiber laser," *Opt. Lett.*, vol. 35, no. 7, pp. 1046–1048, 2010.

[202] K. D. Choquette, D. A. Richie, and R. E. Leibenguth, "Temperature-Dependence of Gain-Guided Vertical-Cavity Surface-Emitting Laser Polarization," *Appl. Phys. Lett.*, vol. 64, no. 16, pp. 2062–2064, 1994.

[203] K. D. Choquette, K. L. Lear, R. P. Schneider, and R. E. Leibenguth, "Gain-Dependent Polarization Properties of Vertical-Cavity Lasers," *14th IEEE Int. Semicond. Laser Conf.*, pp. 149–150, 1994.

[204] T. H. Russell and T. D. Milster, "Polarization switching control in vertical-cavity surface-emitting lasers," *Appl. Phys. Lett.*, vol. 70, no. 19, pp. 2520–2522, 1997.

[205] K. D. Choquette, K. L. Lear, R. E. Leibenguth, and M. T. Asom, "Polarization Modulation of Cruciform Vertical-Cavity Laser-Diodes," *Appl. Phys. Lett.*, vol. 64, no. 21, pp. 2767–2769, 1994.

[206] M. Torre, A. Hurtado, A. Quirce, A. Valle, L. Pesquera, and M. Adams, "Polarization Switching in Long-Wavelength VCSELs Subject to Orthogonal Optical Injection," *IEEE J. Quantum Electron.*, vol. 47, no. 1, pp. 92–99, 2011.

[207] V. A. Fedotov, A. S. Schwanecke, N. I. Zheludev, V. V. Khardikov, and S. L. Prosvirnin, "Asymmetric transmission of light and enantiomerically sensitive plasmon resonance in planar chiral nanostructures," *Nano Lett.*, vol. 7, no. 7, pp. 1996–1999, 2007.

[208] T. Kan, A. Isozaki, N. Kanda, N. Nemoto, K. Konishi, H. Takahashi, M. Kuwata-Gonokami, K. Matsumoto, and I. Shimoyama, "Enantiomeric switching of chiral metamaterial for terahertz polarization modulation employing vertically deformable MEMS spirals," *Nat. Commun.*, vol. 6, 2015.

[209] N. F. Yu, Q. J. Wang, C. Pflugl, L. Diehl, F. Capasso, T. Edamura, S. Furuta, M. Yamanishi, and H. Kan, "Semiconductor lasers with integrated plasmonic polarizers," *Appl. Phys. Lett.*, vol. 94, no. 15, p. 151101, 2009.

[210] D. Dhirhe, T. J. Slight, B. M. Holmes, D. C. Hutchings, and C. N. Ironside, "Quantum cascade lasers with an integrated polarization mode converter," *Opt. Express*, vol. 20, no. 23, pp. 25711–25717, 2012.

[211] P. Rauter, J. Lin, P. Genevet, S. P. Khanna, M. Lachab, A. G. Davies, E. H. Linfield, and F. Capasso, "Electrically pumped semiconductor laser with monolithic control of circular polarization," *Proc. Natl. Acad. Sci. USA*, 2014.

[212] D. Dhirhe, T. J. Slight, B. M. Holmes, and C. N. Ironside, "Active polarisation control

of a quantum cascade laser using tuneable birefringence in waveguides," *Opt. Express*, vol. 21, no. 20, pp. 24267–24280, 2013.

[213] G. Liang, Y. Zeng, X. Hu, H. Yu, H. Liang, Y. Zhang, L. Li, A. G. Davies, E. H. Linfield, and Q. J. Wang, "Monolithic Semiconductor Lasers with Dynamically Tunable Linear-to-Circular Polarization," *ACS Photonics*, vol. 4, no. 3, pp. 517–524, 2017.

[214] G. S. Jenkins, D. C. Schmadel, and H. D. Drew, "Simultaneous measurement of circular dichroism and Faraday rotation at terahertz frequencies utilizing electric eld sensitive detection via polarization modulation," *Rev. Sci. Instrum.*, vol. 81, p. 83902, 2010.

[215] G. D. Metcalfe, M. Wraback, A. Strikwerda, K. Fan, and X. Zhang, "Terahertz Polarimetry Based on Metamaterial Devices," *Proc. SPIE*, vol. 8363, p. 83630O, 2012.

[216] C. F. Hsieh, R. P. Pan, T. T. Tang, H. L. Chen, and C. L. Pan, "Voltage-controlled liquid-crystal terahertz phase shifter and quarter-wave plate," *Opt. Lett.*, vol. 31, no. 8, pp. 1112–1114, 2006.

[217] Y. D. Dong and T. Itoh, "Substrate Integrated Composite Right-/Left-Handed Leaky-Wave Structure for Polarization-Flexible Antenna Application," *IEEE Trans. Antennas Propag.*, vol. 60, no. 2, pp. 760–771, 2012.

[218] R. Oron, S. Blit, N. Davidson, A. a. Friesem, Z. Bomzon, and E. Hasman, "The formation of laser beams with pure azimuthal or radial polarization," *Appl. Phys. Lett.*, vol. 77, no. 21, p. 3322, 2000.

[219] K. Youngworth and T. Brown, "Focusing of high numerical aperture cylindrical-vector beams," *Opt. Express*, vol. 7, no. 2, p. 77, 2000.

[220] R. Dorn, S. Quabis, and G. Leuchs, "Sharper Focus for a Radially Polarized Light Beam," *Phys. Rev. Lett.*, vol. 91, no. 23, p. 233901, 2003.

[221] X. Wang, C. Shen, T. Jiang, Z. Zhan, Q. Deng, W. Li, W. Wu, N. Yang, W. Chu, and S. Duan, "High-power terahertz quantum cascade lasers with 0.23 W in continuous wave mode," *AIP Adv.*, vol. 6, no. 075210, 2016.

[222] C. Worrall, J. Alton, M. Houghton, S. Barbieri, H. E. Beere, D. Ritchie, and C. Sirtori, "Continuous wave operation of a superlattic quantum cascade laser emitting at 2 THz," *Opt. Express*, vol. 14, no. 1, pp. 171–181, 2006.